Charged Hadron Multiplicities in 490 GeV Deep Inelastic Muon Scattering

by

Stephen Charles O'Day

Dissertation submitted to the Faculty of the Graduate School
of the University of Maryland in partial fulfillment
of the requirements for the degree of
Doctor of Philosophy
1990

Advisory Committee:

Professor Andris Skuja, Chairman/Advisor
Professor Nicholas Chant
Professor George Snow
Professor Gus Zorn
Professor Kenneth Berg

pHHb:883

Abstract

Title of Dissertation: Charged Hadron Multiplicities in 490 GeV Deep Inelastic Muon Scattering

Stephen Charles O'Day, Doctor of Philosophy,1990

Dissertation directed by: Professor Andris Skuja,Physics Department

In this thesis, the multiplicity of charged hadrons produced in deep inelastic muon-nucleon scattering was studied using a 490 Gev muon beam impinging upon liquid hydrogen and liquid deuterium targets. Multiplicity was measured using a streamer chamber and forward wire tracking chambers. Muon kinematics were obtained by beam tracking upstream of the target and identification of the scattered muon in the forward detectors. The multiplicity distributions and average multiplicity for H_2 and D_2 were found to be consistent with each other both qualitatively and quantitatively. This result supports the statement that sea quark scattering dominates as one would expect from the fact that more than 90 % of the data is in the $x_{Bj} < .2$ region. Agreement between the data and the Lund Monte Carlo generated with Morfin and Tung structure functions was observed. This result supports the assumption in that model that up to 50 % of the DIS data is photon-gluon fusion.

Dedication

This thesis is dedicated to my mother, Jean R. O'Day and to the memory of my father, Frank C. O'Day,Sr.

FERMILAB
LIBRARY

Acknowledgements

I thank the members of the E665 Collaboration who worked tirelessly in constructing detectors and writing software to collect and analyze the data. Among E665, I would like to thank all my colleagues at the New Muon Lab whose review of my analysis helped to improve it. I extend special thanks to my collaborators at FNAL, MPI and Crakow and their film measurement people.

I would like to acknowledge a few individuals who helped me more personally as well. My advisor, Andris Skuja, gave me good advice and shared his great wealth of knowledge with me. Shuichi Kunori helped me to develop a critical eye for detail. George Snow inspired me to pursue physics seriously while I was a freshman in college and later hired me for E665. Silhacene Aid was never too busy to lend me a hand with a variety of frustrating tasks.

Finally, I must thank my wife, Patricia, for her love and patience through this long endeavor.

Table of Contents

List of Tables vii

List of Figures viii

1. Introduction 1

2. Theoretical Background 3

2.1 DIS Cross Section and Structure 5

2.1.1 Kinematical Variables 5

2.1.2 Cross Section 5

2.1.3 Quark Parton Model 6

2.1.4 Scaling Violation and QCD Corrections 7

2.2 Hadronization 10

2.2.1 Color Flux Tube Model 10

2.2.2 Lund Implementation 11

2.2.3 Parton Shower Model 12

2.2.4 Kiselev and Petrov Model 14

2.2.5 KNO Scaling 15

2.2.6 Kinematical Range of Experiments 15

2.2.7 Review of Existing Data 15

3. The Experiment and the Beam 26

4. The Apparatus 29

4.1 Beam Spectrometer 30

4.2 Vertex Spectrometer 31

4.2.1 Vertex Spectrometer Particle ID 32

4.2.2 Vertex Spectrometer Wire Chambers 33

4.2.3 The Streamer Chamber 34

4.3 The Forward Spectrometer 35

4.3.1 Forward Spectrometer Wire Chambers 35
4.3.2 Forward Spectrometer Particle Identification 38
4.4 Muon Triggering and ID Apparatus 41
5. Triggers 43
5.1 PLRF Tevatron Radio Frequency Beam Signals 44
5.2 The Halo Veto System 44
5.3 The LATB Beam Trigger and RLAT Normalization Trigger 45
5.4 The Large Angle Trigger(LAT) 46
5.5 The SATB Beam Trigger and RSAT Normalization Trigger 46
5.6 The Small Angle Trigger(SAT) 47
5.7 The FCAL Electromagnetic Energy Trigger 48
5.8 The HALO Trigger 48
5.9 The PCN Coincident Streamer Chamber Triggers 48
6. Data and Data Acquisition 51
6.1 Streamer Chamber Data 52
6.2 Electronic Data Acquisition 53
7. Event Reconstruction 56
7.1 Forward Spectrometer Event Reconstruction 58
7.2 Streamer Chamber Track Reconstruction 61
7.3 Combined SC-Forward Spectrometer Event Reconstruction 64
7.4 SC-Forward Spectrometer Alignment Constants 65
8. Analysis 68
8.1 Event Selection 70
8.2 Electromagnetic Event Cuts 73
8.3 LAT·PCNZ Trigger Acceptance 75
8.4 Uncorrected Multiplicity 78

8.5 Monte Carlo Corrections 78
8.6 Monte Carlo vs. Data Comparisons 85
8.6.1 Vertex Fit Residuals 87
8.6.2 Track Momentum and Angle Distributions 89
8.6.3 SC-FS Track Match Residuals 89
8.7 Monte Carlo Multiplicity Contamination Studies 92
8.8 Multiplicity Acceptance 98
9. Results 115
9.1 Multiplicity Distributions 115
9.2 Mean Multiplicity vs. Ln(W^2) and Ln(Q^2) 115
9.3 Systematics 126
10. Conclusions 139
References 140

List of Tables

Table 1. Beam information 31

Table 2. Processed E665 electronic events 51

Table 3. Events with streamer chamber pictures 52

Table 4. Streamer chamber institutional distribution 53

Table 5. Streamer chamber pictures passing kinematic cuts 54

Table 6. Streamer chamber track measurement characteristics 57

Table 7. Multiplicity correction factors(standard close cut) 86

Table 8. Multiplicity correction factors vs. W^2 87

Table 9. Multiplicity correction factors vs x_v,W,Q^2 100

Table 10. Multiplicity x_{vertex} systematics. 135

Table 11. Systematics associated with multiplicity method used 136

List of Figures

Figure 1. Feynman QED diagram....4

Figure 2. Feynman QCD diagrams....8

Figure 3. Quark and Gluon distribution functions....9

Figure 4. The hadronization process in DIS....10

Figure 5. Morfin and Tung QCD weights....13

Figure 6. $< N >_{Charged}$ as a function of $Ln(W^2)$....16

Figure 7. UA5 differential multiplicity....17

Figure 8. BEBC multiplicity....18

Figure 9. BEBC dispersion....19

Figure 10. FNAL bubble chamber ν-p,n multiplicity....20

Figure 11. FNAL bubble chamber ν-p,n multiplicity(by charge)....21

Figure 12. pp, p-nucleus multiplicity....22

Figure 13. NA9 KNO scaling....23

Figure 14. NA9 multiplicity....24

Figure 15. NA9 multiplicity vs. x_{Bj}....25

Figure 16. The NM beamline....27

Figure 17. Particle ID momentum range....33

Figure 18. Example of a hydrogen streamer chamber picture....36

Figure 19. The E665 electromagnetic calorimeter....39

Figure 20. Large,small angle trigger acceptance....47

Figure 21. LAT · PCN trigger acceptance....50

Figure 22. E665 data acquisition system....55

Figure 23. Streamer chamber local coordinate system....64

Figure 24. Q^2 distributions....71

Figure 25. W^2 distributions....72

Figure 26. y_{Bj} distributions.....74
Figure 27. Ratio of LAT·PCNZ over LAT vs. W.....76
Figure 28. Fraction of LAT·PCNZ triggered by found tracks vs. W.....77
Figure 29. Monte Carlo geometry simulation.....80
Figure 30. Monte Carlo vs. data PCN plane hit multiplicity.....81
Figure 31. SC/FS ratio of track multiplicity in the beam region.....82
Figure 32. y' vs momentum.....84
Figure 33. Vertex residuals.....88
Figure 34. Track minimum distance to vertex.....90
Figure 35. Track minimum distance/error to vertex.....91
Figure 36. Track $1/p$.....92
Figure 37. Lab frame track p_T.....93
Figure 38. Track ϕ.....94
Figure 39. SC-FS track match residuals.....95
Figure 40. SC-FS track momentum comparisons.....96
Figure 41. Secondary interaction vertex multiplicity.....97
Figure 42. Forward spectrometer geometrical acceptance.....101
Figure 43. Geometrical acceptance of "box" cut.....102
Figure 44. Acceptance loss of "box" cut.....103
Figure 45. χ^2 of reconstructed track vs. input track match.....104
Figure 46. Fraction of ghost tracks vs. x_F.....105
Figure 47. Geometrical acceptance vs. reconstruction.....106
Figure 48. Uncorrected multiplicity.....107
Figure 49. Ratio of competing multiplicity methods.....108
Figure 50. Monte Carlo corrected average multiplicity vs. X_{vertex}.....110
Figure 51. Monte Carlo correction factors vs. X_{vertex}.....111

Figure 52. Multiplicity excluding the beam region.....113
Figure 53. Multiplicity excluding the beam region SC tracks.....114
Figure 54. D_2 data $P(N) < N >$ vs $N/ < N >$.....116
Figure 55. Charged hadron multiplicity vs. LnW^2.....117
Figure 56. Correction factors vs. LnW^2.....118
Figure 57. Low W H_2 charged hadron multiplicity vs. LnQ^2.....119
Figure 58. High W H_2 charged hadron multiplicity vs. LnQ^2.....121
Figure 59. H_2 Lund shower and Lund Ariadne multiplicity predictions.....122
Figure 60. High W H_2 multiplicity vs. LnQ^2 MC comparisons.....123
Figure 61. Contributions of q, qg and qq to DIS.....124
Figure 62. $< n >$ contributions of q, qg and qq to DIS.....125
Figure 63. Low W D_2 charged hadron multiplicity vs. LnQ^2.....126
Figure 64. High W D_2 charged hadron multiplicity vs. LnQ^2.....127
Figure 65. D_2 Lund shower and Lund Ariadne multiplicity predictions.....128
Figure 66. High W D_2 multiplicity vs. LnQ^2 MC comparisons.....129
Figure 67. D_2 $< n >$ of q, qg and qq.....130
Figure 68. Forward and backward D_2 multiplicity.....131
Figure 69. Forward and backward $< N >$ correction factors.....132
Figure 70. Monte Carlo x_F.....133
Figure 71. D_2 x_F.....134
Figure 72. $< n >$ using different methods.....137
Figure 73. Correction factors for different methods.....138

Chapter 1 Introduction

A number of nuclei(H_2,D_2 and Xe) were studied by a muon scattering experiment using a beam of 490 GeV muons(Fermilab E665). The purpose of this experiment is threefold. First, the hadronic final state may be studied in terms of particle identity, kinematics and multiplicity. Second, measurements of the nucleon structure functions as functions of the muon-nucleon four-momentum transfer (Q^2) and energy transfer (ν) can be made. Third, nuclear structure functions may be studied at low Q^2.

The focus of this work is the study of charged hadron multiplicity in muon-hydrogen and muon-deuterium scattering. Although this topic has already been examined, previous fixed target muon experiments were a factor of 2 or more lower in beam energy. With the increase in beam energy, quantum chromodynamics(QCD) contributions to the final hadronic state become increasingly important. Data from e^+e^- interactions at comparable hadronic energy to E665 indicates that E665 will have a sample of data containing more gluon induced final state hadron events relative to the number of single quark events than lower energy fixed target muon experiments. Both quark-gluon bremsstrahlung and photon-gluon fusion contribute to the hadronic final state in muon scattering, while only the former process is observed in e^+e^- interactions.

Previous experiments have contributed greatly to our understanding of deep inelastic scattering. FNAL Experiment 26(1974) was Fermilab's first deep inelastic muon experiment at high energy. It established scaling violations of the structure functions at large Q^2. E98[1,2,3] and 398[4] studied deep inelastic muon scattering as well as final state hadrons with a beam energy of 200 to 300 GeV during the 1970's. It was the first muon experiment to analyze muon scattering in the language of QCD. In a similar(but later) experiment at CERN,

the EMC collaboration studied hadronization and nucleon structure functions with various targets using a 280 GeV muon beam- but with higher statistics[5,6] than the earlier Fermilab experiments. The CERN NA9 collaboration added a streamer chamber to the EMC apparatus to enhance its geometrical acceptance permitting measurements of charged hadron multiplicity in muon-hydrogen scattering. The Petra storage ring e^+e^- experiments PLUTO,TASSO and JADE[7,8] at DESY and the e^+e^- Mark II,HRS and TPC[9] experiments at SLAC studied charged hadron multiplicity at center of mass energies in the range from 4 to 29 GeV.

Chapter 2 Theoretical Background

The most fundamental constituents of matter are grouped by physicists according to the SU(6) flavor group Standard Model. Within this model, electrons, muons and tau particles along with their respective neutrinos are spin $\frac{1}{2}$ fermions and are organized into families (e, ν_e),(μ, ν_μ), and (τ, ν_τ). Each lepton has thus far been shown experimentally to interact identically (short of mass differences) as the others, to exhibit lepton number conservation, and to be without substructure. Within the Standard Model, the other fundamental constituent of matter is the quark(also a spin $\frac{1}{2}$ fermion). Three mass generations of quarks are predicted to exist. These are the light quarks (u,d), the intermediate mass quarks (c,s) and the heavy quarks (b,t). Only the top quark remains to be observed experimentally.

Hadrons are made of quarks. Mesons are made of $q\bar{q}$ pairs. Baryons consist primarily of 3 quarks or anti-quarks. The proton is a uud combination. The neutron is udd. They are bound together by gluon exchange described by QCD.

The fundamental particles of the Standard Model interact in four different ways each characterized by the exchange of a mediating boson. The electromagnetic interaction is mediated by the virtual photon, the strong interaction by the gluon, the weak by the W and Z and the gravitational by the graviton. The intermediate boson couples to the quark and lepton via charge, color charge(red,yellow,blue),electro-weak charge and mass respectively. The constituent particles underlying muon scattering may be understood within this framework.

Within the limitations of E665, the muon probes the nuclei held together by strong interactions via a process we think we understand, quantum electrodynamics (QED)[10,11] and the radiation of a virtual photon (see figure 1). The

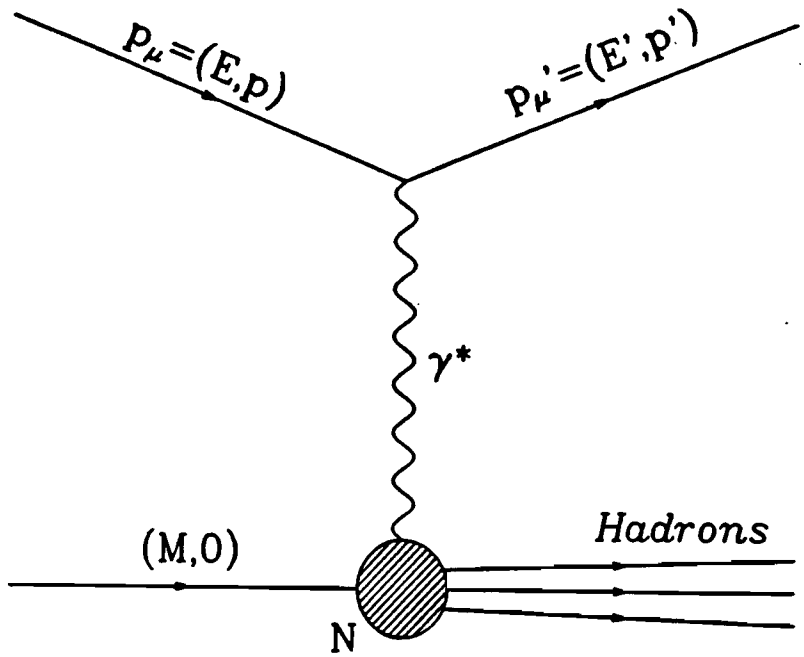

Figure 1. Feynman QED diagram for virtual photon exchange.

electromagnetic and weak interactions have been most successfully described within a single framework[12]. Attempts to create a "grand unified" field theory in which all interactions would be described within a single framework have met with limited success and are described elsewhere[13].

E665 probes the nucleus using the virtual photon whose four-momentum squared is Q^2. This scattering is characterized by the quantum mechanical wavelength of the photon which by $\lambda = h/(p \approx \sqrt{Q^2})$ is inversely proportional to the virtual photon momentum. Thus, Q^2 determines how deeply the nucleus is probed.

§2.1 DIS Cross Section and Structure

§2.1.1 Kinematical Variables

The fundamental process in muon-nucleon scattering is virtual photon exchange. This process is described by the Feynman diagram in figure 1.

This interaction is characterized by the momentum transfer q to the nucleus. Using naive quantum mechanics, the larger $\vec{q}$, the smaller the distance probed within the nucleus. The kinematics of this process can best be described by defining certain key variables in terms of the four-vector momenta k, k' of the incoming and outgoing muons and the target mass M

$$Q^2 = -q^2 = (\vec{k} - \vec{k}')^2 \approx 4E_u E'_u \sin\frac{\theta_u}{2}^2 \quad where\ |\vec{k}^2| >> m^2{}_u$$

$$\nu = \frac{\vec{p}\cdot\vec{q}}{M} = E_u - E'_u = E_{\gamma^*} = \text{energy transfer in the lab}$$

$$W^2 = 2M\nu + M^2 - Q^2 = \text{available hadronic energy in C.M. squared}$$

$$x_{Bj} = \frac{Q^2}{2M\nu} \text{ for } 0 \leq x \leq 1$$

$$y_{Bj} = \frac{\nu}{E_\mu} \text{ for } 0 \leq y \leq 1$$

The importance of x_{Bj} and y_{Bj} to deep inelastic scattering(DIS) was first recognized by Bjorken. The fraction of the nucleon momentum carried by the struck quark is x_{Bj} while y_{Bj} is the fraction of the energy transferred to the parton. Note that $x_{Bj} = 1$ defines an elastic process while $x_{Bj} < 1$ is inelastic.

§2.1.2 Cross Section

The single photon exchange differential cross section is[14]:

$$\frac{d\sigma}{dE'd\Omega} = \frac{\alpha^2}{4E^2 sin^4\frac{\theta}{2}}[W_2(\nu, Q^2)cos^2\frac{\theta}{2} + 2W_1(\nu, Q^2)sin^2\frac{\theta}{2}]$$

where

$$E = \ the\ incident\ muon\ energy$$

and

$$\theta = \textit{the scattered muon angle}$$

W_1 and W_2 are the structure functions of the nucleon and are constant for point-like scattering.

§2.1.3 Quark Parton Model

In the quark parton model, nucleons are comprised of point-like particles with spin $\frac{1}{2}$ called partons. In the large Q^2 limit, one may use the structure functions W_1 and W_2 to define new structure functions which depend only on Bjorken x:

$$MW_1(\nu, Q^2) \longrightarrow F_1(x)$$

$$\nu W_2(\nu, Q^2) \longrightarrow F_2(x)$$

The short wavelength of the virtual photon at high Q^2 results in it interacting with only a single parton(quark) yielding Bjorken scaling in the F_1 and F_2 structure functions. Re-writing the cross section as a differential with respect to Q^2 and ν gives:

$$\frac{d\sigma}{dQ^2 d\nu} = \frac{4\pi\alpha^2 E'}{Q^4 E\nu}[2\frac{\nu}{M}F_1(Q^2,\nu)sin^2\frac{\theta}{2} + F_2(Q^2,\nu)cos^2\frac{\theta}{2}]$$

The dependence of the structure functions on both Q^2 and ν is called scaling violation and will be discussed later. Nonetheless, at large Q^2 the parton model permits the writing of F_1 in terms of F_2.

$$F_1(x) = \frac{F_2(x)}{2x}$$

This equation is known as the Callen-Gross relation[15]. Using this equation, one can express the cross-section in terms of F_2 alone. Within the parton model, scaling is understood to be the virtual photon scattering from individual point-like partons. The scattering becomes point-like as the wavelength of the virtual photon probing the nucleon shortens with increasing Q^2.

F_2 is now defined to be the sum of the probability distributions of the individual quark momenta in the nucleon.

$$\frac{1}{x}F_2 \equiv \sum_i e_i{}^2 f_i(x)$$

Specifically for the proton(ignoring heavy quark terms), this is:

$$\frac{1}{x}F_2^p(x,Q^2) = (\frac{2}{3})^2[u^p + \bar{u}^p] + (\frac{1}{3})^2[d^p + \bar{d}^p] + (\frac{1}{3})^2[s^p + \bar{s}^p]$$

where u,d and s are the u,d and s quark distribution functions. Since the proton and neutron are members of an isospin doublet, the structure function for the neutron is:

$$\frac{1}{x}F_2^n(x,Q^2) = (\frac{2}{3})^2[u^n + \bar{u}^n] + (\frac{1}{3})^2[d^n + \bar{d}^n] + (\frac{1}{3})^2[s^n + \bar{s}^n]$$

§2.1.4 Scaling Violation and QCD Corrections

The description of the quark parton model given is only part of the general QCD framework which includes exchanged gluons as well as quarks or partons. The leading Feynman diagrams for muon-nucleon interactions are shown in figure 2.

When the virtual photon interacts with a gluon emitted by a quark, the $q\bar{q}$ pair is created. This process is called photon-gluon fusion. When a struck valence quark emits a gluon, the process is called gluon bremsstrahlung. These diagrams violate scaling by their explicit dependence on Q^2 as demonstrated by the density function evolution equations[16,17]:

$$\frac{df_i(x,Q^2)}{dln(Q^2)} = \frac{\alpha_S(Q^2)}{2\pi}\int_x^1 \frac{dy}{y}[P_{qq}(\frac{x}{y})f_i(y,Q^2) + P_{qg}(\frac{x}{y})g(y,Q^2)]$$

$$\frac{dg(x,Q^2)}{dln(Q^2)} = \frac{\alpha_S(Q^2)}{2\pi}\int_x^1 \frac{dy}{y}[\Sigma_j P_{gq}(\frac{x}{y})f_j(y,Q^2) + P_{gg}(\frac{x}{y})g(y,Q^2)]$$

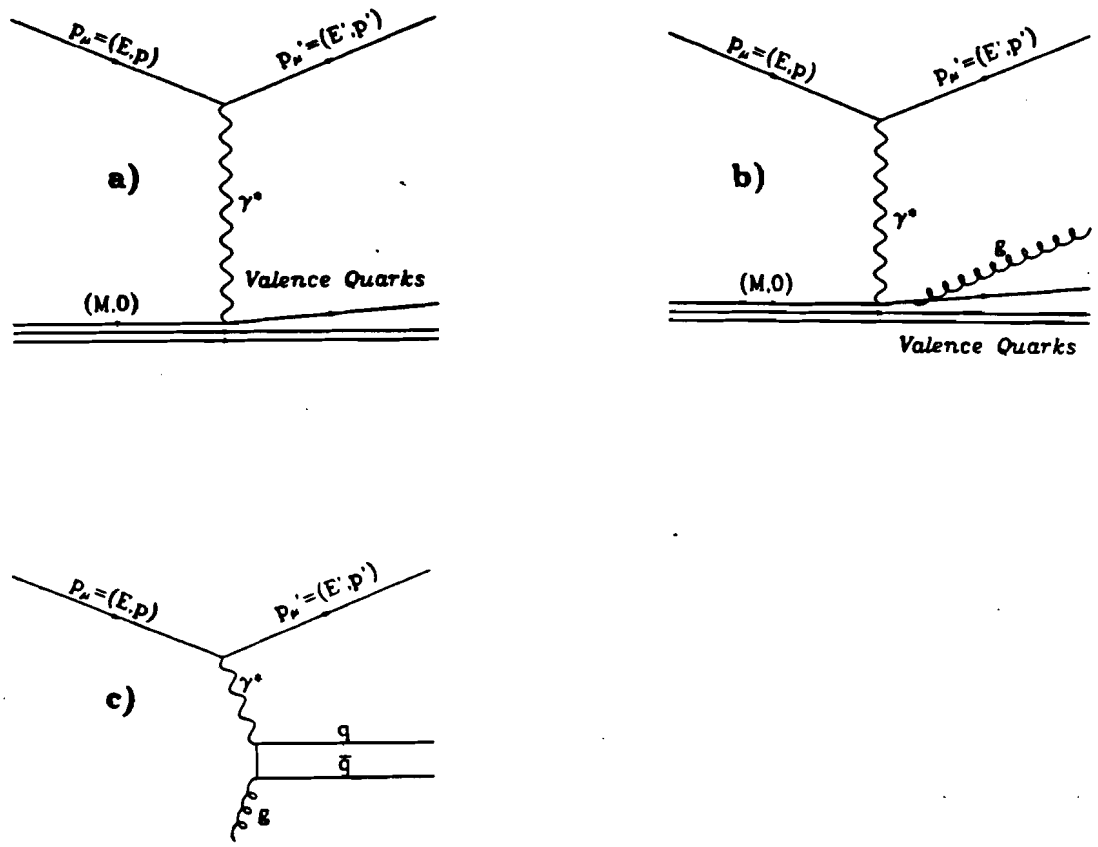

Figure 2. a)Feynman diagram for naive parton model DIS. b) Feynman diagram for gluon bremsstrahlung. c) Feynman diagram for photon-gluon fusion.

In the density evolution equation, j is the sum over all $q\bar{q}$ flavors and P is the splitting function. P gives the probability of finding a quark(gluon) with momentum fraction x inside a quark(gluon) with momentum fraction y.

Existing data has been parameterized for example by Morfin and Tung[18] and Gluck, Hoffmann and Reya(GHR)[19] in an attempt to extract the individual

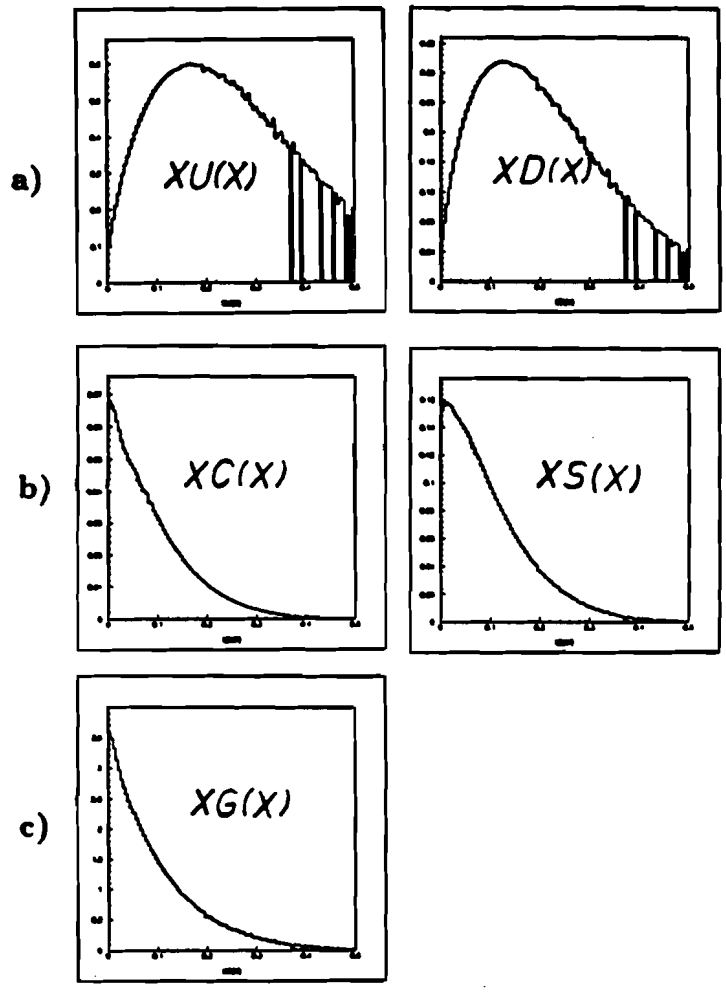

Figure 3. a) Valence quark distribution functions, b) Sea quark distribution functions, c) Gluon distribution function.

quark and gluon distribution functions. The quark and gluon distribution functions of Morfin and Tung are shown in figure 3 and will be used to generate the QCD weights used in this study. These distributions are the best knowledge we have regarding the distribution of quarks and gluons in the nucleon.

§2.2 Hadronization

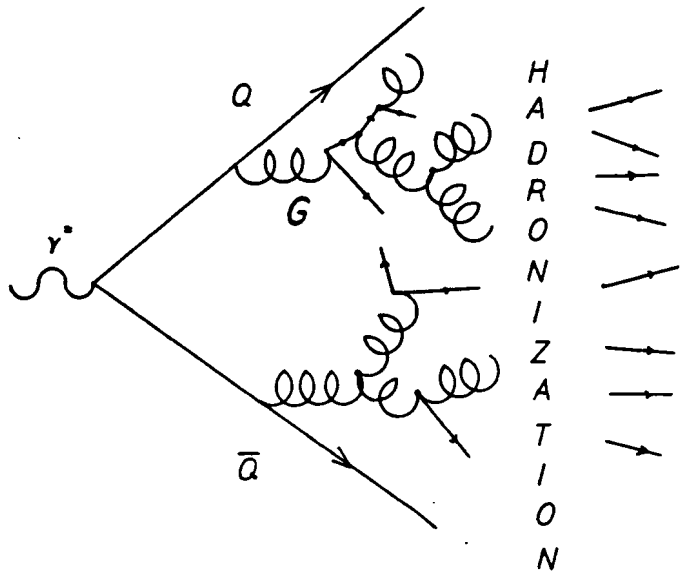

Figure 4. The hadronization process in DIS.

Thus far the variety of virtual photon interactions has been discussed, but not the resulting "hadron showers" which follow. In the naive parton model, a muon imparts energy W to the nucleon via the virtual photon and this energy is available for the creation of new particles. The hadronization process begins as the struck quark within the nucleon pulls away from the remaining di-quark. Potential energy is built up in the system until its release in the form of quark anti-quark pairs which re-combine to form hadrons. This is illustrated in figure 4.

§2.2.1 Color Flux Tube Model

The hadronization process has not yet been calculated with QCD. Only model calculations exist. In the naive parton model, a complicated QCD process is represented by a flux tube[20,21,22,23] which exists between the quark and

di-quark which stretches as the two move apart. The energy stored in the tube and the probability of the tube breaking both increase as the length of the tube increases. This dependence is believed to be linear in energy and the Lund model[24,25,26,27] assigns a phenomenological value of 1 GeV/fm to the "string" constant. When the flux tube or string breaks, $q\bar{q}$ pairs are created and combine amongst themselves to form primary hadrons. Heavy quark production from the described soft fragmentation process is less likely according to this model since the tube must become longer before breaking in order to store sufficient energy to create these quarks. The production probability is modeled as a tunneling phenomenon whose production probability in terms of mass and transverse momentum can be expressed as:

$$P(m, p_T) = e^{-\frac{\pi}{\kappa}m_t^2} = e^{-\frac{\pi}{\kappa}m^2}e^{-\frac{\pi}{\kappa}p_t^2}$$

This momentum dependence leads to the relative quark production ratios:

$$u : d : s : c \sim 1 : 1 : 0.3 : 10^{-11}$$

It should be noted finally that to produce a physical quark with non-zero transverse mass, that the string must break early. With the scheme thus far, the system doesn't build up energy quickly enough for the creation of fast hadrons. Thus, an additional vertex weighting factor is introduced of the form:

$$|g^2| = (\kappa\tau)^2[(\kappa\tau)^2 + m_t^2]^{-1}$$

where τ is the proper time for the vertex(of the outgoing $q\bar{q}$ pair) and κ is the "string" constant.

§2.2.2 Lund Implementation

The Lund model(developed at that university) is a phenomenological Monte Carlo implementation of the flux tube model whose parameters come from fits

to existing data. It is a convenient software package and will be used to generate events for this analysis from which acceptance corrections will be made as well as physics predictions against which the data can be compared. The processes included in this generator are parton model DIS, gluon bremsstrahlung and photon gluon fusion. The string model is used to create the $q\bar{q}$ pairs for all diagrams. The QCD part of the model is controlled by a database of QCD weights. These weights represent the quark and gluon x_{Bj} distributions as obtained from fits to existing data. The weights as a function of Q^2 for different W bins are shown in figure 5.

The Morfin and Tung weights tend to generate higher multiplicities than Gluck,Hoffman and Reya or Lund shower models(see section 2.2.3) particularly at small x. Using Morfin and Tung, the Lund model generates events based on a prediction that 70-90 % of the deep inelastic scatters in the kinematic region of E665 will be simple parton model single jet events. A few percent will be gluon bremsstrahlung and 15 to 25 % will be photon-gluon fusion.

§2.2.3 Parton Shower Model

The Lund program with Jetset version 6.2[28] has two parton shower model implementations available to replace the flux tube model. These generators attempt to handle initial state or "space-like" showers using a parton branching and re-combination scheme.

The model which shall be referred to as the standard Lund shower model, iteratively uses the branchings $g \longrightarrow gg$, $q \longrightarrow qg$, and $g \longrightarrow q\bar{q}$ as given by the Alterelli-Parisi evolution equations:

$$dP_{a\longrightarrow bc}/dt = \frac{\alpha_s}{2\pi}\int_{z_{min}(t)}^{z_{max}(t)} P_{a\longrightarrow bc}(z)dz$$

where the $P_{a\longrightarrow bc}$ are the Alterelli-Parisi splitting kernals, $t = ln(m_a^2/\Lambda^2)$ is the evolution parameter and z gives the energy sharing between b and c. Starting

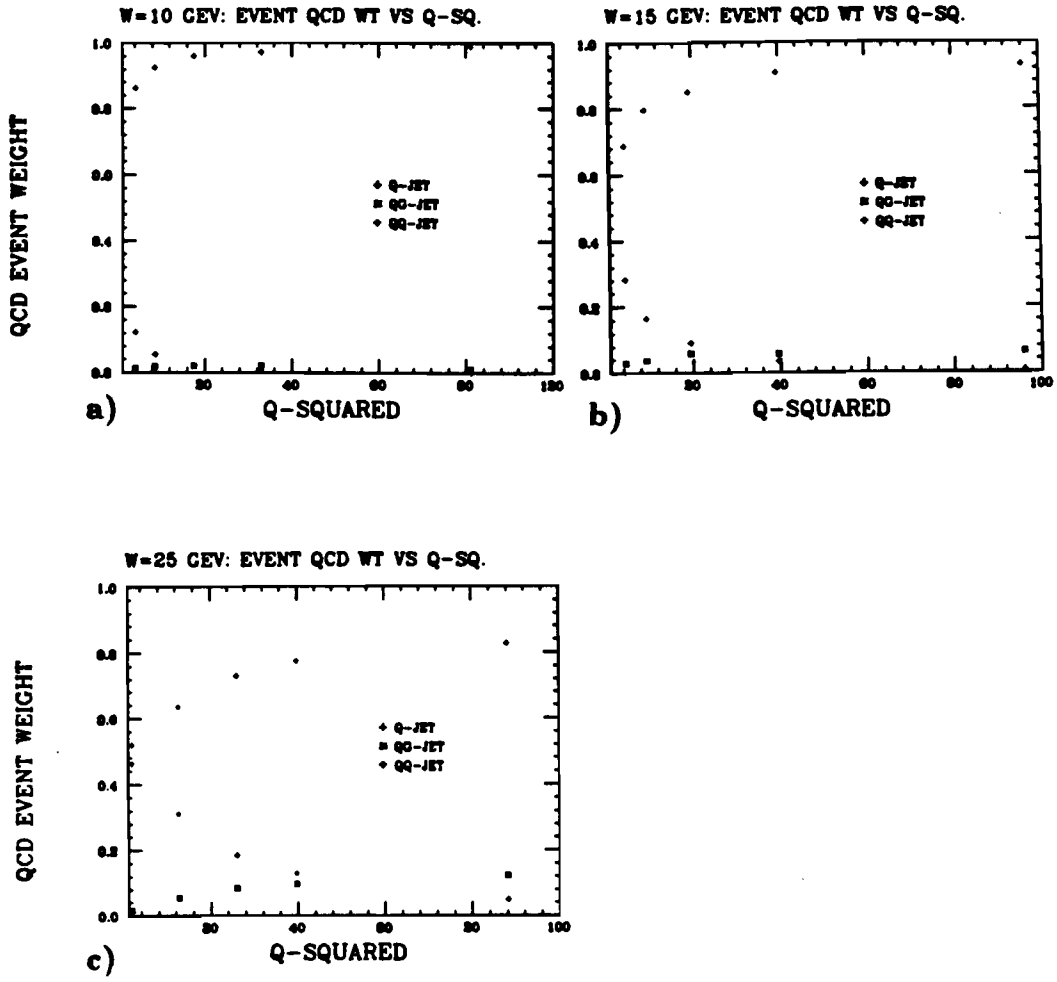

Figure 5. q,qg and qq event fractions for a)$9.5 < W < 12Gev$, b)$12 < W < 20Gev$, c)$20 < W < 29Gev$

at the maximum allowed mass for a, the iteration continues until a branching occurs. b and c may be allowed to then branch. The parton branching ends when a parton mass degrades below its minimum mass cut value. The final state or "time-like" shower is generated by a color flux tube or "string" fragmentation model.

An alternative Lund shower model is Ariadne[29,30]. In the Ariadne model, QCD cascades are generated by a color dipole consisting of a quark and an antiquark. A gluon is radiated from the initial dipole, and then decays into a $q\bar{q}$ pair(treated as a dipole as well). Thus, smaller and smaller dipoles are created until the transverse momentum of the system falls below a cut value. The gluon radiation is characterized by the differential cross section equation:

$$d\sigma/dx_q dx_{\bar{q}} ds_{Q\bar{Q}} \propto \frac{(x_q^2 + x_{\bar{q}}^2)}{(1-x_q)(1-x_{\bar{q}})s_{Q\bar{Q}}}(z^2 + (1-z)^2)$$

where $x_q, x_{\bar{q}}$ are the initial quark energy fractions and $s_{Q\bar{Q}}$ is the created dipole invariant mass. This equation assumes small values of p_T and $s_{Q\bar{Q}}$.

The assumptions of the Ariadne model are questionable for DIS. In particular, p_T can be large for DIS and is assumed to be small in Ariadne. Ariadne assumes a small soft gluon energy, but this is hard to measure. Finally, DIS hadronization is believed to begin with a quark-diquark state but Ariadne begins branching with a $q\bar{q}$ dipole.

§2.2.4 Kiselev and Petrov Model

In their model, Kiselev and Petrov[31,32] seek to create a model in which the hadronization of e^+e^- experiments and DIS experiments may be compared. This is not trivial since the processes are so different. e^+e^- differs from DIS in that complete annihilation of the initial state particles occurs and there are no initial state quarks. To accomplish this task, Kiselev and Petrov defined an effective W^2

$$W_{eff}{}^2 = \frac{\xi}{\xi + n} W^2$$

with

$$\xi = \frac{4}{3}\int_{Q_0{}^2}^{Q^2} \frac{\alpha_s k^2}{2\pi k^2} dk^2$$

where n= number of spectators[33] with

$$\lim_{z\to 1}(\text{valence quark distribution}) \propto (1-z)^{2n-1}$$

Due to the initial state differences mentioned, the model considers only gluon bremsstrahlung since the other leading hard QCD process, photon-gluon fusion, cannot occur in e^+e^-. The value of the quantity $d < n > /dQ^2$(slope of the mean multiplicity as a function of Q^2) as a function of W^2 is the only numerical prediction to arise from this model and will later be compared with data. The prediction is that this slope will be in the range .2 to .3 rising with W^2 in the kinematic range of E665.

§2.2.5 KNO Scaling

Assuming Feynman scaling(scaling with $x_F = 2p_z/W$ in the center of mass system), Koba,Nielson and Olesen(KNO) [34] predicted that multiplicity distributions should scale with available hadronic center of mass energy. If the final state probability for n charged hadrons to occur in an event is P_n and $< n >$ is the mean multiplicity, KNO scaling states that $P_n < n >$ is a function of $n/ < n >$ independent of any further explicit energy dependence.

§2.2.6 Kinematical Range of Experiments

The hadron multiplicity, kinematics and even flux can be measured. The principal measurement of this study is the charged hadron multiplicity. The kinematic range of E665 is presented in the context of previous experiments in terms of the energy available for the creation of hadrons(figure 6)[35].

§2.2.7 Review of Existing Data

There are previous experiments whose measurements, although not necessarily duplicated for deep inelastic scattering in this study, are nonetheless important to the interpretation of physics measurements carried out here.

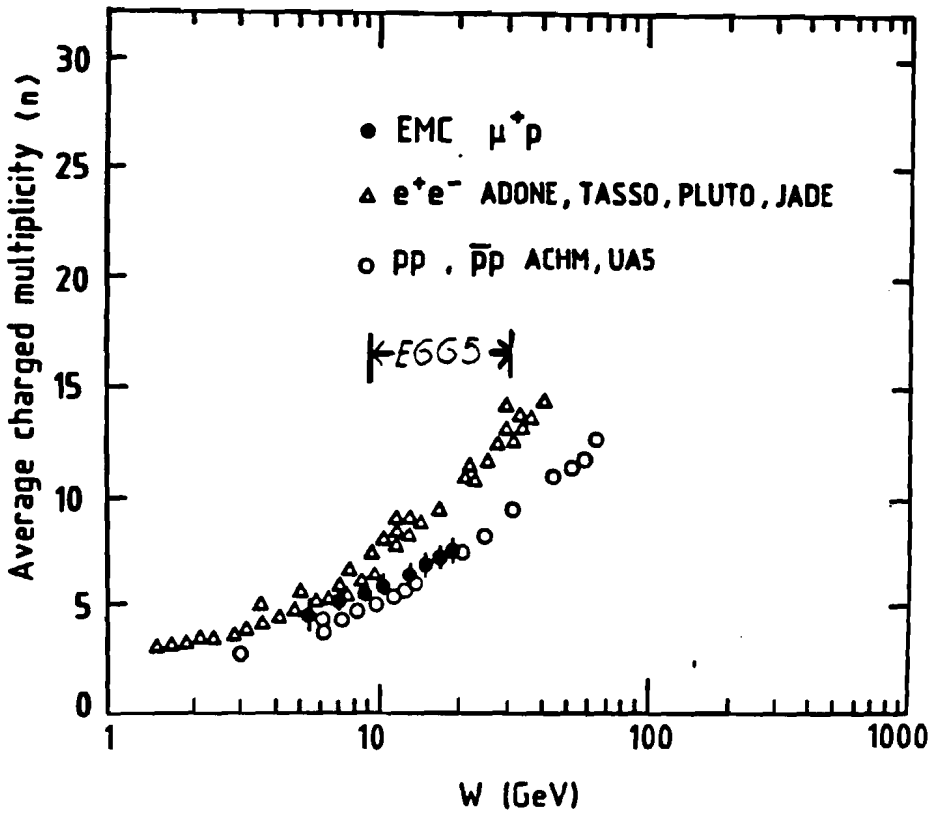

Figure 6. Charged hadron multiplicity as a function of $Ln(W^2)$.

Figure 7 shows $P(n) < n >$ vs. $n/ < n >$ measured by the UA5 540 GeV $p\bar{p}$ experiment[36] for different pseudo-rapidity($\eta = -ln(tan\frac{\theta}{2})$) values. This experiment interpreted the fact that the curves are different for different η as a violation of KNO scaling. Since the data in each multiplicity bin involves different center of mass energies for the $q\bar{q}$ system, it is not clear if these are really KNO scaling measurements.

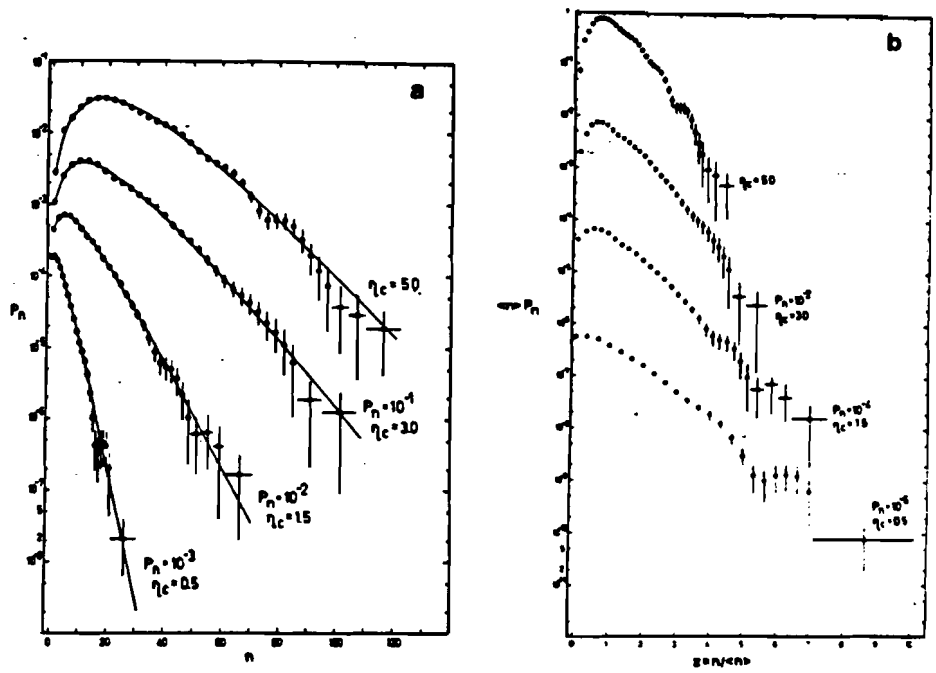

Figure 7. UA5 $p\bar{p}$ corrected charged multiplicity distributions in the pseudo-rapidity intervals $|\eta| < .5$, 1.5, 3.0 and 5.0 plotted in the variables a) P_n vs. n fitted to a binomial distribution and b) $< n > P_n$ vs. $n/ < n >$.

In the BEBC bubble chamber experiment at CERN using 350 GeV ν and 400 GeV $\bar{\nu}$ on a hydrogen target[37], dispersion($\sqrt{(< n^2 > - < n >^2)}$) and multiplicity were measured. In figure 8 is the forward and backward multiplicity. For negative X_F, the multiplicity is higher for ν. The dispersion relation is shown in figure 9.

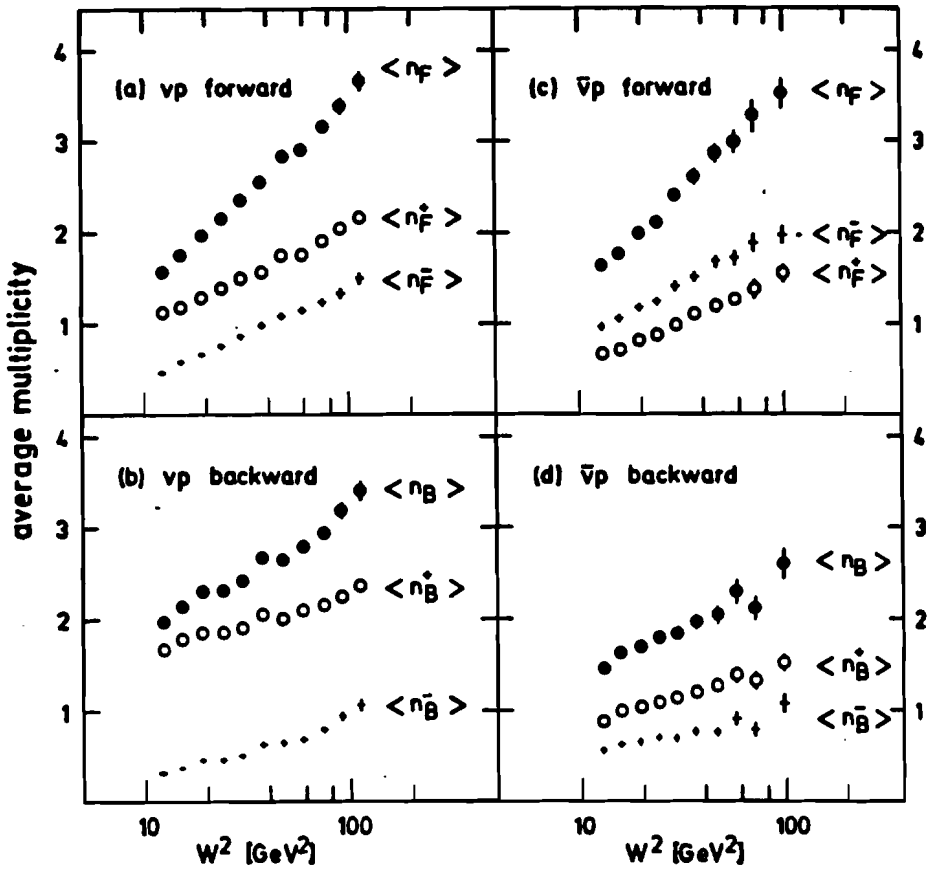

Figure 8. BEBC average multiplicity for a) νp with $X_F > 0$, b) $\bar{\nu} p$ with $X_F > 0$, c) νp with $X_F < 0$, d) $\bar{\nu} p$ with $X_F < 0$.

In the FNAL 15-foot bubble chamber, multiplicity for 350 GeV ν on neutron and proton targets was measured[38]. In figure 10, multiplicity for positive and negative X_F was measured. The same is shown in figure 11 with multiplicity by charge as well. Somewhat different multiplicities were observed for νp and νn charge multiplicities, particularly in the backward hemisphere.

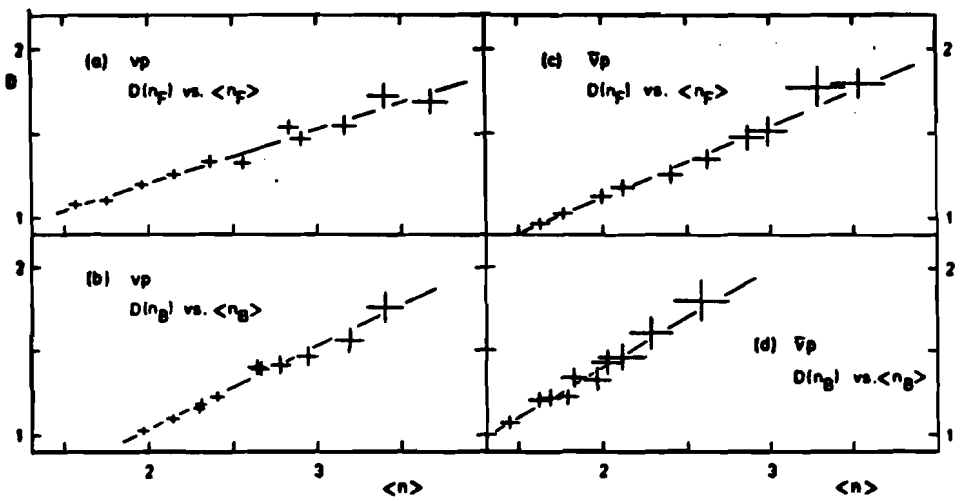

Figure 9. BEBC dispersion vs. multiplicity for a) νp with $X_F > 0$, b) $\bar{\nu} p$ with $X_F > 0$, c) νp with $X_F < 0$, d) $\bar{\nu} p$ with $X_F < 0$.

In the 200 GeV pp and p-nucleus experiment[39], multiplicity was measured for different regions of rapidity for forward and backward X_F. In figure 12 is shown charged hadron multiplicity distributions for various rapidity spans. In this experiment it was shown that a negative binomial distribution fit well over small rapidity regions.

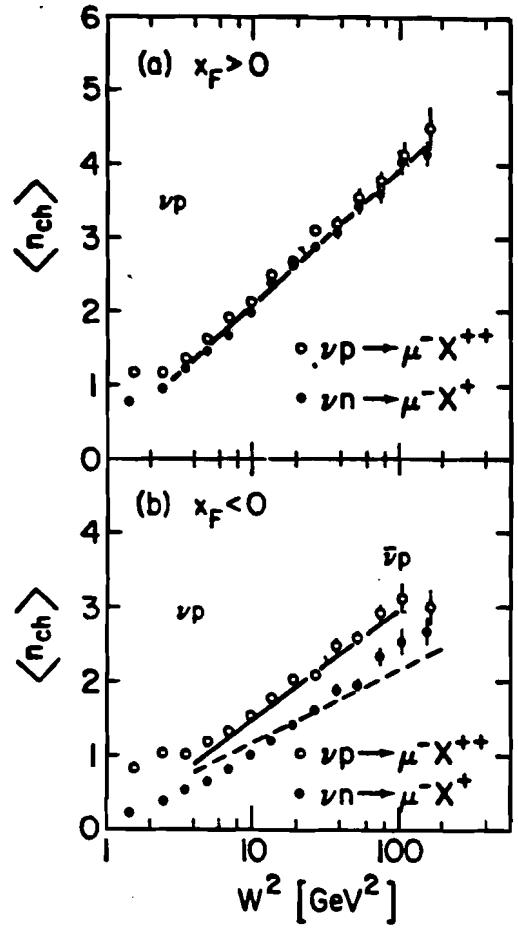

Figure 10. FNAL 15-*ft* bubble chamber average multiplicity for νp, νn with a) $X_F > 0$, b)$X_F < 0$.

Finally, in the most recent predecessor to E665, NA9[35,40] measured charged hadron multiplicity in 280 *GeV* μp scattering. The NA9 KNO scaling plot is figure 13 and supports the model. Charged hadron multiplicity for the forward and backward regions is plotted against W^2 in figure 14. In this figure, forward multiplicity is higher than backward and rises more steeply. Both increase linearly

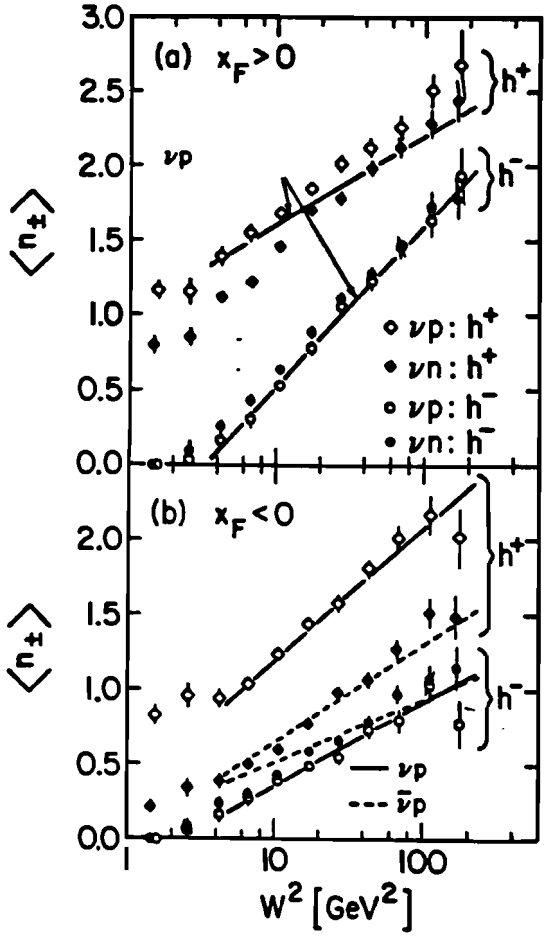

Figure 11. FNAL 15-ft bubble chamber average multiplicity for νp, νn with a) $X_F > 0$, b)$X_F < 0$ for positively and negatively charged hadrons.

with $ln(W^2)$. Charged hadron multiplicity is shown in figure 15 as a function of x_{Bj} and reveals a positive linear dependence with that variable for each of the W ranges shown.

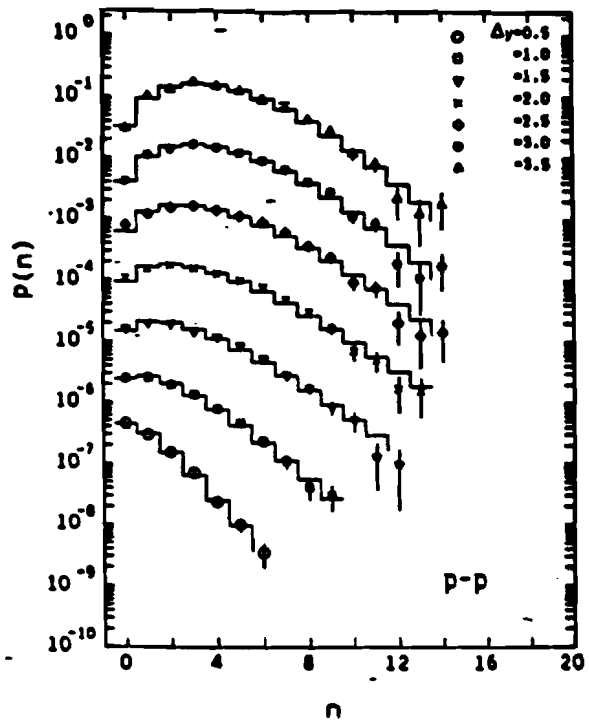

Figure 12. Average charged hadron multiplicity for 200*GeV* *pp* interactions. The data for the two hemispheres is averaged and negative binomial distributions are fit to each curve. The distribution for the widest horizontal span is shown in the ordinary scale with each consecutive curve scaled down by a factor of ten.

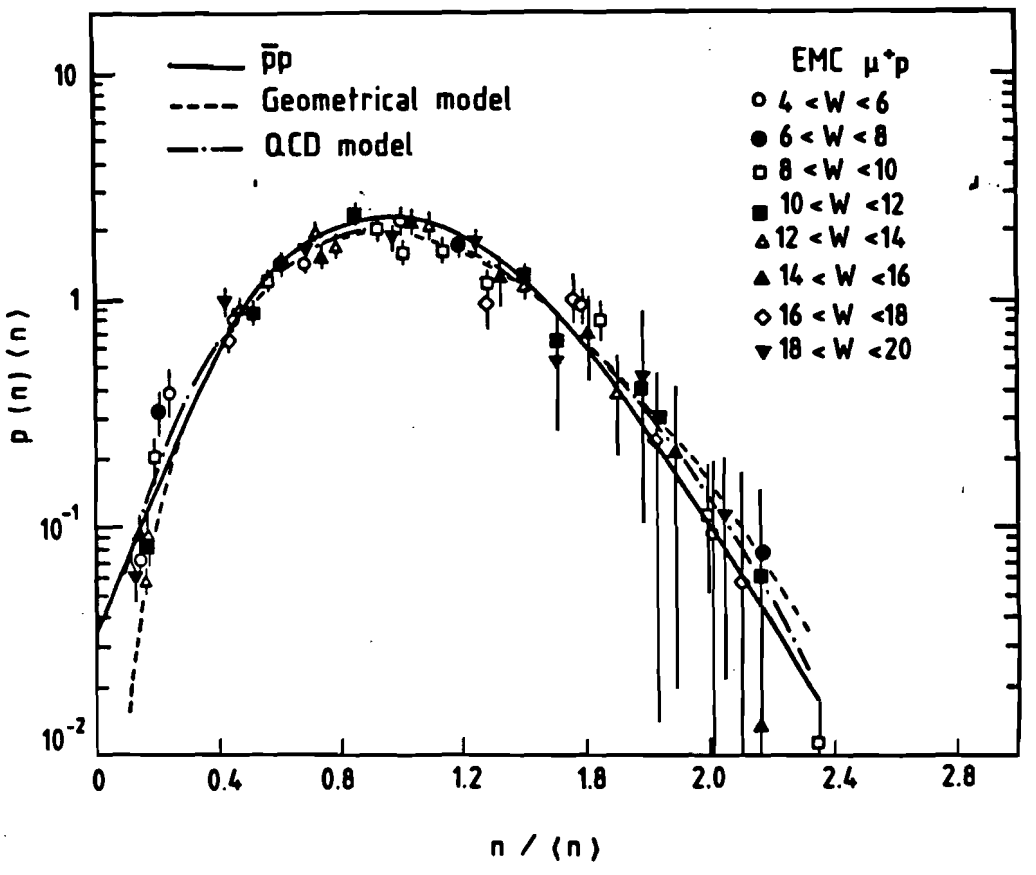

Figure 13. CERN experiment NA9 KNO scaling plot of $P(n) < n >$ vs. $n/ < n >$.

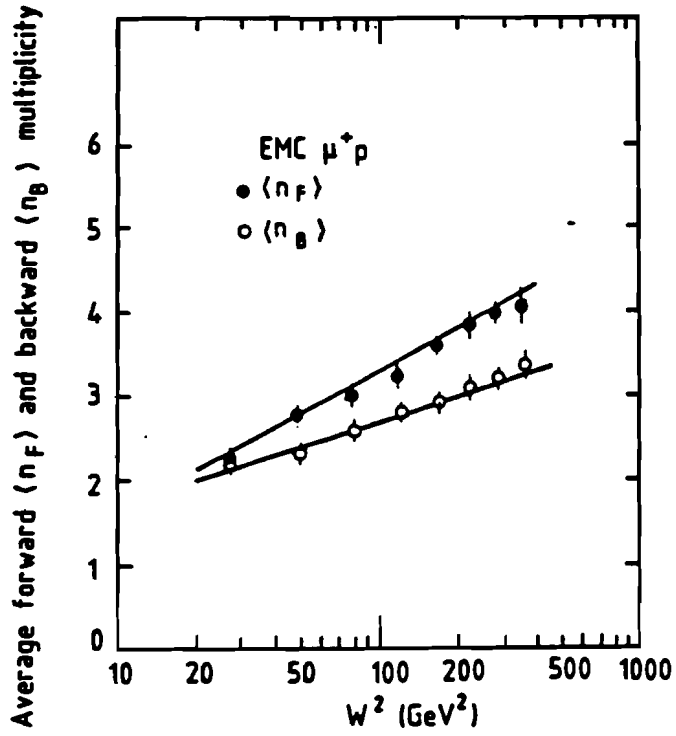

Figure 14. CERN experiment NA9 $< n >$ vs $ln(W^2)$ for $X_F > 0$ and $X_F < 0$.

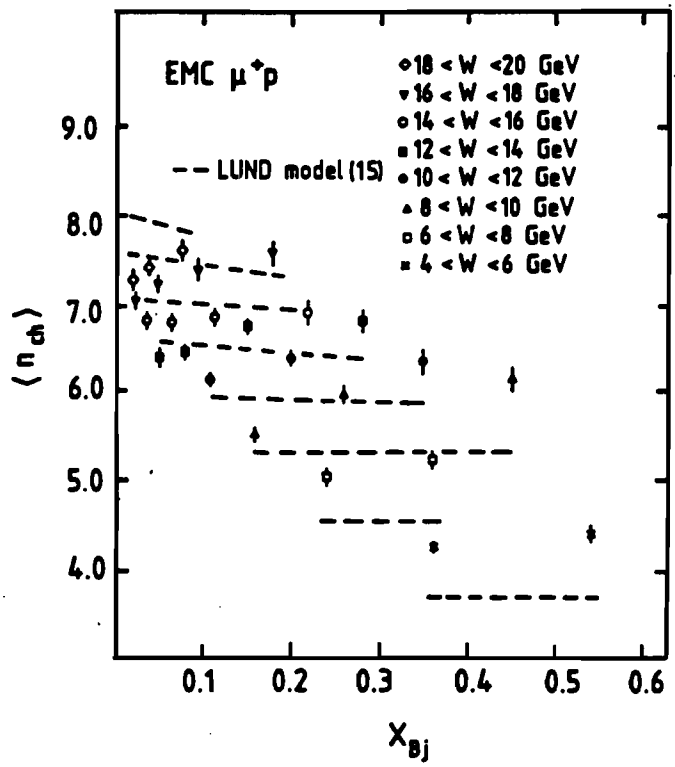

Figure 15. CERN experiment NA9 $< n >$ vs. x_{Bj} for different W.

Chapter 3 The Experiment and the Beam

E665 can be characterized as a focusing open spectrometer with particle identification and beam tagging. Data collection is initiated by a trigger requiring the tagged incident muon to scatter from the experimental nuclear target. Most of the information in this chapter and the next has been published as an E665 apparatus paper[41]. This source will be used too frequently to cite at each instance. The μ^+ beam is a few cm in diameter at the target and is produced from the decay of pions and kaons created by protons interacting in a fixed Be target more than a km upstream of the muon experimental hall. The beam momentum is selected by a 3 $mrad$ dipole magnet and measured by pairs of beam stations before and after the magnet.

Muons are produced for E665 by extracting an 800 GeV proton beam from the Tevatron and allowing it to impinge on a 48.5 cm Be target. The secondary kaons and pions are then momentum selected and are allowed to decay into muons and neutrinos over the remaining 1.1 km of the 1.5 km long NM beam line. To keep the particles from diverging out of the channel, the new muon(NM) beamline has focusing-defocusing quadrapole magnets arranged in a F0D0 structure. A Be absorber at the end of the decay channel absorbs any non-decaying hadrons. The muons alone emerge from this stretch of the NM line and are fed into a 366 m long halo-reducing F0D0 channel. The reduction of halo (those muons outside the nominal beam) is accomplished with thick iron pipe(Mupipe) surrounded by current coils which produce a toroidal magnetic field around the beam. The magnetic field radially deflects muons traversing the pipe while leaving the muon beam itself undisturbed. The halo to beam ratio drops from 1:1 to 1:4 with this method. The final beam momentum selection is done with a bending dipole magnet 80 m upstream of the muon experiment hall.

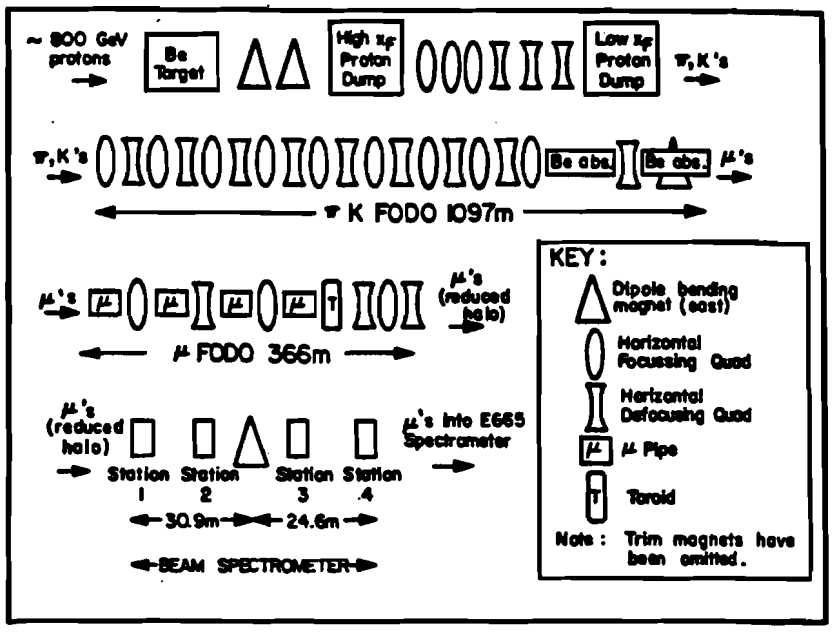

Figure 16. The NM beamline.

The 3 milliradian bend selects for E665 a beam experimentally determined to have a momentum of 486 ± 60 GeV by beam detection before and after the bend. The nominal beam during the 87-88 run was 3 cm in diameter with 20 million muons arriving in a 57 sec spill cycle. The beam arrived in spills lasting 20s of this minute. The 53MHz accelerator RF time structure is preserved in the muon beam giving RF buckets spaced in 19ns intervals(see section 5.1). Additional details are included in figure 16.

The muon beam strikes targets of liquid H_2,D_2 and gaseous Xe each of which is ≈13 cm in diameter and 1.15 m in length. Only one target is in the beam at a given time. E665 has two principal electronic triggers which start data collection: one for large angle muon scatter identification and one for small angle muon scatter identification. Hadron detection is present both in the vicinity of the

target and downstream. It consists of both particle identification and charged particle tracking. At the most downstream end of the experimental hall is the muon identification system which is crucial to the proper triggering of the data collection.

Chapter 4 The Apparatus

The detectors of E665 are divided into the beam spectrometer and the focusing spectrometer for the scattered muon and secondary particles. Extensive particle identification has been incorporated into the experiment as well. In particular, muons, photons and electrons as well as hadrons are identified. The detectors are described in this chapter according to the following groupings: the beam spectrometer, the vertex spectrometer, the forward spectrometer and the muon particle identification. The beam spectrometer and muon identification serve to reconstruct incoming and scattered muons while providing time information useful to triggering. The vertex spectrometer predominantly provides tracking and identification information about lower momentum and wide angle charged particles. The forward spectrometer provides tracking and identification information on higher momentum and forward going charged particles and photons. The E665 experiment provides precise momentum measurement of forward going particles using a multitude of parallel wire chamber planes in arrangement with two superconducting magnets. These magnets are opposite in field direction and have field strengths such that the scattered muon is focused. This is a strength of design which is useful for triggering. As well, particle identification has a strong presence in E665 including wide angle time of flight information, two gas threshold Cerenkov counters, an electromagnetic calorimeter, and a ring imaging Cerenkov counter(which can provide particle identification up to 100 GeV).

It is the E665 streamer chamber located inside the first of the two superconducting magnets and enclosing the target that provides almost 4π geometrical acceptance and is crucial to the physics analysis of this thesis.

§4.1 Beam Spectrometer

The beam spectrometer consists of four beam stations. Each has 6 multi-wire proportional chamber(MWPC) planes(PBT) as well as a vertically segmented and a horizontally segmented scintillation counter hodoscope(SBT). It should be noted that beam station 2 is missing its hodoscope with horizontal counters. Each hodoscope has 13 fingers graded to equalize the beam rate in each. Each PBT plane has 1 *mm* wire spacing and the planes are respectively oriented in reference to the vertical:+30°,0°, 90°,-30°,0°, and 90°. Two of the beam stations are before the first bending dipole of the beam line and two are after. The system of beam stations is designed to operate in a beam flux of 10^7 beam particles per second. The resolution in angle is about 10 μr and in momentum about 0.5% based on a constant bend of 3 *mr*. Studies indicate that the incoming beam muon reconstruction efficiency is in excess of 99% using the beam spectrometer in single muon events. Some more details are provided in table 1. A discussion of the role of these stations in triggering can be found in chapter 5.

Nominal Energy Tune	<momentum> LATRBEAM Trigger	Momentum spread (sigma)	LATB/P measured (typical)	LATB/B measured (typical)	HALO/LATB
500 GeV	486 GeV/c	60 GeV/c	$.55\times10^{-5}$	.88	.2
100 GeV	109 GeV/c	23 GeV/c	$.97\times10^{-5}$	.81	.37

B = 7/7 SBT
LATB = 7/7 SBT . NOT(SVW + SVJ) - Large angle trigger beam
HALO = (SVJ1 . SVJ2 . SVJ3) + (3/4 SPM. SVW. NOT(CVJ))
P = number of protons on Be target (Tevatron total $\sim 10^{13}$/minute)

Table 1. Beam characteristics and beam trigger requirements.

§4.2 Vertex Spectrometer

The vertex spectrometer consists of the central vertex magnet(CVM), the streamer chamber, the time of flight scintillator arrays(TOF), the Cerenkov

detectors(C0 and C1), the wide angle proportional tubes(PTA) and the vertex proportional chambers(PCV).

§4.2.1 Vertex Spectrometer Particle ID

The Cerenkov detectors C0 and C1 are located just downstream of the PCV and follow one another. The gas Cerenkov counters operate on the principle that the number of photons resulting from the passage of a charged particle whose velocity exceeds that of light in the medium will be inversely proportional to $1/\beta^2$. Combining this information with forward tracking momentum information permits particle identification by mass calculation. A mirror-phototube arrangement for the collection of these photons exists in each. The time of flight detector relies on the time information provided by beam station 1 and that of its hodoscope arrays at wide angles east and west of the beam but downstream of the target. Combining geometrical knowledge with time difference information yields the particle velocity while momentum information from the streamer chamber permits calculation of the mass which completes the identification. The time of flight detector is sensitive to charged particles with momentum less than a few GeV while the Cerenkov detectors are sensitive to those above a few GeV up to about 30 GeV(see figure 17).

The C0 Cerenkov counter consists of a radiator of 90 cm effective length with two mirror planes which reflect light above and below the median plane of the detector into 144 Winston- Hinterberger cones. Each of these cones focuses light into a magnetically shielded phototube.

The C1 Cerenkov counter is an atmospheric Cerenkov counter with a 1.5 m effective radiation length and a 1.09×1.43 m entrance window. Its mirror arrangement focuses light onto 58 magnetically shielded phototubes.

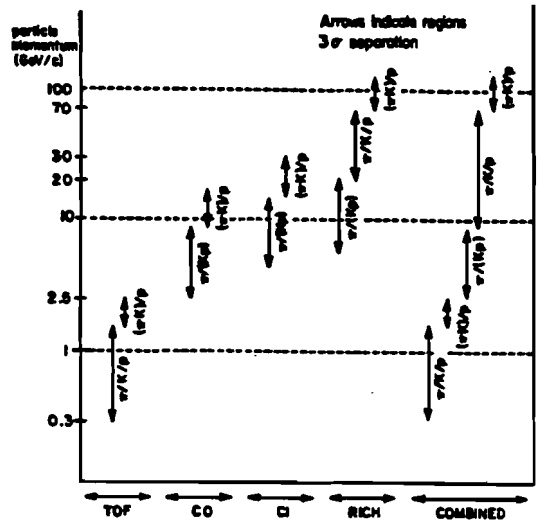

Figure 17. Particle ID momentum range.

The time of flight system consists of two hodoscope walls each of which has 38 counters covering a $4.2m \times 1.6\ m$ sensitive area. These arrays are located on the east and west sides of the target at wide angles. A hodoscope placed in the beam in front of beam station 1 provides an incident muon time and a N_2 laser provides direct hodoscope calibration.

§4.2.2 Vertex Spectrometer Wire Chambers

The vertex spectrometer wire chambers cover the region at wide angles($\pm$ 30°) as well as the forward region. The wide angle tracking provides more precise position information than the scintillators in the TOF. The vertex forward wire chambers PCV provide spacepoint information close to the target which

improves the resolution of the vertex when combined with further downstream wire chamber information.

Behind each of the TOF hodoscope walls are four 2 $m \times 2$ m active region wire chamber planes,PTA. Their respective orientations with respect to the vertical are: 0°, 90°, +45° and -45°. The wire spacing is 12.7 mm in each plane.

The PCV detector consists of six wire chamber planes with a sensitive area of 2.8 $m \times 1.0$ m. The detector is directly downstream of the streamer chamber. The planes have the following respective orientations: horizontal,+45°, +18.5° ,-18.5° ,-45° and 0°. The wire spacing is 2mm in each plane.

§4.2.3 The Streamer Chamber

Within the CVM and enclosing the target is the streamer chamber[42] which physically consists of a box with an active volume of 2.0 $m \times 1.2$ $m \times 0.7$ m and cameras mounted at the following locations with respect to the chamber center: (.307,.482,3.722), (-.298,.004,3.707),(.297,-.482,3.695). All cameras are focused to the center of the detector. A two stage image intensifying system is present as well to maximize the quality of the tracks recorded on film. The demagnification between chamber and film is $\frac{1}{66}$ at the median plane.

The charged tracks become visible in the following way[43]. As a charged track passes through the helium gas in the chamber, it ionizes it along its path. The streamer forms when exposed to a powerful electric field stretching the region of ionization vertically along the direction of the potential drop. The streamer may be a few mm in length while about 1 mm in width. When the field is removed, the electrons are re-captured by the helium ions and light is emitted. An electric field pulse is provided by a three gap system permitting the insertion of targets in the beam. The high voltage pulses applied to the

electrodes are $\pm$ 350 kV,10 ns long, and take 400 ns to generate. These pulses are generated by a Marx and Blumlein system. The gas mixture has been tuned such that the track ionization trail lasts $\approx 1\ \mu s$. The dead time of the streamer chamber is large compared to that of wire chambers due to the fact that the Marx generator requires about half a second to recharge. The normal operation of the system has a trigger rate of 1.5 s^{-1}.

Some track detection characteristics arising from the nature of the streamer chamber are worth noting. The two track resolution is approxiamtely 3 mm in space and is dominated by the apparent 1 mm streamer width. Single track position measurements are accurate to roughly 850 μm. The field strength coupled with the track position resolution yields a momentum resolution of $\sigma p/p = p/100$ where p is in GeV/c. Figure 18 is a typical hydrogen target streamer chamber picture.

§4.3 The Forward Spectrometer

The forward spectrometer consists of the Chicago cyclotron magnet(CCM), the proportional chambers(PC and PCF), the drift chambers(DC), the small angle proportional chambers(PS), the electromagnetic calorimeter(CAL) and the ring imaging Cerenkov counter (RICH).

§4.3.1 Forward Spectrometer Wire Chambers

The forward spectrometer consists of six wire chamber detectors. Among the wire chamber detectors are proportional counters(PC) and (PCF);2 banks of drift chambers(DCA) and (DCB); as well as 2 small proportional counters (PSA) and (PSB). The PCV and PC provide tracking from just downstream of the target to the CCM. The PCF tracks the charged particles through the

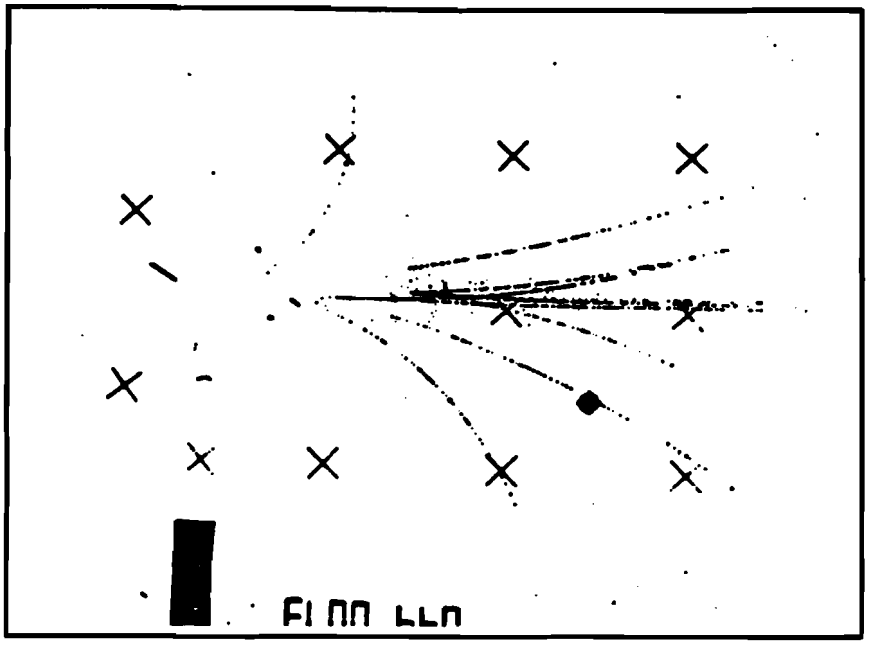

Figure 18. Example of a hydrogen streamer chamber picture.

CCM and provides the only data from which forward track momentum may be extracted. The DC and PS wire chambers provide especially precise tracking information which is crucial to reconstructing complete tracks. Their location permits efficient matching of forward spectrometer tracks to muon spectrometer track segments. The details of construction, placement and operation are given below.

The PC proportional chambers are located just downstream of C1 and are not exposed to significant magnetic fields from either of E665's magnets. The detector is divided into 3 sets of 4 planes. Each plane has a sensitive area of 2 m ×2 m with an anode wire spacing of 3 mm. The planes contain the same gas mixture as PCV. Each plane in a package has a different wire orientation with respect to the vertical. The values are: 0°, 90°, 28° and -28°. The average efficiency is 85 % outside the beam region according to halo muon data.

The PCF proportional chambers are located downstream of the PC detector and reside inside the CCM magnet. The detector consists of 5 sets of 3 planes whose wire orientations with respect to the vertical are: 0°, 15°, and -15°. The spacing of the 20 μm wires is a constant 2 mm and the anode to cathode gap is 6.4 mm. The total sensitive area is 2 m×1 m for each plane set. The gas mixture used by the detector is 80 % argon, 19.7 % carbon dioxide and .3 % $C\ Br\ F_3$. The typical plane operates at 3.8 kV. The above leads to an average non-beam region efficiency of 95 %.

There are 8 DC drift chamber packages. These each consist of 8 planes which have the following wire orientation with respect to vertical: 4 planes at 0°, 2 planes at 5.758°, and 2 planes at -5.758°. Each plane has 50.8 mm wide cells along the drift direction and cells 9.6 mm along the beam. There are 4 packages just upstream of the RICH with a sensitive area of 2 m×4 m and 4 just downstream of the RICH with a sensitive area of 2 m×6 m. The DC's are deadened in the beam region which is covered by PSA and PSB. The average efficiency outside the beam region is 95 % ± 4 %.

The PSA and PSB are small angle MWPC packages each consisting of 2 identical 4 plane detectors. PSA is located just downstream of the most downstream DC and the identical PSB is located just downstream of the RICH. The

first 4 plane detector package is mounted in the following way: 1 plane has a vertical wire orientation, 1 is horizontal, the next 2 planes are arranged as the first 2 but offset .5 *mm* with respect to them. The second 4 plane package is mounted at a 45° angle with respect to the first. All planes have an active area of .128 *m* square and 1 *mm* wire spacing. Both PSA and PSB operate at 3.1 *kV* and use a 50-50 mixture of argon-ethane. Using non-interacting beam, the average single plane efficiency was found to be 90 %.

§4.3.2 Forward Spectrometer Particle Identification

The RICH identifies charged particles in the 30 to 100 *GeV* range by reconstructing the Cerenkov radiation light cone emitted by these particles as they pass through at velocities exceeding that of light in the RICH's gas.This detector consists of a roughly 6 *m* long radiator vessel, 33 spherical mirrors covering an active area of 2.7 $m \times 3.7$ *m*, and a photon detector with a 40 $cm \times 80$ *cm* active area . The mirrors form some fraction of a sphere and have an average focal length of 4.85 *m*. When a relativistic particle passes through the detector, Cerenkov light reflected from the mirrors forms rings at the focal plane where the photon detector is mounted. The photon detector consists of a calcium fluoride window followed by a drift space and then a wire proportional chamber. The proportional chamber is made up of a cathode wire plane whose wires lie at 500 μm pitch, an anode plane of wires with 2 *mm* spacing, and a second cathode plane consisting of 10800 individually 3.8 $mm \times 12$ *mm* read out pads. Analog zero-suppression is applied before pad and anode readout with only signals above a pre-set threshold digitized. The gas used by the chamber is 99.3% methane and 0.7% triethylamine (TEA).

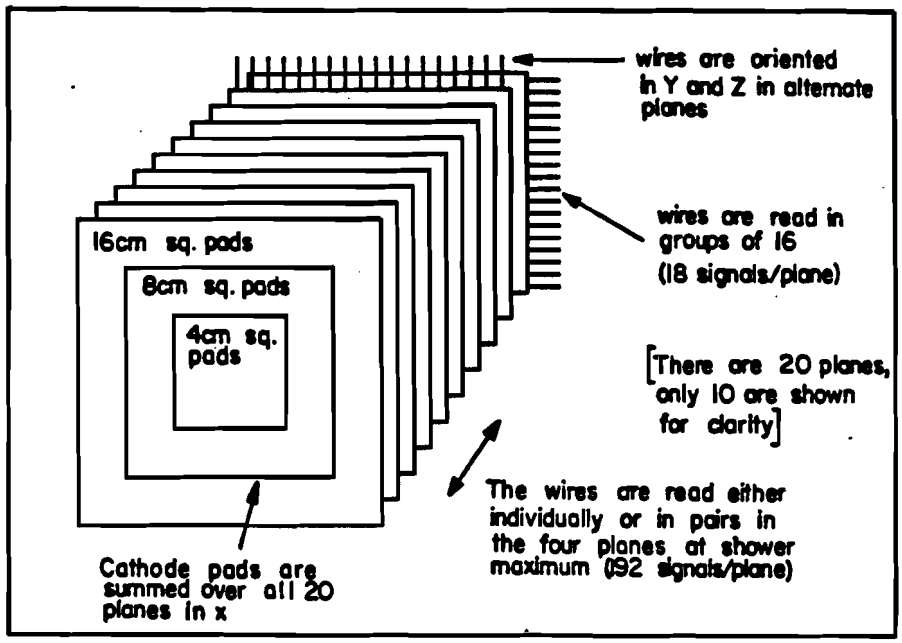

Figure 19. The E665 electromagnetic calorimeter.

CAL is a photon and electron particle identification counter which reconstructs the energy of these particles due to their tendency to shower more readily than hadrons or muons. The twenty planes of one radiation length Pb located between the wire chamber planes of CAL ensure that nearly all photons and electrons will relinquish all their energy electromagnetically showering in the calorimeter. The shower energy is summed up by CAL's pad towers(see figure 19 and the description below). Photons are distinguished from electrons by forward spectrometer wire chamber tracking information.

As mentioned, the calorimeter consists of 20 wire chamber planes each separated by a plane of 1 radiation length thick lead. The active area of the detector is 3 $m \times 3$ m. The wire spacing is 1.04 cm. The data is read out in groups of sixteen adjacent wires. In the 4 planes closest to the shower maximum, data is read out

from single wires in the central 1 m of the detector and from pairs outside that region. The calorimeter has been constructed such that it alternates between planes with horizontal and vertical wire orientation in consecutive planes. The wire chambers are operated at 2.0 kV and 2.15 kV in proportional mode. Two different high voltages are used because some wire chambers have 50 micron wire and some have 63 micron wire. A 50% argon-50% ethane gas mixture flows through the chambers. The most useful source of shower energy and location information is not the summed anode, but the cathode pad tower readout. The cathode planes are split into 1188 pads and read out as longitudinal towers by summation over all planes. The pads are 4 cm square in the central .5 m square area of the detector, 8 cm square in the region outside the central region but inside the region defined by a centered square 1 m on side, and 16 cm square outside that. All data is read out using the FASTBUS data acquisition system. Isolated particles can be resolved down to ~5 mm using the pad information and ~3 mm using the wire information. The 2 γ resolution spatial resolution in the central part of the detector is ~12 $cm(.4mrad)$ using pad information. Based on a measured π^0 peak and electron beam test data, the energy resolution is $\sim 7\% + 45\%/\sqrt{E}$ where E is the γ energy in GeV.

§4.4 Muon Triggering and ID Apparatus

The muon spectrometer consists of the muon proportional tubes(PTM), the large angle scintillation counters(SPM) and the small angle scintillation counters(SMS). The muon spectrometer is separated from the forward spectrometer by a 3 m thick iron hadron absorber. There are 8 PTM planes- 4 with vertical wire orientation, 4 with horizontal. Each plane is paired with an orthogonal partner and separated by 90 cm thick concrete walls from its closest neighbor pair. These walls serve to absorb hadrons and electromagnetic showers. Along with each PTM pair comes a similar pair of SPM and SMS counters. This absorber-wire chamber-hodoscope configuration permits the clean identification of muon tracks.

The SPM detector consists of 4 planes of scintillation counters. All but the central counters are 1.5 $m \times 0.5$ $m \times 0.025$ m. The central counters are all 1.4 $m \times 0.28$ $m \times 0.025$ m. The counters overlap their neighbors by 12 mm and cover a wall of 3 $m \times 7$ m excluding a 20 cm square hole in the center.

The SMS scintillation counters consist of 4 sets of 2 planes divided into 16 equally sized "finger" counters and cover the SPM hole. Each set of 2 has 1 vertical plane and 1 horizontal. Each of the 14 inner "finger" counters is 13.2 mm wide while the 2 outer ones are 19.6 mm wide. The adjacent counters overlap 3 mm.

The PTM muon proportional wire tubes consist of 4 pairs of 1 vertical and 1 horizontal plane. Each plane of a pair has an active area of 3.6 $m \times 7.2$ m and is constructed as a double layer of aluminum tubes whose width is 25.4 mm and whose wall thickness is 2 mm. The layering of wires yields an effective 12.7 mm pitch with no dead region between the tubes. The typical plane high voltage is 2.7 kV and the gas mixture is 50-50 argon ethane. The beam region of the PTM

planes is deadened. Studies with halo beam reveal the single plane efficiency to be 95 %.

Chapter 5 Triggers

There is not enough computing time available to record the state of the detector system continuously. This coupled with the fact that the muon-nucleus cross section is quite low where the LAT acceptance is high ($\approx$ 90*nanobarns* overall with acceptance included) means that we must take data selectively. Thus, the data acquisition system is triggered only when an event of physics interest is believed to have happened. The goal of the E665 trigger is to mark the presence of a scattered muon resulting from a DIS. E665 has triggers which detect this occurrence using information from the muon identification system directly. To ensure a fast trigger, the incoming and scattered muons are triggered with scintillation hodoscopes. There are three principal pieces of evidence which indicate the presence of a scattered muon. The first is presence of a beam muon on a trajectory which goes through the target. The SBT hodoscopes described in section 4.1 provide this information. The second indicator is the lack of a muon in the SMS hodoscopes(section 4.4) which cover the non-interacting beam region downstream of the iron absorber. The third piece of evidence is the presence of a muon outside the non-interacting beam region downstream of the iron absorber. This is ascertained from the presence of hits in the SPM hodoscopes which cover a 3 $m \times 7$ m region excluding a 20 cm square hole covered by the SMS counters. It should be noted again for clarity that there are 4 SMS/SPM hodoscope stations interspersed with 90 cm concrete walls in the muon identification system. Along with the iron absorber, these walls absorb hadrons and electrons which would otherwise produce trigger impairing hodoscope hits.

Triggering is not an easy game since various processes can produce "fake" triggers or triggers which do not result from DIS. Bremsstrahlung and muon-electron scattering certainly cause the muon to scatter but are electromagnetic(

not DIS processes). A different sort of false trigger results from timing problems. Muons arrive in "buckets" separated in time by the tevatron proton radio frequency(PLRF). Two muons from different buckets can accidentally conspire to satisfy the beam trajectory requirements necessary to trigger while neither independently does. Since there is a requirement that a certain number of beam station hodoscopes fire, it's possible for an out-of-time muon to help satisfy this condition. In particular, halo muons(muons which accompany the beam outside the usual phase space) are sometimes displaced far enough away from the center of the beam so that they do not veto. A halo muon in combination with an "in-time" beam can often produce such an "accidental". As well, an effort has been made to avoid losing good triggers due to muon spectrometer beam region vetoing by a muon from another bucket.

§5.1 PLRF Tevatron Radio Frequency Beam Signals

The tevatron proton RF frequency of 53.1047 MHz is inherent in the muon beam. Since protons are used to produce the muon beam, it is natural that the proton bunching carry over to it. The reference plane signal PLRF is provided by 4 5.08 cm square 1.27 *cm* thick NE110 scintillation counters located downstream of the last SPM counter. The jitter associated with this signal is 1.05 ns. The smallness of this number is important since all of the experiment's triggers require a PLRF coincidence. Note that this part of the trigger is thus, not responsible for trigger timing problems.

§5.2 The Halo Veto System

The first consideration in the trigger beam definition is that of removing halo muons or muons which do not pass through the target. These must be removed

in the beam definition since they are already displaced from the beam and some fraction of these will thus not veto. Thus, if coupled with a beam muon which fails to set the beam veto, then a "fake" event trigger occurs. There are enough halo muons naturally accompanying the beam to saturate a trigger with non-DIS events. To detect the presence of halo muons, the SVJ and SVW scintillation counter systems were built. The SVJ counters are located in the beam stations while the SVW counters are located 6m upstream of the experimental target.

The SVW large scintillation counter wall consists of 28 1.5 $m \times .55$ m counters approximately 5 m upstream of the CVM center. The central 4 counters are constructed so that the beam may pass through a 25 cm square hole. To eliminate extraneous hits in the counters arising from low energy particles, a 5 cm steel wall shadows SVW from such particles.

The SVJ scintillation veto counters consist of 3 pairs of counters covering a 50 cm square region centered on the beam. One pair is located at each of beam stations 2 through 4. Each SVJ pair possesses an adjustable aperture permitting flexibility in one's definition of halo in any trigger using this counter system.

§5.3 The LATB Beam Trigger and RLAT Normalization Trigger

As described in the introduction to this chapter, one must carefully select beam muons which are on a trajectory consistent with hitting the target. The incoming beam condition used as part of the large angle muon scatter trigger(LAT) is the LATB trigger. The LATB definition is satisfied when there is a hit in all 7 SBT hodoscopes in coincidence with the PLRF signal while there is no hit in any of the SVJ or SVW hodoscopes(see the halo veto section). The latter condition removes halo muon events. The RLAT trigger is the LATB in

coincidence with a random number generator synchronized to the RF. Thus, the LATB trigger is randomly sampled at a pre-scaled rate in order to measure the fraction of beam muons satisfying the beam conditions of the LAT and is written to tape as RLAT.

§5.4 The Large Angle Trigger(LAT)

One of the two principal physics triggers used by E665 is the large angle scattered muon trigger. The phase space of the beam defined by LATB and used by the LAT is such that unscattered muons hit the SMS hodoscopes behind the iron absorber. The LAT is defined as LATB in coincidence with hits in 3 out of 4 SPM planes and in anti-coincidence with presence of a hit in any of the SMS counters. The LAT acceptance as functions of Q^2 and X is shown in figure 20a.

§5.5 The SATB Beam Trigger and RSAT Normalization Trigger

The incoming beam condition used as part of the small angle muon scatter trigger(SAT) is the SATB trigger. Part of the SATB trigger condition is satisfied when the incoming muon fires a combination of SBT hodoscopes determined by the SAT hardware look-up table to be acceptable. Qualitatively, those combinations which have hits in the high resolution central part of each SBT hodoscope are deemed "acceptable" by the look-up table. The PLRF signal must be in coincidence with the condition described to satisfy SATB completely. If the SATB is also in coincidence with the RF synchronized random number generator then it is a RSAT. Thus, the SATB trigger is randomly sampled at a pre-scaled rate in order to measure the fraction of beam muons satisfying the beam conditions of the SAT and is written to tape as RSAT.

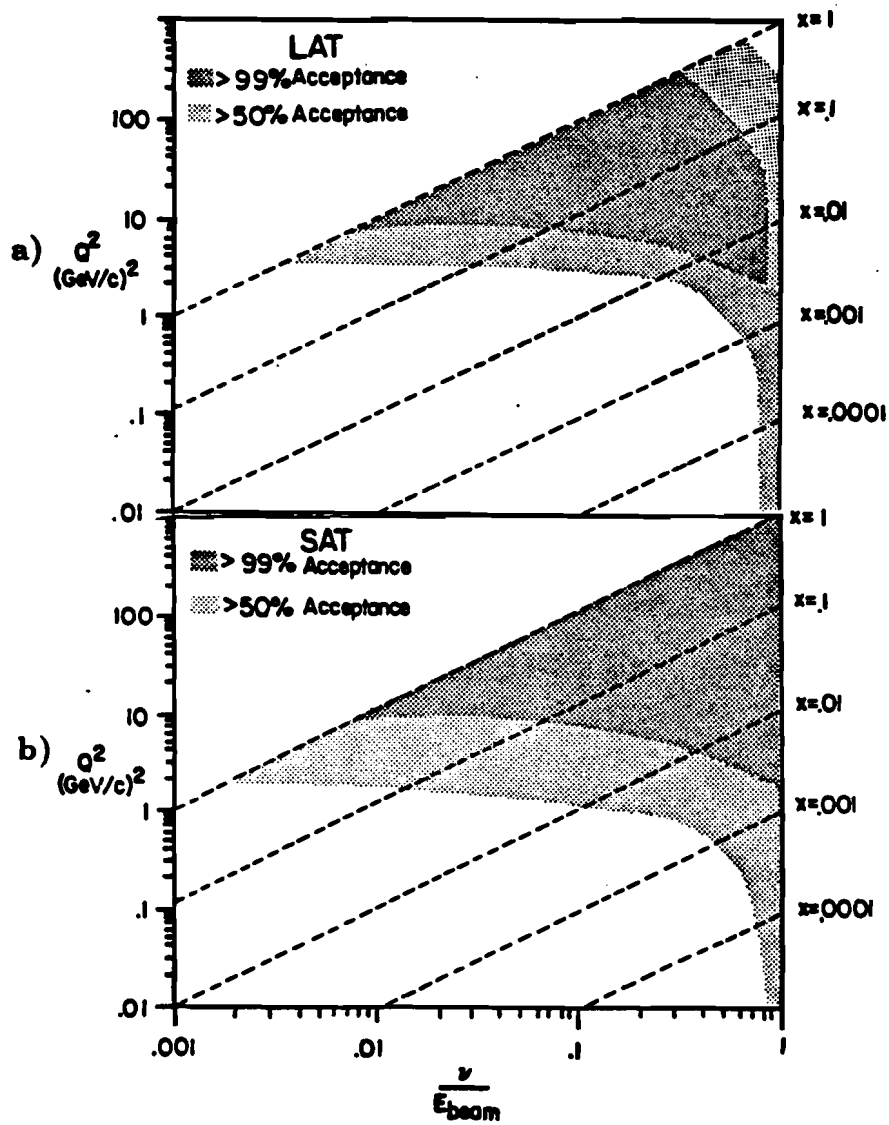

Figure 20. a)Large,b)small angle trigger acceptance.

§5.6 The Small Angle Trigger(SAT)

The goal of the SAT is to detect muons which scatter at angles so small that the scattered muons themselves would veto in the LAT. To trigger, the SAT uses the directional information obtained from the SBT to calculate an impact point for the beam muon in the SMS. A veto region using at least 3 of the vertically

oriented SMS hodoscope fingers is then defined by a ECL hardware look-up table. Only a coincidence between the veto described and SATB is required to satisfy the SAT trigger condition. The acceptance of SAT as functions of Q^2 and X can be found in figure 20b.

§5.7 The FCAL Electromagnetic Energy Trigger

A completely independent trigger used primarily for normalization purposes is the calorimeter energy trigger(FCAL) which requires a certain level of CAL energy deposition to fire. The FCAL trigger is satisfied when the total calorimeter energy deposition excluding a 32 cm wide cross centered on the beam is above a ≈ 60 GeV threshold and PLRF are in coincidence. Since the calorimeter is response time limited, FCAL fires only if no muon was present in the last 15 RF buckets.

§5.8 The HALO Trigger

To trigger on muons outside the normal beam phase space, the HALO trigger was created. This trigger is useful for monitoring alignment and the efficiency of detectors in the region away from beam. The trigger is defined to be the coincidence of the following: 3 of 4 SPM hodoscope planes record hits, PLRF signals, and the upstream veto wall (SVJ,SVW) fires.

§5.9 The PCN Coincident Streamer Chamber Triggers

Due to the deadtime limitations of the streamer chamber, an attempt was made to place a trigger in coincidence with the LAT and SAT which would enhance the fraction of deep inelastic event triggers which fire the streamer

chamber. The PCN multiplicity trigger is that trigger. It consists of a requirement that in the 3 PC planes with horizontal wire orientation, at least 2 wires outside a $\pm$ 9.6 cm band with repsect to center have hits. The acceptance of the LAT $\cdot$ PCN trigger(using which most of the data was taken) is shown as functions of Q^2 and W^2 in figure 21.

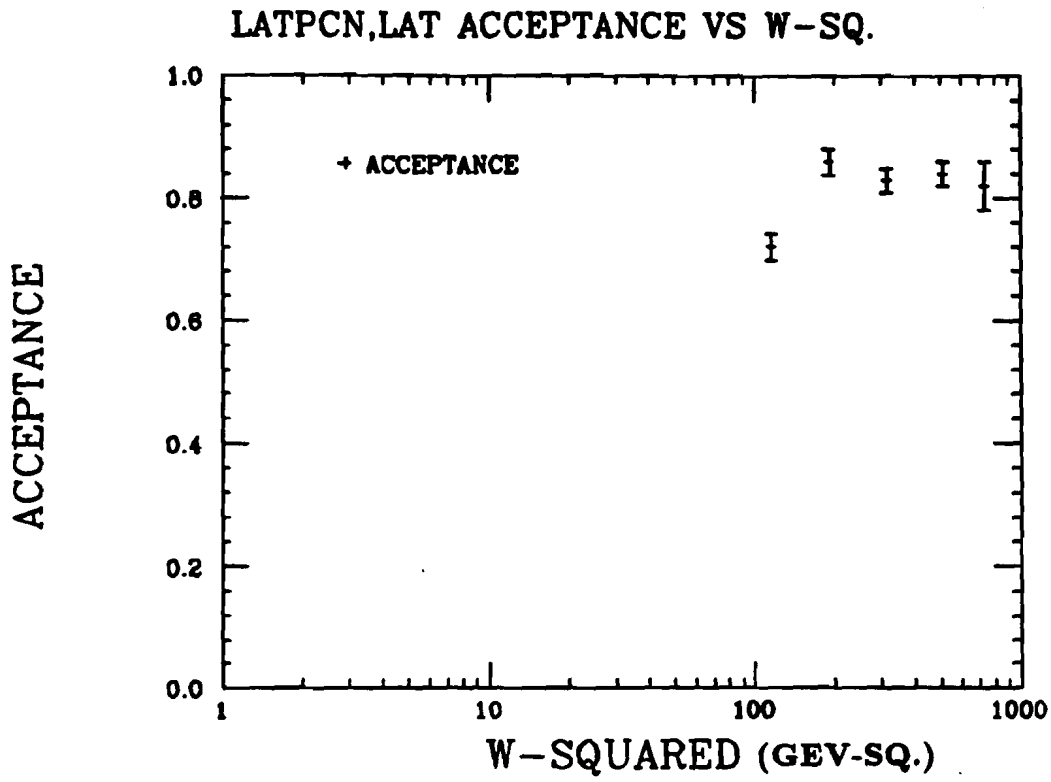

Figure 21. LAT · PCN trigger acceptance.

Chapter 6 Data and Data Acquisition

The E665 raw electronic data sample is given by trigger and target type in table 2[44].

The electronic data sample for which a streamer chamber picture exists is given in table 3[45]. It should be noted that the raw data has been split such that the categories of table 2 have actually been re-written to tape as separate data sets. The electronic data for which pictures exist has been split off from the rest of the raw data as well but not to the level of target and trigger type. Thus, the data of table 3 exists as a single data set.

Reconstructed Electronic Data Sample

Beam Energy	Target	Trigger	Triggers
500 GeV	H_2	LAT	708k
500 GeV	H_2	SAT	613k
500 GeV	D_2	LAT	1,479k
500 GeV	D_2	SAT	315k
500 GeV	Xe	LAT	1,113k
500 GeV	Xe	SAT	795k
100 GeV	D_2	All	0k
100 GeV	Xe	All	0k

Table 2. Electronic data sample statistics.

E665 Streamer Chamber Trigger Data

Beam Energy	Target Type	Number of Triggers
$500GeV$	H_2	53,370
$500GeV$	D_2	91,700
$500GeV$	Xe	72,600

Table 3. Streamer chamber data sample statistics.

§6.1 Streamer Chamber Data

The frames of SC data taken during the 1987-1988 run are distributed for measurement according to table 4[45].

It was decided by E665 that physics interest and time considerations dictate that scanner measurement(see next chapter) would take place only on frames with $Q^2 > 1GeV^2$, $0.9 > y_{Bj} > 0.1$, and $-9.6 > X_{primary\ vertex} > -12.4m$. Film

E665 Streamer Chamber Film Distribution

Film	Fermilab	Krakow	Munich	Undistributed	Total
500 GeV H_2	42,000	16,000	61,000	0	119,000
500 GeV D_2	55,000	32,000	94,000	0	181,000
500 GeV Xe	48,000	56,000	50,000	0	153,000
100 GeV D_2	0	0	0	16,000	16,000
100 GeV Xe	0	0	0	36,000	36,000

Table 4. Distribution of streamer chamber film by institution.

measurement is a human task and the 3 institutions- FNAL,MPI and Krakow, can measure only 1500 frames per month combined. After accounting for the kinematics cuts above, the film distribution is as shown in table 5.

§6.2 Electronic Data Acquisition (DAQ)

The E665 chain of data acquisition is shown in figure 22.

There are 4 steps involved in getting data from detector to tape. These are: readout,storage, event concatenation and logging.

Information from the detectors of E665 is for the most part read out using CAMAC electronics. There are 6 branches of electronics which are fed(in pairs) into the 3 PDP11/34 computers which collect and store the readout data for a single event in 3 milliseconds. These PDP11/34 "front-end" computers are attached to a μVAX which reads the buffered information for each event,

E665 Streamer Chamber Film Distribution

Film	Fermilab	Krakow	Munich	Undistributed	Total
$500GeV H_2$	1,551	703	2,235	191	4,680
$500GeV D_2$	3,419	2,510	6,586	259	12,774
$500GeV Xe$	1,289	1,729	1,653	0	4,671
$100GeV D_2$	0	0	0	0	0
$100GeV Xe$	0	0	0	0	0

Table 5. Scanlist streamer chamber statistics.

concatenates it and writes it to 6250bpi tape. Attached to theμVAX as well is the calorimeter FASTBUS data acquisition system. FASTBUS serves both as a fourth front-end computer and as a readout device. So much CAL detector information must be collected and stored that the standard CAMAC path would have been prohibitively slow had it been used.

The total DAQ system can acquire and log data at an average rate of 250 kilobytes per second. A typical event is 10 kilobytes so that this rate corresponds to 25 events per second. It should be noted that the systems log data asynchronously to minimize deadtime during the 20 seconds of continuous muon beam "spill" present each minute[41]. Thus, data logging goes slower during the spill and faster otherwise. Using this method, the $\approx$ 20 percent deadtime arises predominately from only the 3 millisecond readout time.

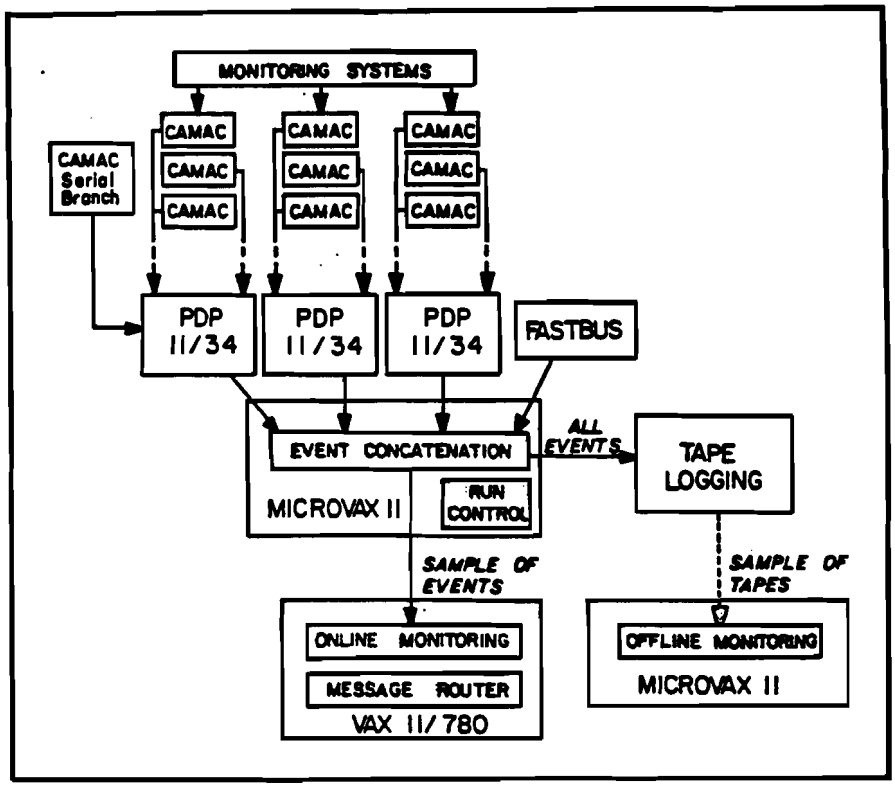

Figure 22. E665 data acquisition system.

The μVAX also sends a sample of complete events to a VAX 11-780 computer for independent analysis and detector monitoring.

Chapter 7 Event Reconstruction

The efficient processing of the 1987 E665 data has taken a great deal of planning since only 5 to 10 percent of the data has been estimated to be true DIS. The full event reconstruction processing of the non-DIS data would have been wasteful of both human and CPU time. Thus, an additional step, the LAT and SAT event filters were created to throw out non-DIS events while leaving as many DIS events as possible. These event filters throw out multiple beam, false trigger and electromagnetic events while discarding less than 1/2 percent DIS events. The filter reduces the original event sample by a factor of 3 for the LAT and a factor of 2 for the SAT.

After the filter procedure was performed on the data, full event reconstruction began. Full event reconstruction for the electronic data consists of first verifying the existence of a single in-time beam muon. Then, the beam muon, the scattered muon, and all other charged tracks in the event are identified. Kinematic fits to the hits associated with each track are performed and then the tracks are extrapolated back to the interaction point or vertex from which kinematics for the event is extracted.

Full reconstruction of the the streamer chamber picture data proceeds as follows. People known as film "scanners" in their work sit at a measuring table onto which an optical system projects an image of each film frame. The scanners record the coordinates of many points on each track to a computer database using an interactive program. Since there are 3 cameras, the scanners must go through this process for the film from each view and then match the corresponding tracks. Track kinematics are determined by a streamer chamber track reconstruction program. A comparison between measurements done at the two institutions contributing data to this analysis is given in table 6.

Streamer Chamber Measurement Data

Quantity	Fermilab H_2	Munich H_2	Fermilab D_2	Munich D_2
Event total	1406	1337	2877	2641
Avg. Measured Multiplicity	9.43 ± .14	9.47 ± .13	10.3 ± .11	10.4 ± .11
Number of Tracks	13,335	12,480	30,055	26,756
Number of Points Used	33.3±.06	53.4±.07	34.5±.04	53.0±.05
Trackfit Probability	.749±.003	.762±.003	.703±.002	.730±.002
Trackfit Residual(microns)	9.88±.03	14.49±.05	10.47±.02	14.84±.03
Track Length(cm)	129.1±.4	132.4±.4	124.5±.2	130.1±.3
Momentum(GeV/c)	3.43±.03	3.43±.03	3.13±.02	3.17±.02
Error on p^{-1} (c/GeV)	.0155±.0001	.0152±.0001	.0170±.0001	.0154±.0001
$p_{transverse}$	.433±.003	.443±.003	.423±.002	.429±.002
$p_{longitudinal}$	3.42±.03	3.43±.03	3.13±.02	3.18±.02

Table 6. Streamer Chamber Measurement Data.

The final step is to combine the optical and electronic data by matching forward-going tracks to remove duplicates and then to re-fit the vertex using both streamer chamber and forward spectrometer tracks.

§7.1 Forward Spectrometer Event Reconstruction

The beam,forward and muon spectrometer electronic wire chamber data was processed through a 4 stage software package (PTMV) written by members of the E665 collaboration based on similar code from the European Muon Collaboration which did a similar experiment using a lower energy muon beam. PTMV consists of: track pattern recognition, track fitting, track matching, muon spectrometer-forward spectrometer matching and vertex finding code. The pattern recognition code associates wire chamber hits into track segments in each detector and then tries to use straightforward algorithms to associate the found segments. The track fitting program takes associated segments and fits to them a parameterization. Track momentum and charge as well as spatial coordinate and slope information is extracted from the fit. The muon matching associates orthogonal line segments reconstructed in the muon spectrometer to a particular forward spectrometer track. Finally, the vertex finding program attempts to associate the non-muon tracks in the forward spectrometer to the point of interaction in the target(if there is one) and to find the vertices of secondary interactions and decays with the leftover tracks.

The pattern recognition program[46] is divided into 4 four phases: beam reconstruction(BEAM), muon i.d. track segment reconstruction (PTM/SMS), forward spectrometer reconstruction of the " scattered muon"(MUON), and forward spectrometer reconstruction of the "hadrons"(HADRON). In BEAM, incoming beam tracks are reconstructed from the PBT wire chamber hits. A found track must then have associated hit(s) in each of the 7 SBT hodoscopes for it to be considered "in time". In the PTM/SMS phase, horizontal and vertical view muon track segments are searched for. Scattered muon track segments pointing to both target and non-target sources are searched for. The

MUON phase consists of a search for forward spectrometer tracks originating in the target with high momentum and track segment projections downstream of the absorber. These tracks are flagged as candidates for muon matching. The HADRON phase then executes a search for all other hadron tracks.

The pattern recognition generally follows an algorithm which tries to connect the track segments farthest apart using intermediate PCF hit information. The detectors with the largest plane multiplicity in the forward spectrometer on opposite sides of the CCM are the PC and DC detectors. The PC detector has a large number of planes with good efficiency close to the target while the DC detector has a large number of good efficiency planes close to the muon spectrometer. Thus, the pattern recognition looks first for track segments in these and then tries to associate them using PCF information. It should be noted that due to the CCM magnetic field, it would be difficult to create PCF track segments and work outward from PCF. In the next phase, the program tries to link the small angle detector PS track segments with PC segments using the same basic idea. After this process iterates until no more tracks can be reasonably identified, PCV track segments are attached to the already identified tracks. Specifically, this processor performs its search using the following algorithm:

a. Find DC track segments.
b. Find PC track segments.
c. Associate PC and DC track segments, using hits in the PCF's.
d. Find PSA,PSB space points.
e. Project any unassociated PC tracks through the PCF, DC and PSA/PSB searching for tracks not found in the PC-PCF-DC search. The tracks found here are expected to be small angle scattered muons, hadrons exiting the

forward spectrometer at the CCM and hadrons that go through the dead regions of the DC's.

f. Search for heretofore missed PCF chambers using leftover hits.

g. Associate PCF tracks to hits in the PC, DC and PSA chambers.

h. Find PCV track segments.

i. Find PTA space points.

j. Link the PCV track segments to PC tracks.

The trackfitting program[47] attempts to fit a cubic spline parameterization (derived from the equations of motion in a magnetic field) to the tracks identified by pattern recognition. This fit uses coordinate, slope and magnetic field information to find the best trackfit while obtaining the track momentum.

The muon spectrometer-forward spectrometer match processor attempts to match muon track segment projections from the muon spectrometer with candidate tracks from the forward spectrometer as obtained from the MUON phase of pattern recognition. A χ^2 probability including the projection line fit and multiple scattering errors is formed for all combinations within the track and projection samples and the best projection-best track combination is taken as the muon match.

The vertex processor[48] searches for the primary vertex, fits tracks to this vertex and uses the leftover tracks in a search for other (secondary) vertices. Some secondary vertices are provided by the streamer chamber geometry program(if there is SC information) ; these are not among the tracks which may be associated to the primary. The primary vertex is arrived at in 2 stages. First, a search for the approximate intersection of the beam muon track and the scattered muon track is performed. Tracks are dropped from this sample until the vertex probability is below a cut-off value. Then, a check is made on these

"fitted" tracks to see if the contribution of any particular tracks to the overall χ^2 is above a cut value. Such additional tracks are dropped. Secondary vertices are searched for with the remaining tracks in a similar fashion but with different cuts. All tracks reported as fitted are given at their points of closest approach to the vertex to which they belong.

The following vertex classifications are reported by the vertex program:

1. No beam.
2. No secondary hadrons and exactly 1 secondary positively charged muon.
3. No secondary hadrons and > 1 secondary positively charged muons.
4. No secondary hadrons and exactly 1 secondary negatively charged muon.
5. Any other vertex with beam.
6. Neutral decay consistent with $V0$ topology and with no incident charged track.
7. Charged decay (kink).
8. Neutral secondary interaction consistent with $V+$ $V-$ topology and with charged incident track.
9. Charged secondary interaction. Vertex not consistent with $V+$ $V-$ topology and with charged incident track.
10. Types 1,2,3,5 listed above using only μ,μ' tracks in vertex fit.

§7.2 Streamer Chamber Track Reconstruction

As mentioned at the beginning of this chapter, the first step in SC track reconstruction is film measurement by scanners. The scanners "digitize" ten to twenty points on each track; digitized points are roughly 5 cm apart in real space. This must be done for all tracks which pass the scan rules. The scan rules are designed to pick out tracks which may be associated to the primary

vertex while eliminating tracks which obviously are not. The rules agreed upon for the measurement of film by the E665 collaboration are as follows[49]:

a. Measure events with $Q^2 > 1GeV^2$, $0.9 > y_{Bj} > 0.1$, and $-9.6 > x_{primary\ vertex} > -12.4m$.

b. Record the scanned track count.

c. Measure all tracks except: beam tracks, halo tracks, spiral tracks not emerging from the primary vertex and tracks not observed in 1 or more cameras.

d. Flag measured tracks which: originate upstream of the target, emerge from secondary target interactions or spiral more than a semi-circle.

In the scanner analysis, frames are assigned a scan category of from 1 to 10 according to the following scheme:

1. Satisfactory. No track problems.
2. Measured, but upstream tracks are included.
3. Measured, but partly obscured by too many tracks or flares.
4. 1 or more views missing.
5. Empty.
6. This category is not used.
7. Flares prevent measurement.
8. Faintness prevents measurement.
9. No vertex identified. Only beam,halo and upstream tracks present.
10. Multiplicity prevents measurement.

Only scan categories 1,2 and 3 are used in this analysis.

After track digitization by the scanners, the streamer chamber geometry program(SCGEOM) is used to reconstruct the tracks, determine their kinematic variables and fit the tracks to a vertex or vertices while reporting relevant errors. The scanner has decided which tracks in the 3 views are really images of the same

track. The SCGEOM program is forced to accept the scanner's determination or report an error. The track kinematic variables- coordinate,slope and momentum information, are extracted using the following:

a. Lighted, surveyed fiducial marks which appear on film whose coordinates in real space are known.

b. Survey measurement of the real space position of the 3 cameras.

The fiducial marks are used to create a planar transformation grid which can be applied to film plane measurements to account for such things as film deformation and imperfections in the optics. Using the camera position information, light ray vectors are calculated using the pinhole approximation. These vectors applied to a track's 3 views enable the calculation of the vertical or "z" coordinate with a parallax algorithm. The measured tracks are thus transformed into the ideal film plane in which a track fit reveals all kinematic information. The momentum is calculated using a circular fit.The kinematics are reported in the variables x,y,z,"dip" and "phi"(see figure 23).

After track reconstruction, a vertex processor is run which attempts to fit a primary or interaction point vertex, but whose most useful function is that of identifying secondary and decay vertices. The latter is most useful since analysis will only be done after the SC data is combined with that from the forward spectrometer(no muon information with SC alone). With the merging of data, the primary vertex information is discarded, but the secondary vertex information is kept so that this work will not have to be done twice.The method by which SC data is combined with forward spectrometer data is described next.

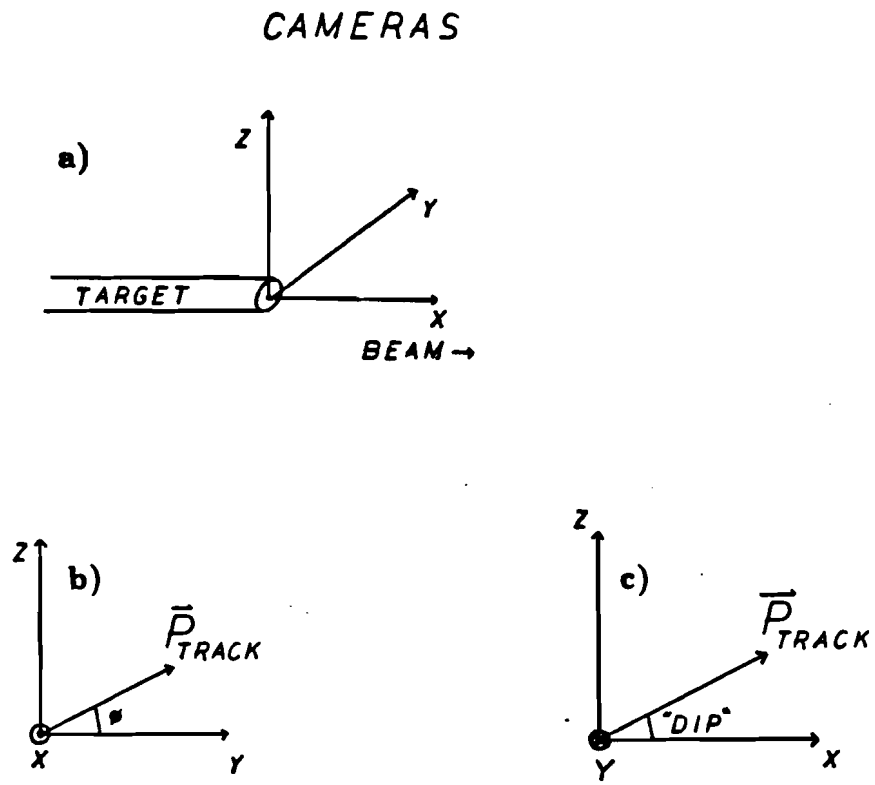

Figure 23. a)Streamer chamber local coordinate system, b)ϕ angle, c)"dip" angle.

§7.3 Combined SC-Forward Spectrometer Event Reconstruction

Under the circumstances that SC data exists for an event, it is necessary to merge this data with that from the forward spectrometer. Since the SC tracks are reported in a different coordinate system, a coordinate transformation is performed from the (x, y, z, dip, ϕ) system to the (x, y, z, y', z') system. After that, alignment translations and rotations are applied based on constants obtained from comparing forward-going tracks which appear in both systems. To remove the duplicate tracks in the forward region, the streamer chamber-forward spectrometer match processor is run on the data. When a duplicate track is found

by comparing the y, z, y', z' and $1/p$ variables for both, then the forward spectrometer values are used to represent the track since they are considered to be more reliable. Finally, the vertex processor described earlier is re-run on the combined data set. Note that using track information from a different source(SC) does not present any special problems to the vertex processor since it uses the coordinate,slope,charge and momentum information from the track alone. Although the vertex algorithm for finding the primary vertex is the same, track errors are handled in a special way. Due to optical distortion, the streamer chamber geometry reported tracking errors fed into the streamer chamber-forward spectrometer match processor and vertex processor are increased by a multiplicative factor to make them more realistic when compared to the forward spectrometer tracks in the combined fits done in these processors. Thus, apart from the "head start" on secondary vertices and the track error scaling, the vertex fit is done in the same fashion as the forward spectrometer vertex fit with the same vertex information reported. This error scaling factor is 1.5 for tracks originating downstream of the target and 6 otherwise.

§7.4 SC-Forward Spectrometer Alignment Constants

As mentioned, the alignment of the streamer chamber is somewhat involved since it is an optical device and thus subject to spatially dependent track distortion. Initial alignment comes from the fiducial survey marks which appear in each picture. Simple interpolation between the marks is insufficient to determine the spatial location of all measured track points since few of the tracks are in the same plane as the fiducial marks. Even within the same plane, there is non-linear optical distortion of the tracks. To remedy this situation, a distortion correction grid was created which applies spatial offsets to measured trackpoints

based on their location in the streamer chamber. These constants are obtained by comparing forward spectrometer halo tracks with corresponding tracks in the streamer chamber. For tracks which are too low in momentum to have a corresponding forward spectrometer track, constants are extracted which will cause these wide angle tracks to have a constant curvature. Since one can best extract constants for the beam region, this region is taken as a reference. The distortion constants consist of a 101 x 51 grid in the horizontal plane and are applied before SCGEOM track reconstruction. Note that there are more divisions in the x direction.

Due to limitations in the quality of these constants- particularly reflected in the vertical coordinate, additional alignment is necessary before one matches streamer chamber tracks with forward spectrometer tracks and then vertex fits the entire track sample. These constants are translations and rotations within the (x, y, z, y', z') coordinate system. It has been shown that the optical distortion is worst farthest from the center. This distortion results in the vertical coordinate z being systematically downwardly shifted as one moves away from the center. Thus, a simple rotation about the y axis to align beam region streamer chamber and forward spectrometer tracks will not correct the problem since such a rotation would worsen the situation for wide angle tracks. Thus, one applies different z and z' constants for forward going and wide angle tracks. The constants applied before matching are specifically:

$$y_{SC} = y_{SC} - .0025m$$

$$\theta_z = \theta_z - .004 milliradians \ (rotation\ about\ the\ vertical\ axis)$$

$$z_{SC} = z_{SC} - .015m \ for\ tracks\ originating\ downstream\ of\ the\ target$$

$$z_{SC} = z_{SC} - .003m \ otherwise$$

$$z'_{SC} = z'_{SC} + .023 milliradians \ for \ tracks \ originating \ downstream \ of \ the \ target$$

$$z'_{SC} = z'_{SC} + .016 milliradians \ otherwise$$

Note that a single y translation and a rotation about the z-axis may be used for all tracks since the distortion in the $x - y$ plane is small and these adjustments may well be spatial- not merely optical. As for z and z', systematic scalar adjustments are made for the reasons described.

Chapter 8 Analysis

The focus of the analysis is the measurement of charged hadron multiplicity distributions for hydrogen and deuterium targets. The goal of this endeavor is to report correctly the number of charged hadron tracks originating from the original DIS as a function of W and Q^2. To do this, one must count the tracks in a systematic way and then correct for losses and gains.

There are a number of sources of track losses and gains. The tool for correcting the measurements to take into account the losses and gains is the Monte Carlo.

The major sources of track loss follow with those things pertaining to the streamer chamber denoted by SC and those pertaining to the forward spectrometer denoted by FS:

a. Charged pion decay(SC,FS).

b. Re-interactions where none of the decay products fit well to the muon vertex(SC,FS).

c. Obfuscation of tracks due to track density problems. Due to the $1\mu s$ SC livetime, 5-10 non-interacting beam tracks appear downstream of the target on film in each event making track separation more difficult(SC).

d. Tracks with vertical slope of great magnitude. Both detector systems have limitations here. The streamer chamber has a shadow below the target while tracks into the cameras appear very short(unusable) on film. The forward spectrometer has magnet pole pieces which tracks may run into.(SC,FS)

The major sources of track gains follow.

e. K^0,Λ^0 and Dalitz decays(SC,FS).

f. Measured knock-on electrons(violates scan rules)(SC).

g. Pre-target interaction hadrons and leptons(SC).

h. Mistakenly measured non-interacting muons(SC).

i. Forward spectrometer ghost tracks(tracks created from electronic hits associated with different tracks or noise)(FS).

j. Re-interactions where more than one of the decay products fits well to the muon vertex(SC,FS).

In addition, the DIS data may be contaminated by electromagnetic events. The major types of possible contaminants are muon bremsstrahlung and muon electron scattering. It is desirable to remove radiative DIS events as well since they distort Q^2 and ν. The tools for eliminating these events from the data are kinematics cuts and electromagnetic calorimeter cuts. The kinematic cuts come into play because the quasi-elastic events dominate in fairly well-defined kinematic regions. These regions for E665 are $x_{Bj} < .003$ and $y_{Bj} > .9$. The calorimeter is useful in removing the the remaining contamination because electrons and photons produced in electromagnetic events should deposit a large amount of energy in this detector. From test beam measurements and measurements in the experiment itself, it has been shown that hadrons typically leave at most 10-15 % of their energy in the E665 calorimeter.

More difficult considerations are those of bias in the data set. If the physics trigger or detector causes the data set to be biased within the event kinematic cuts or ignores certain physics signatures altogether, then the physics results will be accordingly skewed. Software may systematically err in the reconstruction of certain kinds of events creating bias as well. It is necessary to properly address these bias problems as well.

After cuts on the data, the tool for correcting bias problems as well as acceptance problems is the Monte Carlo event simulation program. This program

simulates the experimental apparatus as well as the physics one expects from models or previous experiments. The legitimacy of the E665 Monte Carlo will be established by comparison with the data and by the details of what it does.

In this chapter, the event selection, the trigger bias, the uncorrected multiplicity extraction and the Monte Carlo correction work done to arrive at a physics result will be discussed.

§8.1 Event Selection

In this section, a comparison of the muon kinematics from data will be made with that from Monte Carlo to show that the Monte Carlo qualitatively reproduces distributions from data.

The fully reconstructed E665 streamer chamber data consists of 1213 H_2 and 2660 D_2 LAT·PCNZ events within these prescribed bounds:

$$Q^2 > 4GeV^2$$

$$W^2 > 90GeV^2$$

$$.9 > y_{Bj} > .1$$

The Q^2 cut removes the small angle region of the LAT trigger where the acceptance is falling. The W^2 removes events most affected by forward spectrometer software inefficiency. The y_{Bj} cut removes quasi-elastic events with its upper cut and the lower cut overlaps with the Q^2 and W^2 cuts but is listed for completeness.

The reader is reminded that the PCNZ trigger requires only that there be hit(s) in two of the horizontally wired forward spectrometer PC planes outside a 19.2 cm horizontal band. The trigger bias will be discussed in detail in section 8.3.

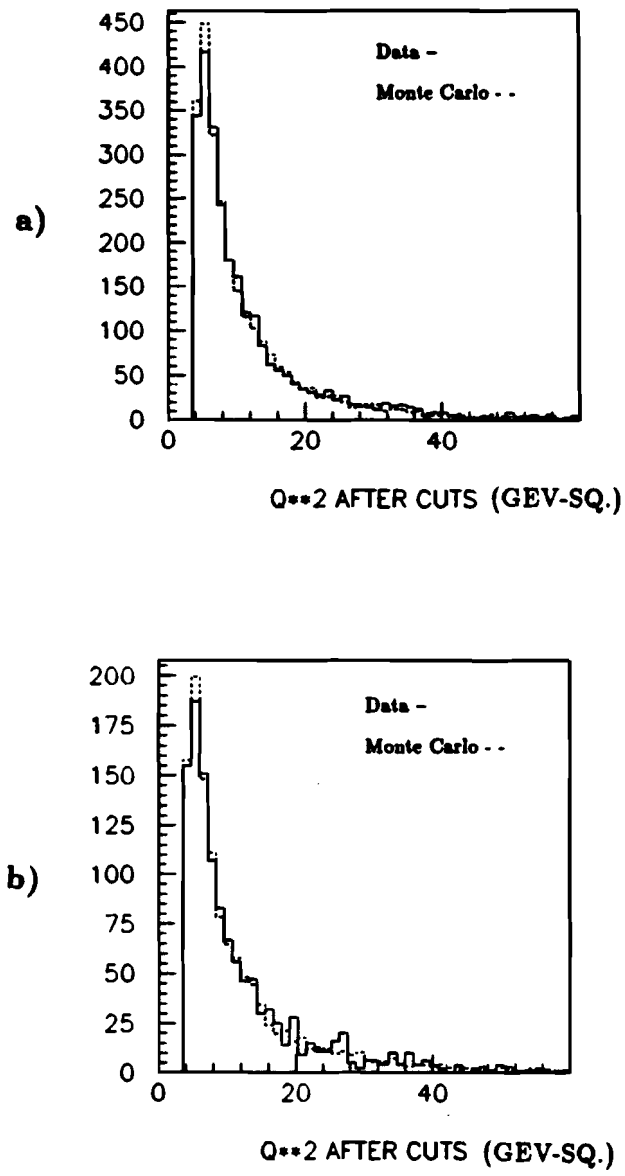

Figure 24. Q^2 distributions for a)D_2 data and Monte Carlo, b)H_2 data and Monte Carlo.

To begin our comparison of data and Monte Carlo, the Q^2 distributions for these targets are shown in figure 24.

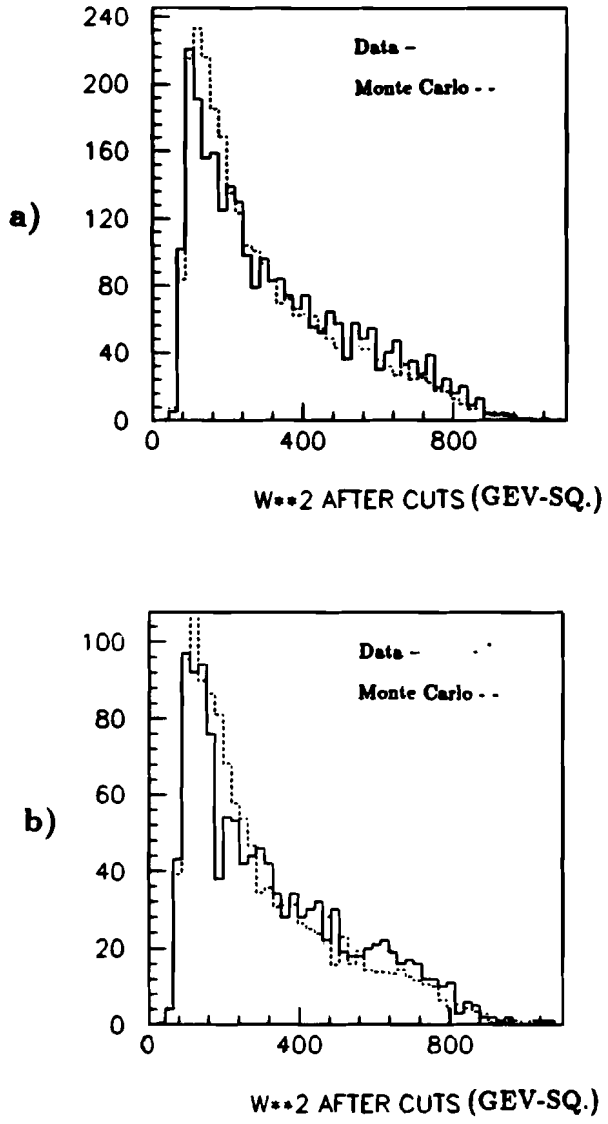

Figure 25. W^2 distributions for a)D_2 data and Monte Carlo, b)H_2 data and Monte Carlo.

From the distribution of events, it is clear that most of the events fall in the range $4 < Q^2 < 10GeV^2$ although reasonable statistics for $10 < Q^2 < 25GeV^2$ are also present. The Q^{-4} dependence of the cross section is responsible for the distribution of events in Q^2.

Another comparison of data to Monte Carlo is found in the W^2 distribution of figure 25. E665 has useful statistics up to a W^2 of 780 GeV^2. It should be noted that no previous deep inelastic lepton-hadron experiment has published with data whose W^2 is greater than 400 GeV^2. As well, the magnitude of the incoming muon's energy carries E665 lower in x_{Bj} than previous experiments in its class. In particular, the SAT·PCNZ data from E665 goes down to x_{Bj} of .003. When measured, this data can in principle reach even lower if current electromagnetic background problems become better understood. Figure 26 shows y_{Bj} to have larger statistics at smaller values of that variable.

§8.2 Electromagnetic Event Cuts

It should be noted that along with standard kinematic cuts, additional cuts are necessary to eliminate muon bremsstrahlung and muon-electron scattering. This background is characterized by a large electromagnetic shower in the calorimeter with an energy deposition which is a large fraction of the muon energy loss ν. Thus, cuts are made using our best tool for identifying the presence of this background: the E665 electromagnetic calorimeter. The cuts are imposed using E_{tot}, the total energy deposited in the calorimeter pad towers, ν, the virtual photon energy, and N_{clus}, the number of energy clusters in the calorimeter with energy greater than 2 GeV. Events are dropped from the final data set if any of the following are true:

$$\frac{E_{tot}}{\nu} > .6 \text{ and } N_{clus} < 3$$

$$\frac{E_{tot}}{\nu} > .8$$

$$E_{tot} > 230\ GeV \text{ and } N_{clus} < 3$$

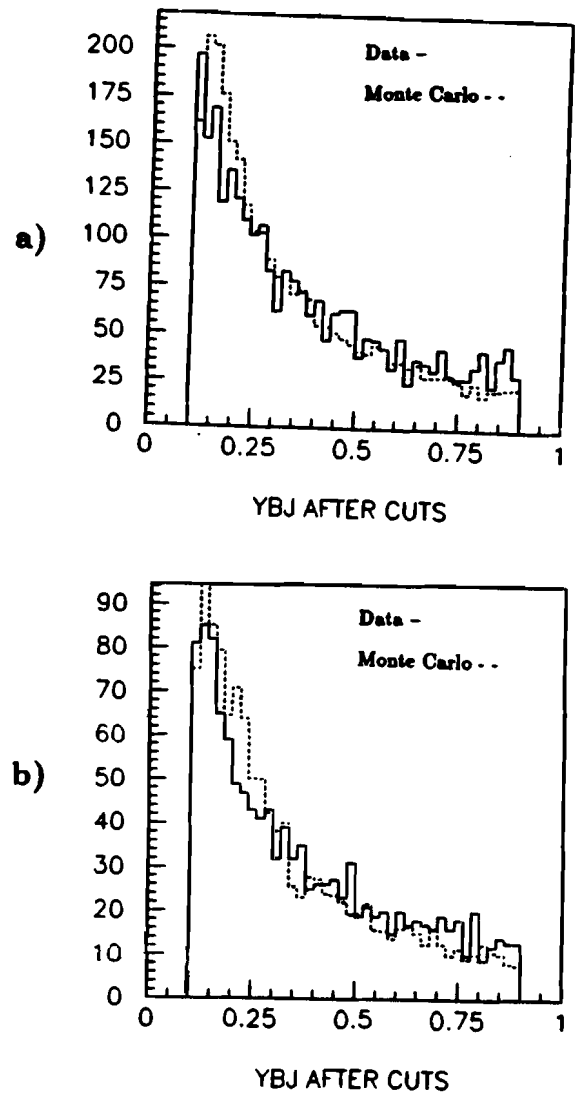

Figure 26. Data and Monte Carlo y_{Bj} distributions for a) D_2 and b) H_2.

The first cut eliminates the event if 60 % of the energy lost by the beam muon in scattering is deposited in the calorimeter and if there are only one or two clusters. These constraints indicate that the cluster(s) is the shower from a photon or electron and the event is probably radiative. The second cut eliminates the event if 80% of ν is deposited in the calorimeter. The assumption

here is that the energy must have originally gone predominately to a photon or electron which showered once again indicating a radiative event. The last cut eliminates the event if a large amount of energy went into one or two calorimeter clusters indicating a radiative event.

After these cuts, the N=0 bin was cut since any remaining muon bremsstrahlung contamination would have zero multiplicity as would any streamer chamber-forward spectrometer event mismatches or unfiltered false LAT triggers(see chapter 7). The fraction of triggers removed by the calorimeter cuts and the bin cut is 3.5 %. The fraction of DIS events removed by these cuts is estimated to be less than 1 % yielding minimal bias. Some of the radiative DIS events are likely to be removed by the calorimeter cuts. Since the muon kinematics distributions have been shown to be reasonable, radiative DIS events are thought to have little presence in the data.

§8.3 LAT·PCNZ Trigger Acceptance

The data used consists of events triggered upon by the LAT·PCNZ trigger(see section 5.9). LAT trigger acceptance is described by figure 20. For the given kinematic regions under consideration, the LAT·PCNZ trigger acceptance as determined from Monte Carlo is found in figure 21. False PCNZ triggers arising from noise will be modelled by the Monte Carlo and discussed next.

The integrity of the trigger simulation in the Monte Carlo is checked by this study in two different ways. The fraction of LAT triggers which additionally satisfy PCNZ as a function of W is shown in figure 27 for both data and Monte Carlo. Note that the data used here is filtered(see chapter 7) LAT electronic events.

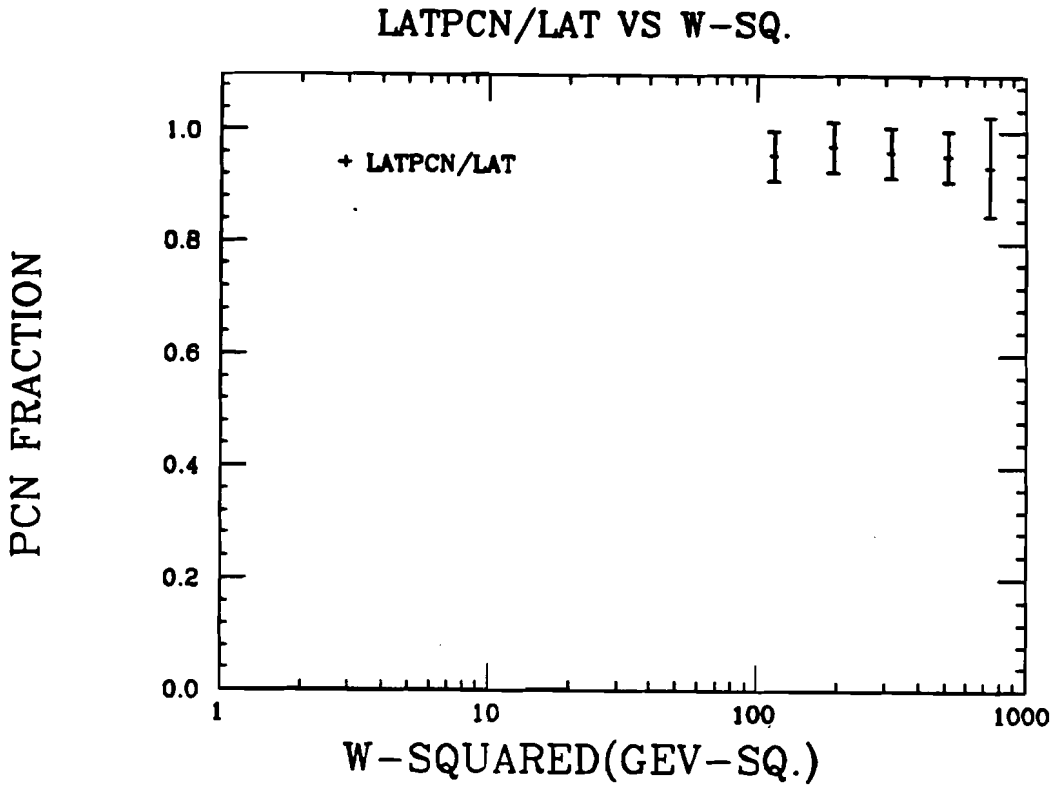

Figure 27. Ratio of LAT·PCNZ over LAT vs. W.

There is good qualitative agreement between the two. One can also examine the fraction of LAT·PCN triggers which are fired by reconstructed tracks. Data and Monte Carlo plots are shown to be in agreement to within 10 % at low W and better at high W in figure 28. In order for an event to satisfy the reconstructed

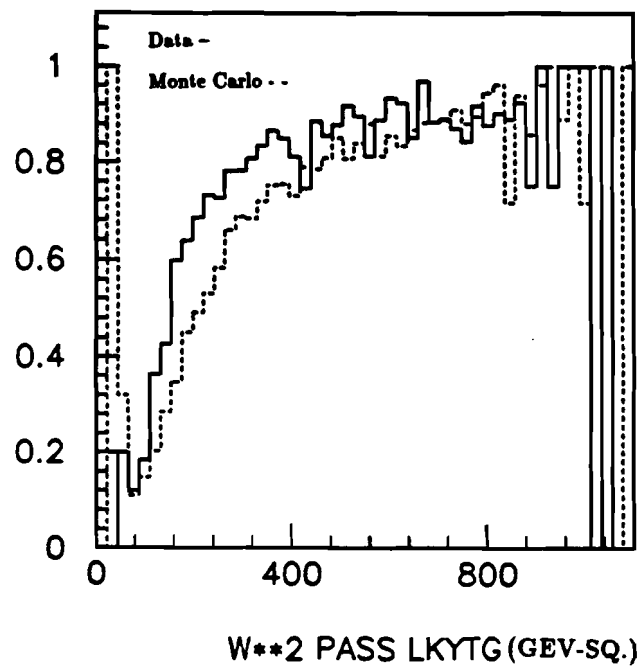

Figure 28. Fraction of LAT·PCNZ triggered by found tracks vs. W.

track PCNZ condition, there must be two or more PC planes hit at least 9.6 cm away from the E665 x axis in the vertical or z coordinate and these hits must be associated with reconstructed track(s). The reader is reminded that the x axis is roughly parallel to the incoming beam. The fact that reconstructed tracks do

not trigger at low W is a result of our track reconstruction inefficiency and not due to a large random trigger background.

§8.4 Uncorrected Multiplicity

The raw data for the multiplicities are the reconstructed tracks which are then fitted to a vertex. The tracks which are the input for the vertex fitting processor follow: all streamer chamber detector tracks, beam region forward spectrometer tracks which go unmatched by the streamer chamber-forward spectrometer match processor, and all matched beam region tracks. The term "beam region" here is defined to be a 10 cm box centered on the x-axis.

As described before, the vertex fitting program attempts to associate subsets of tracks to the primary and any secondary vertices. The number of fitted tracks(excluding muons) yields an uncorrected charged hadron multiplicity.

§8.5 Monte Carlo Corrections

The production of Monte Carlo events is a very detailed undertaking and can adversely affect the physics results if improperly done. A description of the major parts of the Monte Carlo used by E665 follows. The Geant portion of the Monte Carlo allows one to construct in software, a very detailed geometry using a variety of materials. The Lund generator permits the user to select his favorite structure functions for event generation. As well, E665 has made provisions for the imposition of noise hits and the smearing of input track hits. The details follow.

The Monte Carlo for E665 makes use of the Lund 4.3[27] generator with Morfin and Tung structure functions. Geant[50] tracking and detector geometry simulation are included with the Geisha physics process routines as part of the Geant

package. The E665 organization of the Monte Carlo divides it into two sections. Stage one controls the Lund and Geant input parameters, kinematic cuts, particle tracking, detector geometry creation, material specification and recording of generated particle kinematical quantities. Stage two introduces detector noise and plane hit smearing. Listed are the generation parameters selected for E665 hydrogen and deuterium Monte Carlo production using Lund with Jetset 4.3 and Morfin and Tung structure functions. The Geisha physics processes activated are:

a. Gaussian multiple scattering.

b. Particle decays.

c. Compton scattering.

d. Pair production.

e. $e-$ bremsstrahlung .

f. Delta rays.

g. $e+$ annihilation.

h. Hadronic interactions.

The kinematic cuts were:

i. $Q^2 > 3.5 GeV^2$

j. $\nu > 40 GeV$

k. $.1 < y_{Bj} < .9$

Additionally, tracks were treated as follows:

l. Tracking in forward spectrometer if track $p > .5 GeV$

m. Tracking in streamer chamber if track $p > .2 GeV$

n. Electronic noise added.

o. Electronic track hits smeared.

p. SC tracks smeared.

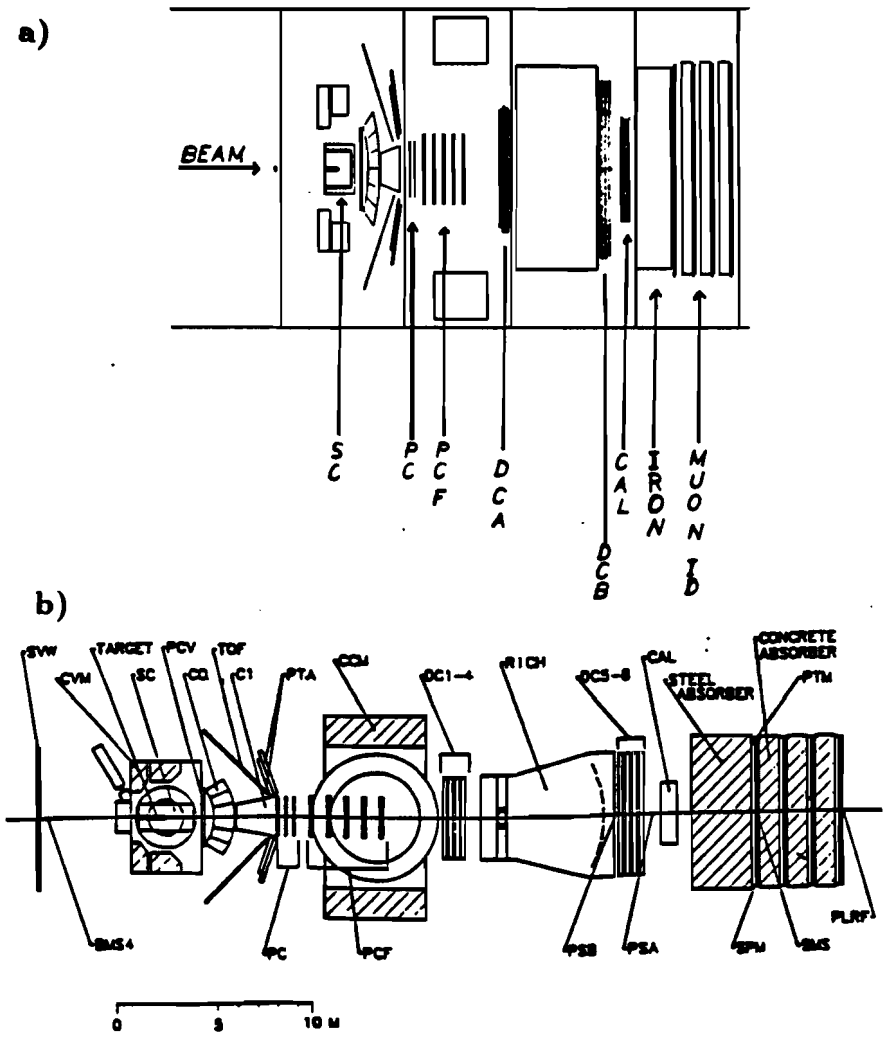

Figure 29. a)Monte Carlo geometry simulation, b) Engineering drawing of apparatus.

Figure 29 indicates the qualitative detail with which the geometry was simulated in Geant.

Figure 30, which is a comparison of real and Monte Carlo data, demonstrates the quality with which wire chamber plane hit multiplicity is simulated.

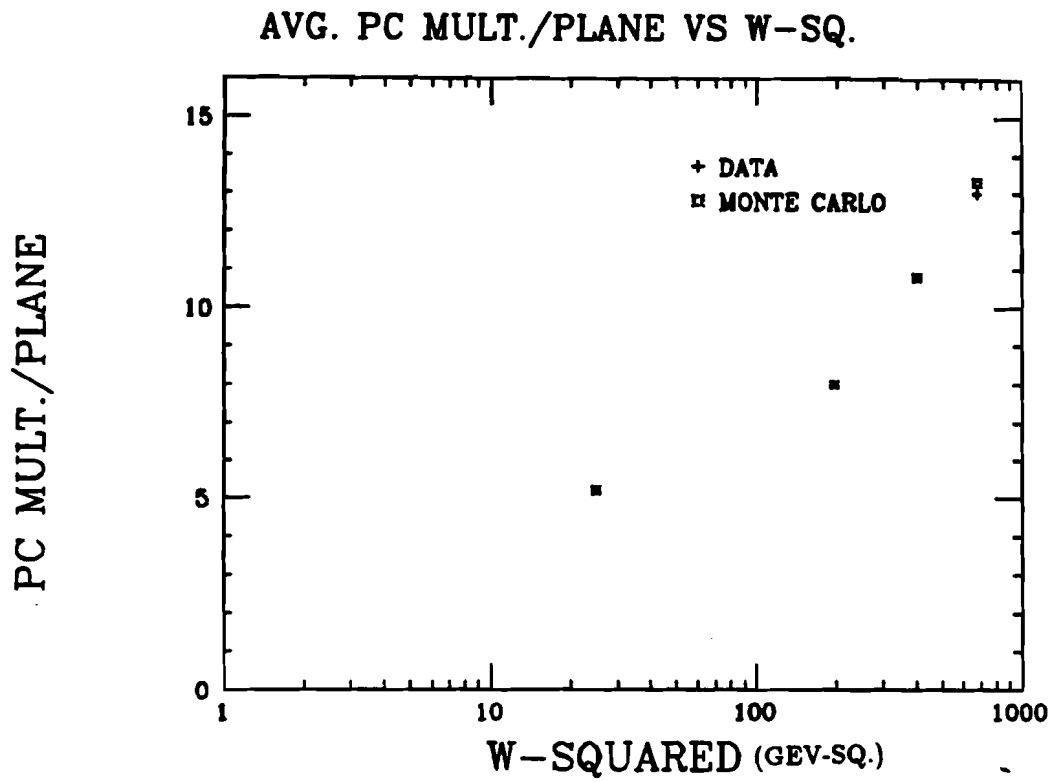

Figure 30. Monte Carlo vs. data PCN plane hit multiplicity(noise hits included).[51]

By running simulated data through the PTMV software and applying correction factors in a way which will be described below, software, detector and trigger bias is compensated for.

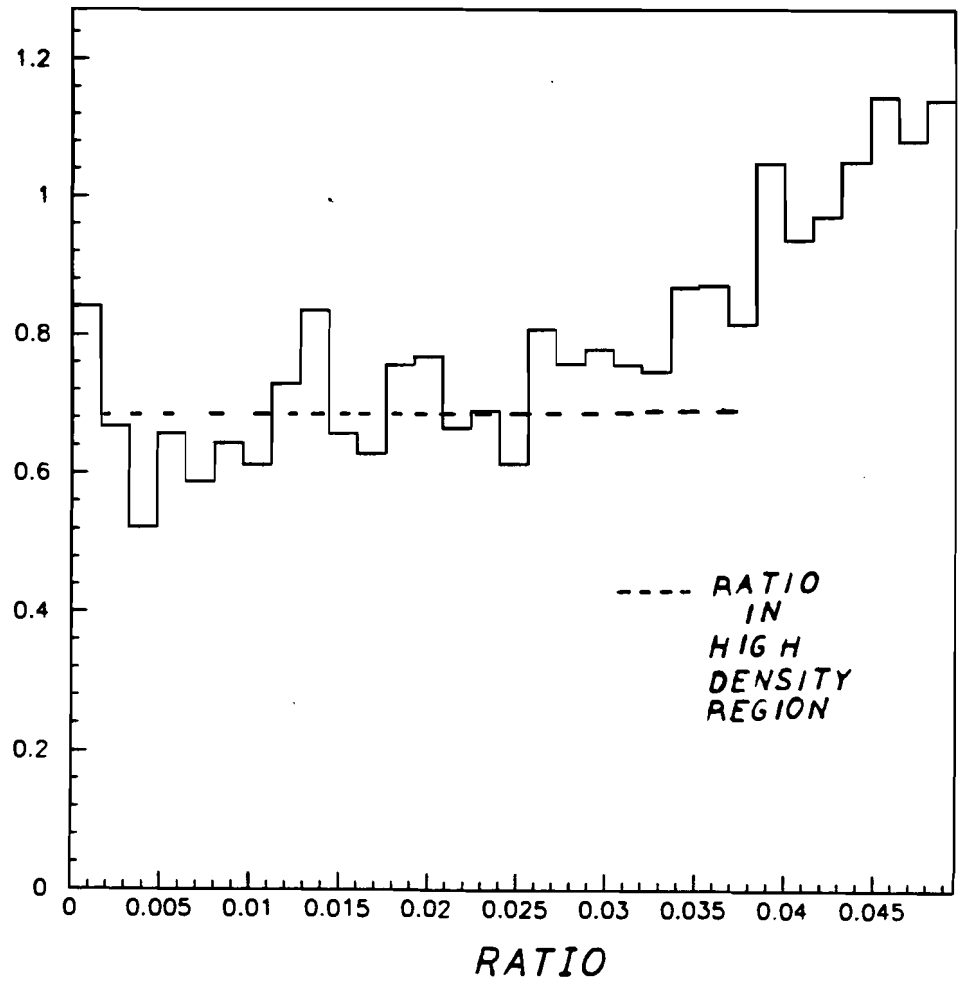

Figure 31. Ratio of the number of streamer chamber tracks to that of the forward spectrometer as a function of track Y_{max} in the beam region.

The streamer chamber Monte Carlo is a crucial part of the analysis described in this thesis. This Monte Carlo consists of collecting streamer chamber track information in banks at the Geant tracking stage and smearing these tracks just before the streamer chamber- forward spectrometer track match. In real

data, streamer chamber track kinematic variables are reported at the first visible track point outside the target. In the streamer chamber Monte Carlo, streamer chamber track information is given accordingly. During the tracking phase of the Monte Carlo, the output event information is not stored until Geant tracking places the particle in question outside the target within the visibility of all three streamer chamber cameras.

As well, due to beam region track density acceptance losses, one does not expect beam region acceptance from data to be as good as Monte Carlo. Based on comparisons between real data forward spectrometer tracks and streamer chamber tracks in the beam region(figure 31), 33 % of the streamer chamber tracks in the beam region are randomly dropped in Monte Carlo "events" after processing them through PTMV to simulate this real data track loss. To further improve this, an additional $100(1-10/\sqrt{p})$ % of the tracks left with $p > 10GeV$ are dropped. It should be noted that the simulation of the beam region is useful to check the matching which was used in streamer chamber-forward spectrometer alignment, but is not critical to the multiplicity since unmatched beam region streamer chamber tracks are dropped from the multiplicity measurement(see section 8.8). Evidence that the number of tracks dropped is reasonable in terms of y' and momentum is presented in figure 32.

From data, the errors on each of the track kinematic quantities used to match and fit a primary vertex are known. These values after multiplication by an optical distortion factor are used to smear the Monte Carlo streamer chamber tracks. Although the optical distortion is important, a Monte Carlo study reveals that only 3.5% of input streamer chamber primaries are lost by the vertex fit due to smearing.

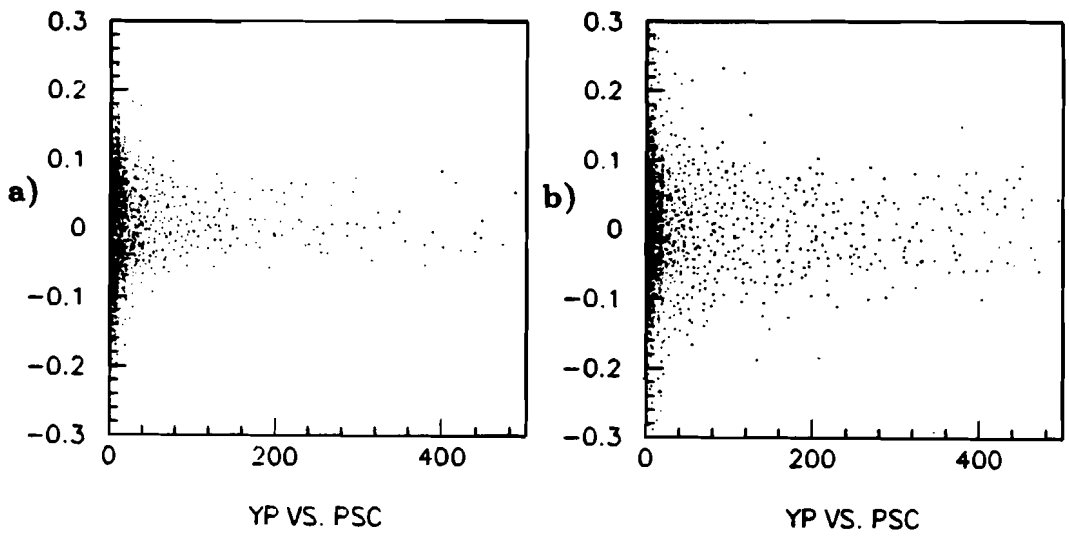

Figure 32. y' vs momentum in D_2 a) data and b), Monte Carlo

At this point, we move to a discussion of how the Monte Carlo will be used in data analysis. The Monte Carlo data is used to correct measured multiplicity for all of the effects discussed at the beginning of the chapter- track acceptance, trigger acceptance, software inefficiency and contamination of the multiplicity by tracks arising from secondary interactions and decays. To accomplish this,

a correction grid is created for each bin of Q^2 and W^2 present with sufficient statistics in the data. The simulated electronic data is processed through pattern recognition and trackfitting in the same way as real electronic data. It is then matched with streamer chamber data and the combined track set is fit to a vertex. Kinematics are calculated and cuts are applied. For each bin, the correction factor:

$$C = \frac{N_{\text{Unprocessed Lund Generation}}}{N_{\text{analysed}}}$$

is calculated. The statistical errors from both Monte Carlo paths as well as from the data itself are propagated to arrive at a corrected measurement error. The correction factors arising from this method are given in tables 7 and 8.

The only effects which cannot be corrected for are wide angle upstream interaction tracks and mistakenly measured knock-on electron tracks. Either of these is a problem only when the track is attached by the vertex processor to the muon vertex. The upstream interaction correction is a constant independent of kinematics. It is systematically checked by varying the looseness of vertex track fit cuts (see section 9.3). The assumption is that the looser the cut, the wider the "window" for accepting upstream interaction tracks. Sometimes electron tracks are mistakenly measured and then attached to the vertex by the vertex processor. Both of these effects have a negligible effect estimated to be less than 1 % by re-scanning.

§8.6 Monte Carlo vs. Data Comparisons

Comparisons between the Monte Carlo and the data are given in this section. Since acceptance, hadron decay and re-interaction corrections are made using the Monte Carlo, it is important that known hadronization processes as well as

a) Multiplicity Correction Factors(Clcut=1cm)

Target	$ln(Q^2)$	$W^2(GeV-sq.)$	C_{factor}	σ
H_2	All	115.6	1.17	.09
H_2	All	190.6	1.20	.12
H_2	All	314.2	1.17	.11
H_2	All	513.0	1.17	.14
D_2	All	115.6	1.18	.07
D_2	All	190.6	1.18	.08
D_2	All	314.2	1.13	.09
D_2	All	513.0	1.13	.11
D_2	All	735.0	1.16	.14
H_2	1.83	115.6	1.16	.13
H_2	2.87	115.6	1.19	.18
H_2	1.68	244.7	1.18	.15
H_2	2.31	244.7	1.17	.15
H_2	3.21	244.7	1.18	.18
H_2	1.68	561.2	1.18	.2
H_2	2.31	561.2	1.17	.23
H_2	3.21	561.2	1.19	.27
D_2	1.83	115.6	1.18	.10
D_2	2.87	115.6	1.15	.09
D_2	1.68	244.7	1.15	.09
D_2	2.31	244.7	1.13	.11
D_2	3.21	244.7	1.16	.12
D_2	1.68	561.2	1.13	.13
D_2	2.31	561.2	1.14	.14
D_2	3.21	561.2	1.16	.15

b) Multiplicity Correction Factors vs. z_{vertex}

Target	$ln(Q^2)$	$W^2(GeV-sq.)$	$z_{vertex}(m)$	C_{factor}	σ
H_2	All	148.4	-11.63	1.09	.16
H_2	All	148.4	-11.37	1.15	.16
H_2	All	148.4	-11.12	1.15	.17
H_2	All	148.4	-10.75	1.26	.13
H_2	All	403.4	-11.63	1.08	.18
H_2	All	403.4	-11.37	1.08	.18
H_2	All	403.4	-11.12	1.135	.19
H_2	All	403.4	-10.75	1.28	.15
D_2	All	148.4	-11.63	1.08	.12
D_2	All	148.4	-11.37	1.13	.12
D_2	All	148.4	-11.12	1.16	.13
D_2	All	148.4	-10.88	1.22	.14
D_2	All	148.4	-10.63	1.28	.14
D_2	All	403.4	-11.63	1.05	.15
D_2	All	403.4	-11.37	1.07	.15
D_2	All	403.4	-11.12	1.1	.15
D_2	All	403.4	-10.88	1.17	.16
D_2	All	403.4	-10.63	1.26	.17
D_2	All	735.0	-11.38	1.09	.18
D_2	All	735.0	-10.75	1.24	.18

c) Multiplicity Correction Factors vs. x_F

Target	$W^2(GeV-sq.)$	x_F range	C_{factor}	σ
D_2	115.6	Positive	1.44	.07
D_2	190.6	Positive	1.51	.07
D_2	314.2	Positive	1.51	.07
D_2	513.0	Positive	1.57	.08
D_2	115.6	Negative	0.98	.04
D_2	190.6	Negative	0.96	.05
D_2	314.2	Negative	0.87	.05
D_2	513.0	Negative	0.84	.07

Table 7. Multiplicity correction factors as a function of a)W^2 and Q^2, b) z_{vertex}, c) x_F for a close track inclusion cut of $1cm$.

the apparatus be simulated well in the Monte Carlo. Evidence that this is the case follows.

Multiplicity Correction Factors(Clcut=5cm)

Target	$W^2(GeV-sq.)$	C_{factor}	σ
H_2	115.6	1.05	.105
H_2	190.6	1.06	.11
H_2	314.2	1.07	.11
H_2	513.0	1.06	.13
D_2	115.6	1.05	.07
D_2	190.6	1.04	.08
D_2	314.2	1.00	.09
D_2	513.0	0.99	.09
D_2	735.0	1.005	.15

Table 8. Multiplicity correction factors as a function of W^2.

§8.6.1 Vertex Fit Residuals

The vertex residual is defined to be the difference between the track coordinate at the point of closest approach and the vertex coordinate. The y and z track residuals are shown in figure 33. From data one can see that the physical alignment of the two track measurement systems, the streamer chamber optical

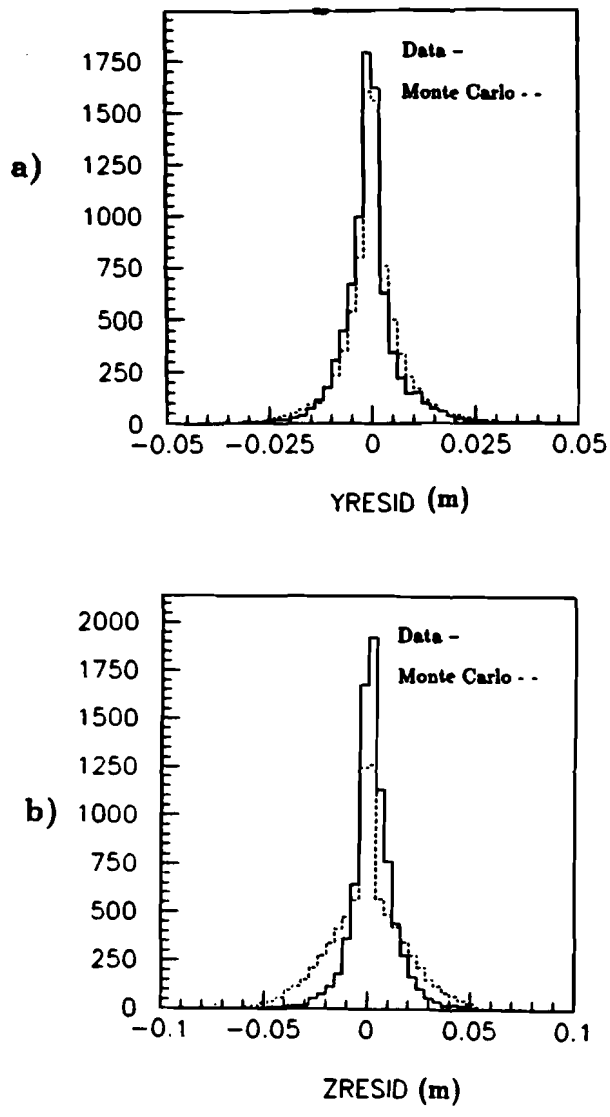

Figure 33. For D_2 data a) y_{vertex}-y_{track}, b) z_{vertex}-z_{track}. Note that the track variables are given at the point of closest approach to the vertex.

distortion and the track momentum resolution combine to form residuals of .5 cm half-width. Monte Carlo and data are qualitatively similar.

Tracks are fit to the vertex on the basis of minimum distance to vertex over track error. This quantity for tracks fitted to the muon vertex is given in figure 34a(minimum distance without error scaling in 34c). For tracks omitted from the muon and any secondary vertex fit, see figure 35. The agreement between Monte Carlo and data after error scaling gives one confidence that the vertex processor fits tracks to the vertex in an equivalent way. The reader is reminded that this scaling is necessary due to the presence of optical distortions which vary with track location in the streamer chamber. Figure 34c confirms this.

§8.6.2 Track Momentum and Angle Distributions

It is also necessary to examine the basic kinematics of tracks which fit to the vertex in checking the quality of the Monte Carlo.

The reciprocal track momentum is given for Monte Carlo and data in figure 36. Figure 37 is the sum of the transverse lab frame momentum (with respect to the incident muon direction). Figure 38 is the ϕ distribution(angle about the beam axis).

§8.6.3 SC-FS Track Match Residuals

To do alignment, forward spectrometer and streamer chamber tracks were matched by kinematics. Track match residuals for y, y', z, and z' are shown in figure 39 .

All beam region streamer chamber-forward spectrometer track combinations are taken in these plots. The match peaks are clearly above the combinatoric background and the similarity between data and Monte Carlo is evident. Evident as well is the quality of alignment between the streamer chamber and the forward spectrometer.

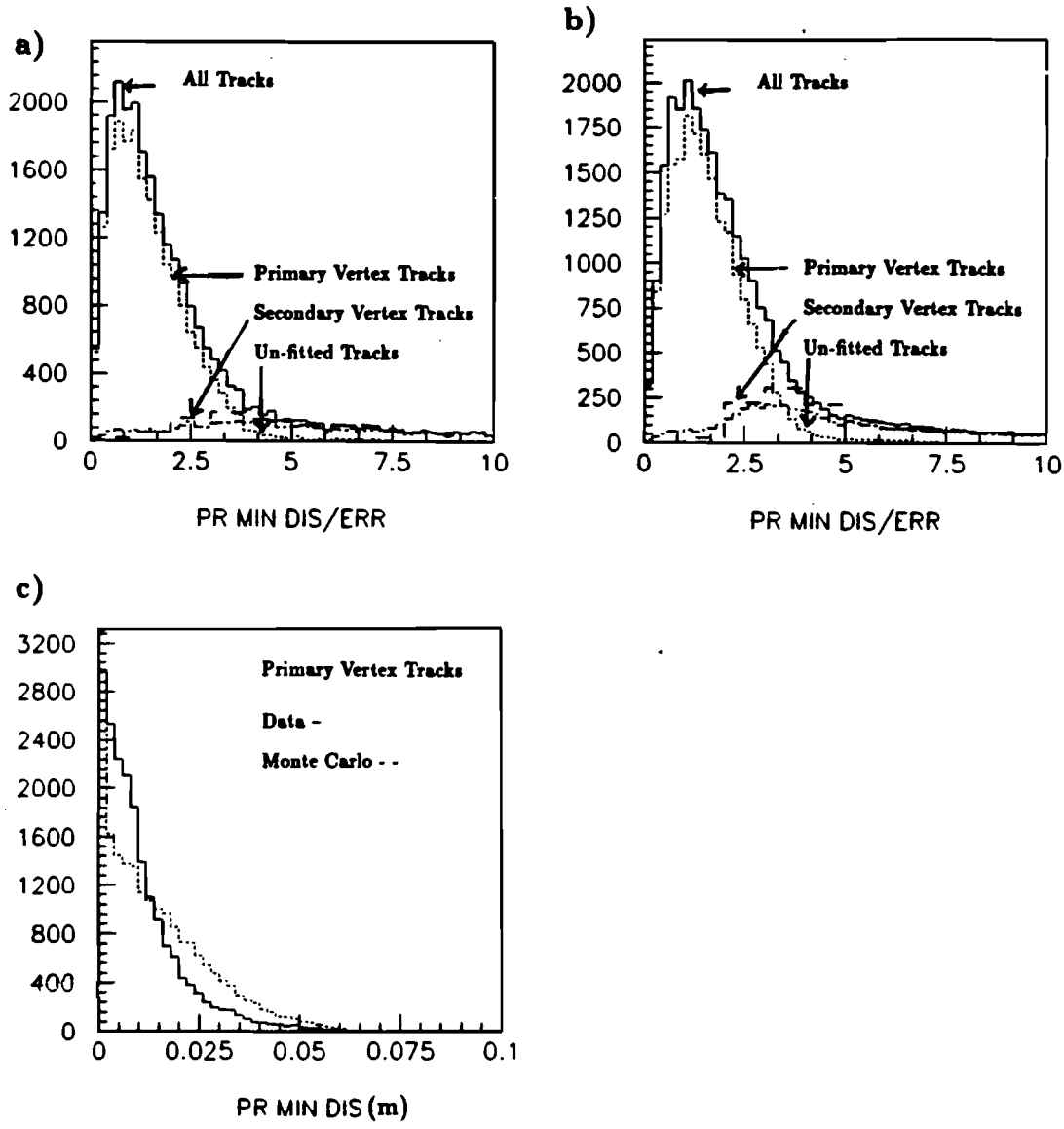

Figure 34. D_2 vertex fitted track *minimum distance/error* for a) data b) Monte Carlo, c) *minimum distance* in meters.

The beam region track match compares the reciprocal momentum $1/p$ as well. The forward spectrometer momentum p_{FS} is plotted against the difference of forward spectrometer $1/p$ with its matched streamer chamber track in figure

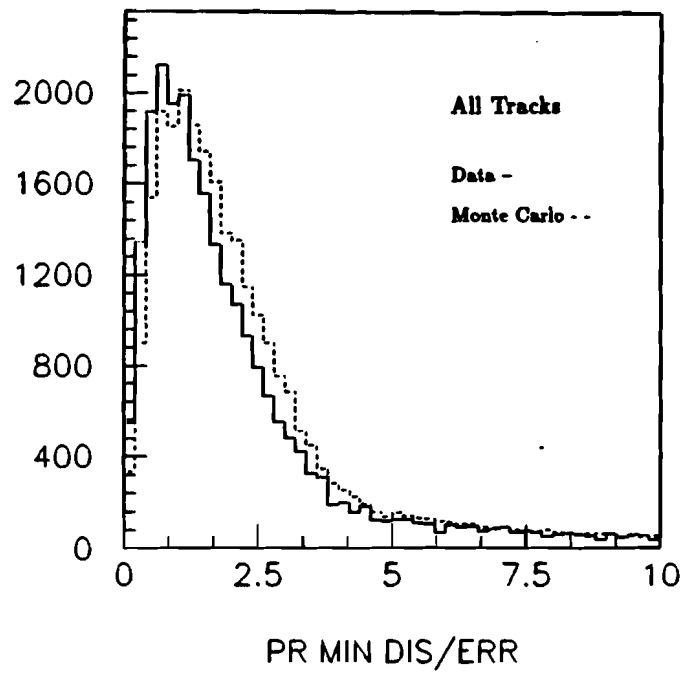

Figure 35. D_2 data and Monte Carlo track *minimum distance/error* Note that these plots are for tracks fitted to any vertex.

40 and the comparison between Monte Carlo and data is once again reasonable. The data and Monte Carlo both exhibit the p % momentum resolution of the streamer chamber(i.e. a $5GeV$ track has a 5 % momentum error).

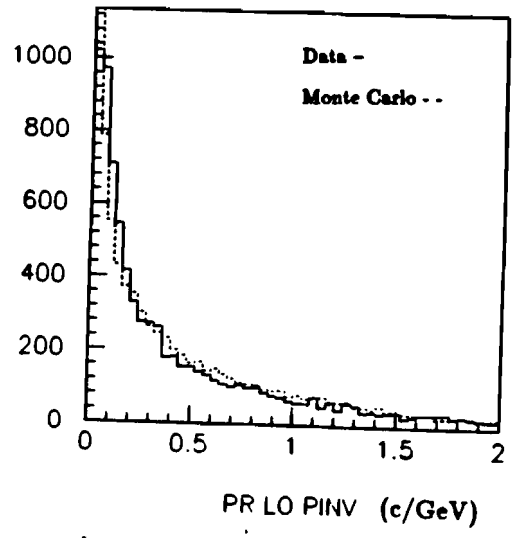

Figure 36. Track $1/p$ for D_2 and Monte Carlo.

§8.7 Monte Carlo Multiplicity Contamination Studies

The nature of the contamination of the raw multiplicity by tracks arising from secondary interactions and decays can be estimated from the analysis of Monte Carlo data.

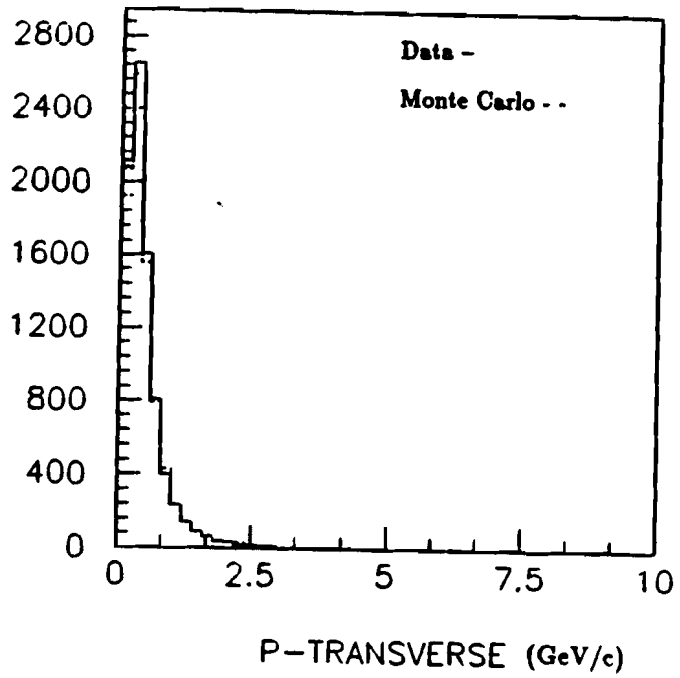

Figure 37. Lab frame track p_T for D_2 data and Monte Carlo. Note that p_T is measured with respect to the incoming beam direction.

As mentioned in section 7.1, the E665 vertex processor classifies the tracks in an event as "fitted" to the primary vertex or as "close" tracks. The term close track is an attempt to classify a track as not obviously primary without ruling the possibility out while the term fitted track implies that the track is likely

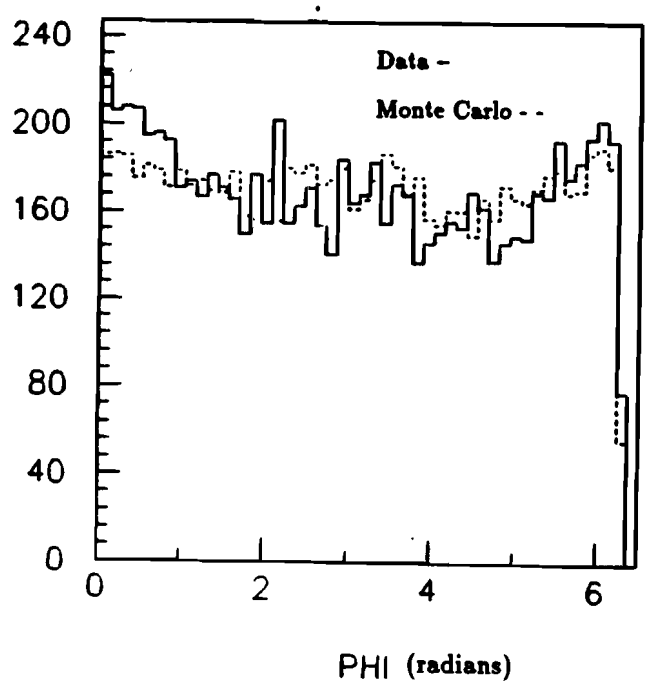

Figure 38. Track ϕ at vertex for D_2 data and Monte Carlo.

to be, but not definitely, a primary charged hadron. A plot of the minimum distance divided by the track error is given in figure 35 for all tracks(vertex processor fitted plus close). One can see that there is a peak in the plot for small values of this quantity and a subsequent long tail. Virtually no tail tracks are primary vertex tracks and only a small percentage of the closer unfitted tracks

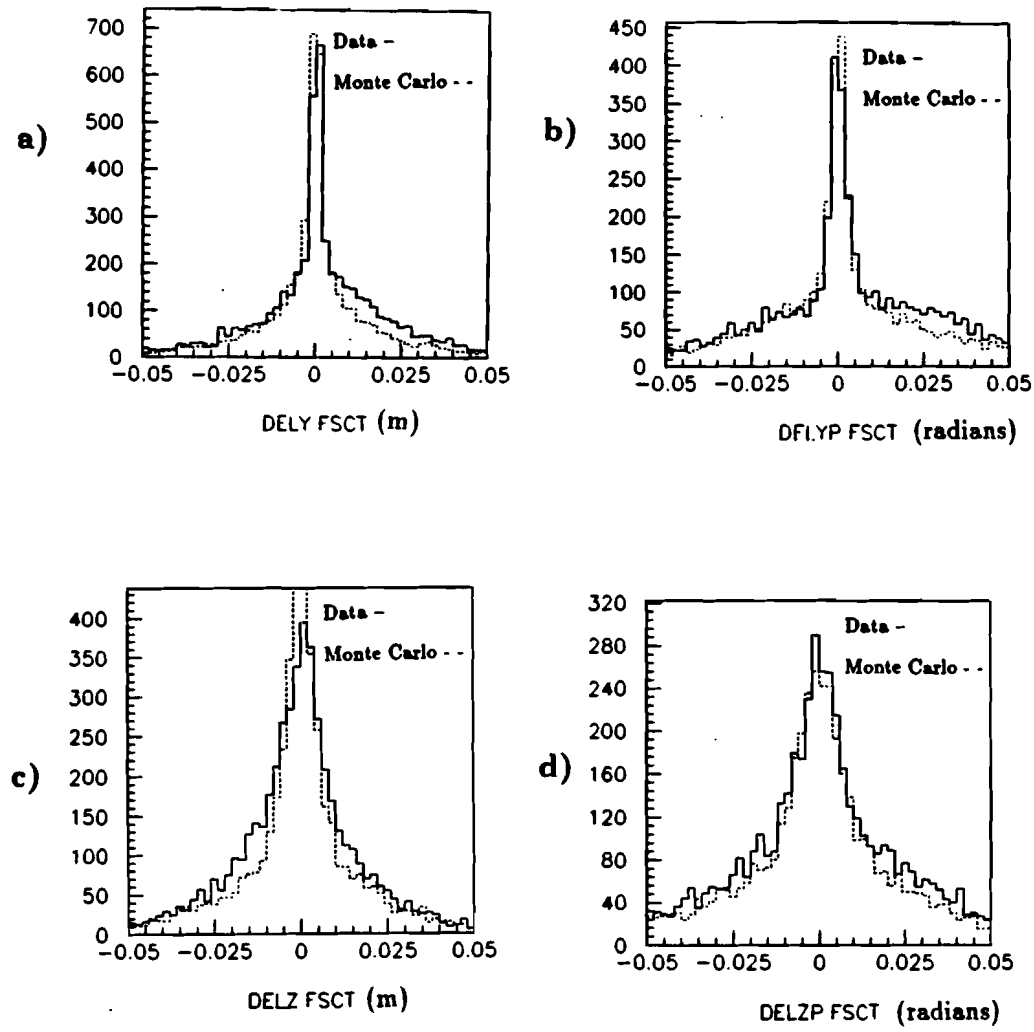

Figure 39. a) $y_{SC} - y_{FS}$ for D_2 data and Monte Carlo, b) $y'_{SC} - y'_{FS}$ for D_2 data and Monte Carlo, c) $z_{SC} - z_{FS}$ for D_2 data and Monte Carlo, d) $z'_{SC} - z'_{FS}$ for D_2 data and Monte Carlo

are true primary vertex tracks according to Monte Carlo studies. However, some secondary vertices are close to the primary beyond the resolution of the detector and thus contribute fitted tracks. Removal of these tracks on an event by event

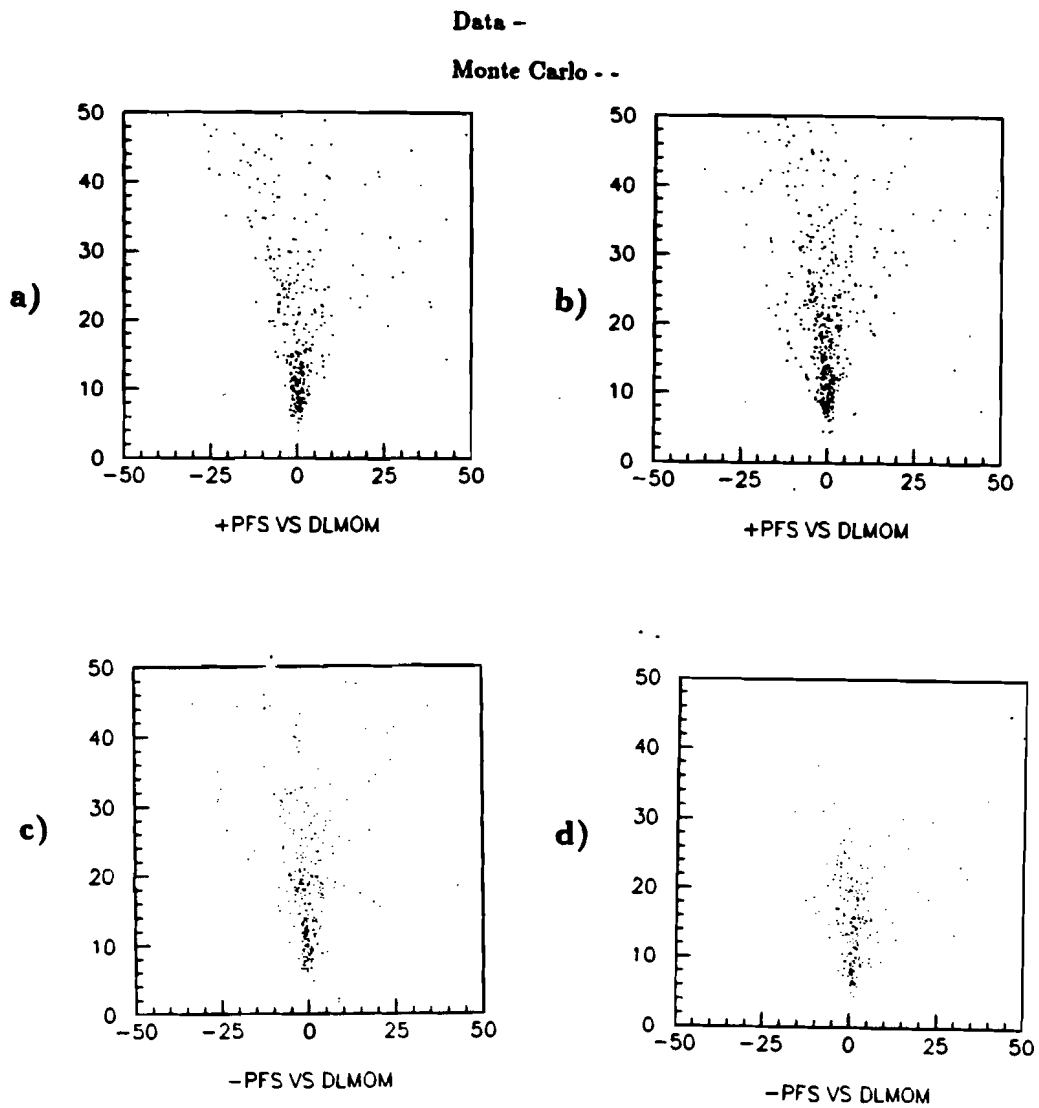

Figure 40. a) Positive track p_{FS} vs. $1/p_{SC} - 1/p_{FS}$ for D_2 data, b) Positive track p_{FS} vs. $1/p_{SC} - 1/p_{FS}$ for D_2 Monte Carlo, c) Negative track p_{FS} vs. $1/p_{SC} - 1/p_{FS}$ for D_2 data, d) Negative track p_{FS} vs. $1/p_{SC} - 1/p_{FS}$ for D_2 Monte Carlo.

basis is impossible, but statistical estimations of the presence of these tracks is possible by Monte Carlo simulation.

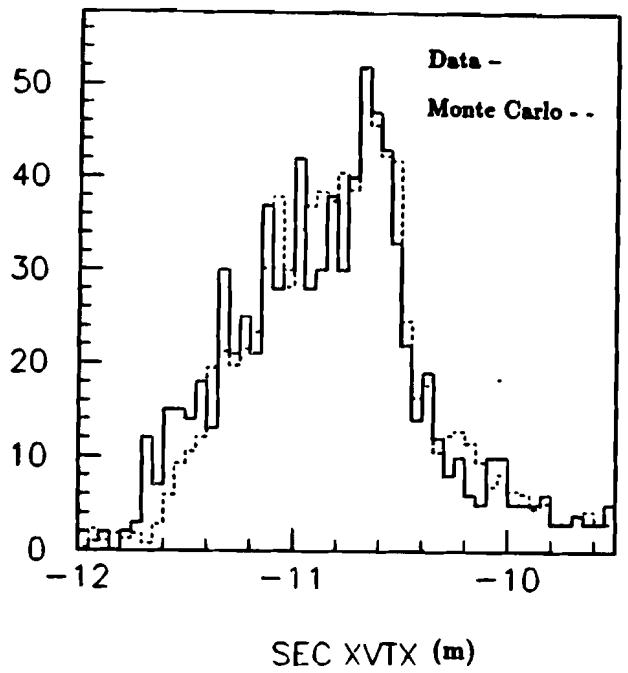

Figure 41. Secondary interaction vertex multiplicity as a function of interaction location.

A comparison of the number of secondary interactions from data and Monte Carlo indicates good agreement(see figure 41).

Given the reliability of the Monte Carlo from this figure, one may use it as a tool to reveal the presence of secondary tracks in the final multiplicity. The

contamination is given to be 9.5 % by examining the input Monte Carlo identity of all vertex accepted streamer chamber tracks.

There are certain processes which will cause there to be a varying multiplicity as a function interaction point within the target. Since there is a declining amount of target material downstream of a produced hadron as the vertex position within the target becomes more downstream, the hadron is less likely to re-interact. This will cause the uncorrected multiplicity to be higher for upstream interactions. In addition to this, the more downstream the vertex, the more likely that a scanner can tag obvious neutral decays. Thus, the opaqueness of the target results in higher multiplicity for upstream target interactions. Competing with these is the effect that charged hadrons may be absorbed in the target or converted to neutrals. Systematics for these processes will be discussed in sections 8.8 and 9.3.

§8.8 Multiplicity Acceptance

The uncorrected multiplicity described in section 8.4 will be reduced before Monte Carlo corrections by dropping all unmatched streamer chamber tracks which fall inside a 10 cm box centered on the x-axis(roughly parallel to the beam) since it is not possible to model the streamer chamber acceptance inside this box in an unbiased way. The forward spectrometer will be used exclusively in this region since the forward spectrometer Monte Carlo is more unbiased than simulating the streamer chamber track measurement procedure. It has been described in section 8.5. Outside this box, only the streamer chamber data is used since the forward spectrometer has almost no acceptance while the streamer chamber is believed to have an acceptance of almost 100 %. Most of the tracks in multiplicity still come principally from the streamer chamber even

without using unmatched beam region streamer chamber tracks. An important point here is that this is the method of counting which will be used for the physics plots of chapter 9. Two other methods will be discussed in this section for the purpose of systematic error estimation and cross checks on the data.

For interactions in the most upstream fifth of the target, 92 % of the average multiplicity comes from the streamer chamber. This value falls to 83 % for interactions in the most downstream fifth of the target. The numbers just given are averages. Although the upstream to downstream tendency is the same for all W and Q^2, the fractions vary for bins of W and Q^2 as shown in table 9.

The table shows that a larger fraction of tracks are found in the streamer chamber for lower W and that the upstream to downstream dependence is less pronounced as well.

Although the foward spectrometer always comprises less than 20% of the multiplicity, it accounts for a large fraction of $x_F > 0$ and thus its acceptance must be understood. The forward spectrometer acceptance of primary hadron tracks may be studied as a function of x_F using the Monte Carlo. The definition of forward spectrometer geometrical acceptance which will be used is that at least two PCF planes must be hit and that the hadron may not decay before reaching the third of five PCF planes. The PCF planes are special since they are the only wire chambers in E665 which reside in a significant magnetic field. The geometrical acceptance of the forward spectrometer by this definition is given in figure 42. After applying the 10 cm box cut used in the analysis, the acceptance is shown in figure 43. The fraction of tracks which enter the box, but escape the geometrical acceptance by decay,re-interaction or by magnetic field action on the trajectory is shown in figure 44 as a function of x_F.

Streamer Chamber Multiplicity Fraction

Q-Sq.(GeV^2)	W(GeV)	$\frac{SC}{FS}$	$\frac{SC}{FS}$(upstream $\frac{3}{5}$)	$\frac{SC}{FS}$(downstream $\frac{2}{5}$)
6.2	11.	.97	.97	.95
17.5	11.	.99	.99	.96
5.4	16.	.93	.94	.91
10.0	16.	.92	.94	.88
24.8	16.	.92	.94	.89
5.4	24.	.86	.89	.80
10.0	24.	.86	.88	.82
24.8	24.	.84	.89	.78

Table 9. Table of streamer chamber multiplicity dependence on X_{vertex}, Q^2, and W. The error on the ratios is approximately .02.

Some tracks which are reconstructed by the forward spectrometer software are ghosts. That is to say that the software has assembled a track from hits from different tracks. These reconstructed forward spectrometer tracks have

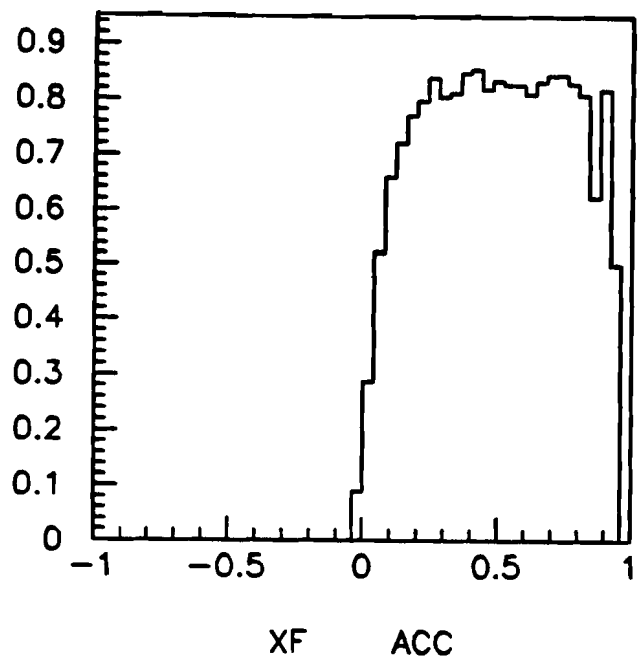

Figure 42. Forward spectrometer geometrical acceptance vs. x_F.

kinematics which don't resemble any input track from the Monte Carlo generator. The track parameters y, z, y', z' and p are compared with all Monte Carlo input tracks at corresponding forward spectrometer x coordinates to obtain a χ^2 for the pair. This χ^2 is shown in figure 45. The fraction of reconstructed primary vertex tracks passing both the box cut and the forward spectrometer geometrical

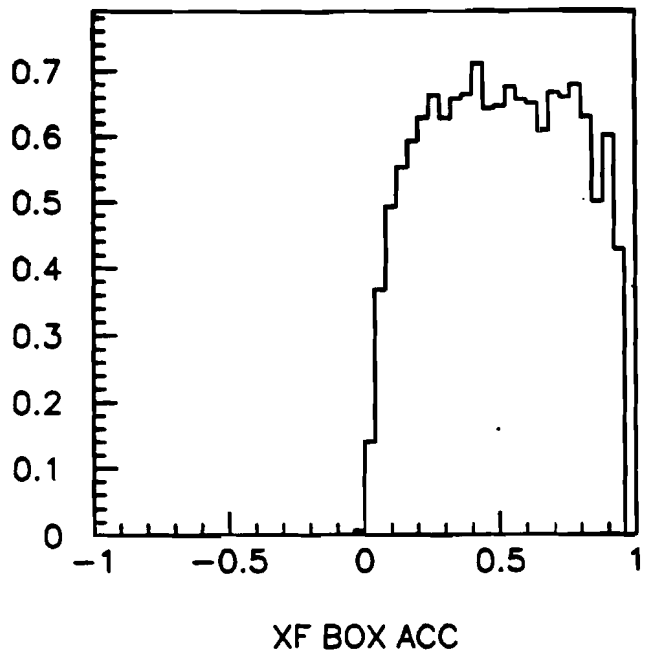

Figure 43. Geometrical acceptance of "box" cut vs. x_F.

acceptance cut which are ghosts is given in figure 46. With ghosts subtracted from the primary vertex multiplicity, figure 47 shows a comparison between the box geometrical acceptance and what is properly reconstructed. The software appears to be most confused at small positive x_F (see the "ghost" figure 46). At

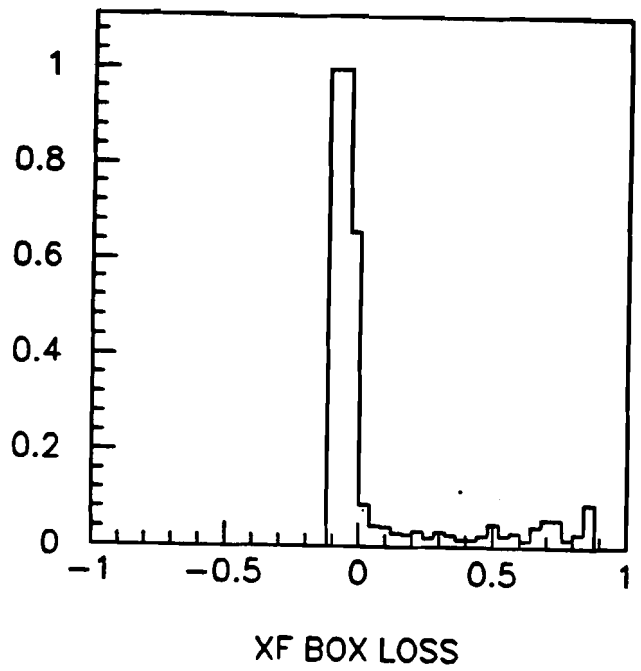

Figure 44. Acceptance of "box" cut lost to forward spectrometer vs. x_F.

large x_F, tracks are reconstructed at a higher x_F than the input. The error on the momentum for high momentum tracks is illustrated in this feature.

Now that the acceptance of both the streamer chamber and forward spectrometer have been discussed separately, the acceptance as a whole will be addressed. In figure 48 is shown the D_2 target uncorrected charged hadron

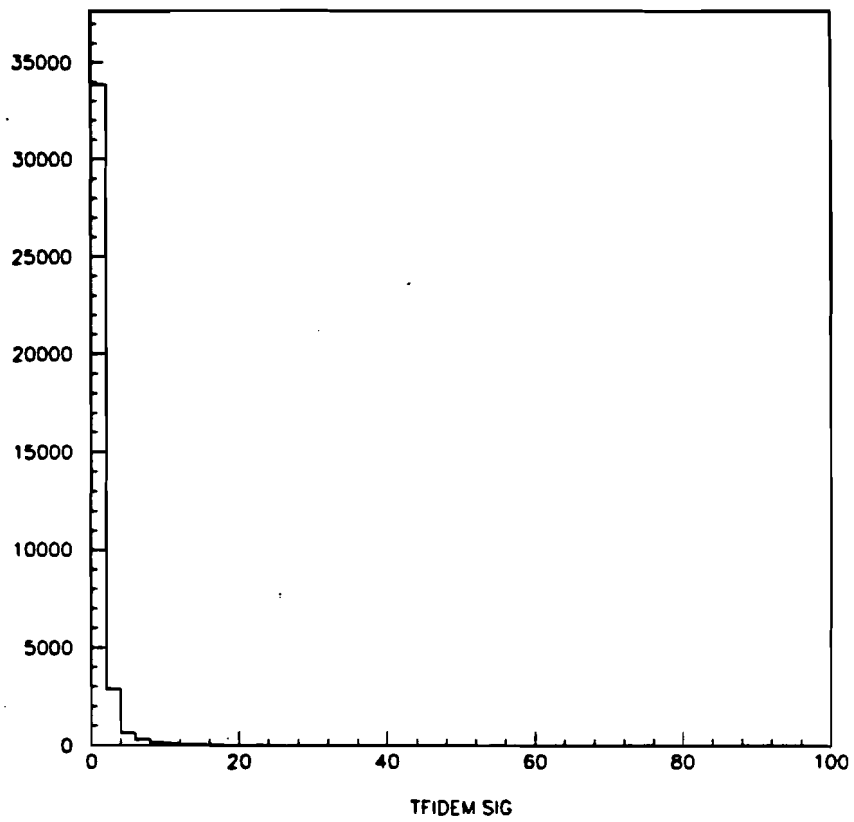

Figure 45. χ^2 of reconstructed track vs. input track match.

multiplicity distribution produced using the method where unmatched streamer chamber tracks in the beam region are dropped. The reader is reminded that this method is one which is used to produce the multiplicity plots of chapter 9.

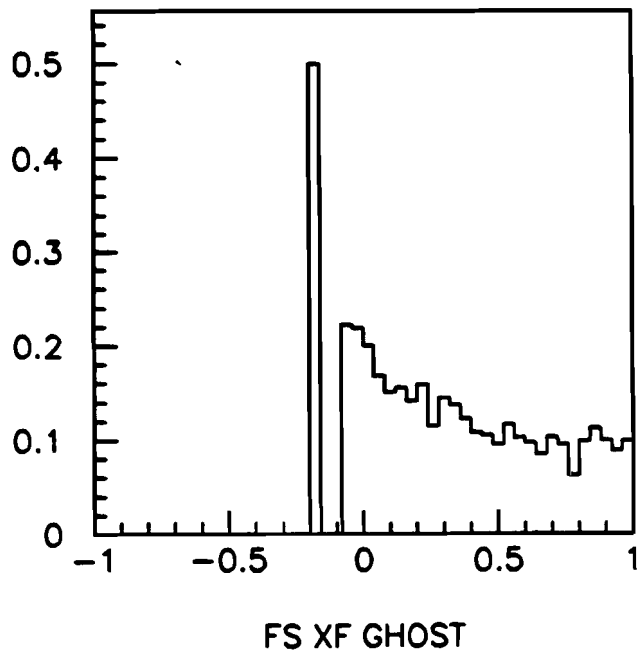

Figure 46. Fraction of ghost tracks vs. x_F.

To understand the acceptance losses imposed by this method, it is useful to compare the average multiplicity if these unmatched streamer chamber tracks are or are not dropped. In figure 49a is a plot of the ratio of the means from these two charged hadron multiplicity counting methods as a function of the muon interaction location.

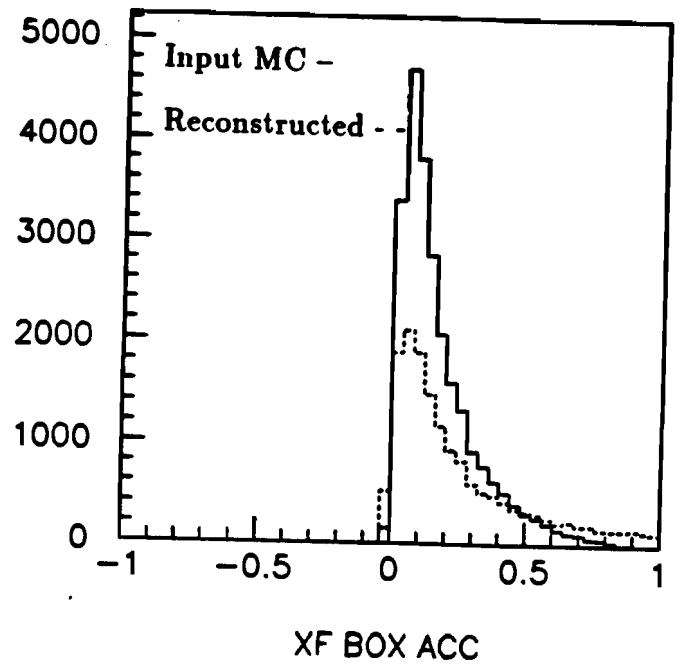

Figure 47. Number of tracks in geometrical acceptance to reconstruction vs. x_F.

The denominator represents the highest possible acceptance and reveals that the acceptance that will be used to do physics is 3% lower at the most upstream end for $W < 16GeV$ and 6% lower at higher W. At the downstream end, the multiplicity to be used is 15% lower for low W and 13 % lower for high W. As the

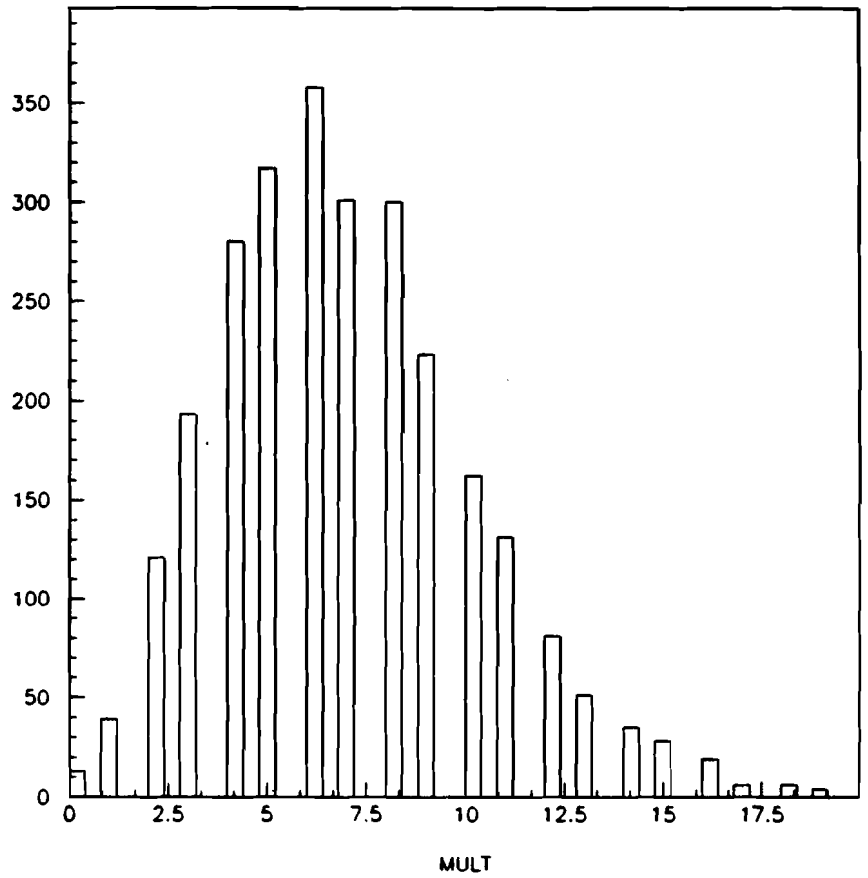

Figure 48. Uncorrected multiplicity for D_2.

forward spectrometer contributes a more significant fraction of the multiplicity, the acceptance falls.

If one then corrects the multiplicity with beam region streamer chamber tracks dropped using the Monte Carlo and divides the "match" method multiplicity by this, one can study the maximum possible acceptance of the detec-

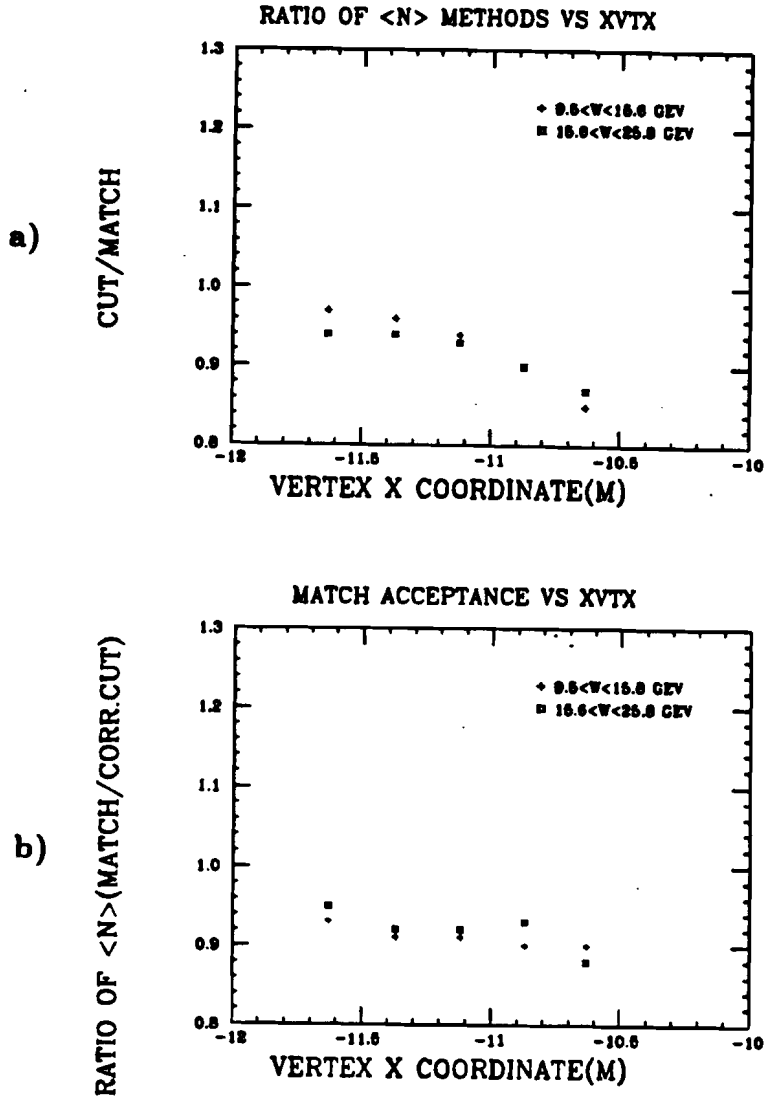

Figure 49. a)Ratio of competing multiplicity methods $< n >_{cut} / < n >_{match}$ as a function of muon interaction location in target. b) $< n >_{match}$ /*corrected* $< n >_{cut}$

tor(figure 49b). One sees that at the upstream end, 93% of the multiplicity is observed for low W and 94 % of the multiplicity is observed for high W. These values both fall to 90 % for very downstream interactions according to a fit

through the points. The downward slope of the curve indicates that the beam region streamer chamber acceptance falls for more downstream interactions provided that the Monte Carlo correction factor is correct. This is expected from considerations of track density in the beam region. A rising slope would have been a clue that double counting of tracks due to the combination of the two detector systems was a significant problem. Acceptance losses clearly dominate this effect.

To show the extent of systematic errors in the acceptance using the multiplicity measurement method where unmatched SC tracks are dropped, the corrected average multiplicity is presented as a function of x_{vertex}. After Monte Carlo corrections for all effects(trigger bias, geometrical acceptance, secondary interactions and decays,etc.), the average charged hadron multiplicity versus the x coordinate position(x is the axis nominally along the beam) of the vertex is shown in figure 50 for high and low W for both targets. The correction factors are shown in figure 51.

For $4.5 < ln(W^2) < 5.5$, the multiplicity is on the average lower than for $5.5 < ln(W^2) < 6.5$ as expected since there is less energy available for the production of hadrons. For both W regions, the multiplicity plotted against X_{vertex} is more or less flat and a bit low for upstream and downstream vertices. For these vertices, the forward spectrometer contributes tracks where its reconstruction ability is most questionable- namely at very high and low momentum respectively for the upstream and downstream vertices. Due to statistics, multiplicity for $6.5 < ln(W^2) < 7.0$ is shown only for D_2 and potential systematic problems are revealed due to the difference in upstream versus downstream corrected multiplicity. The variation here displays the extent to which the Monte Carlo can correct for the

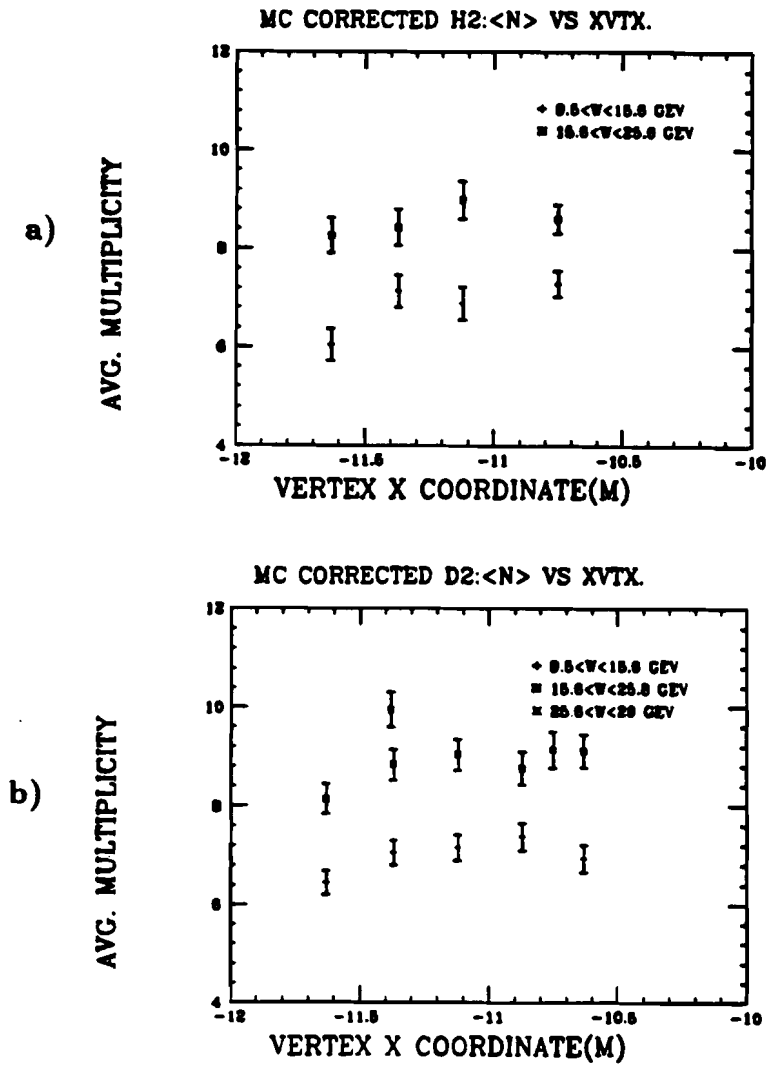

Figure 50. Monte Carlo corrected average multiplicity vs. X_{vertex} for a)H_2 and b)D_2.

things discussed in the last two chapters. Handling of these systematics will be discussed in section 9.3.

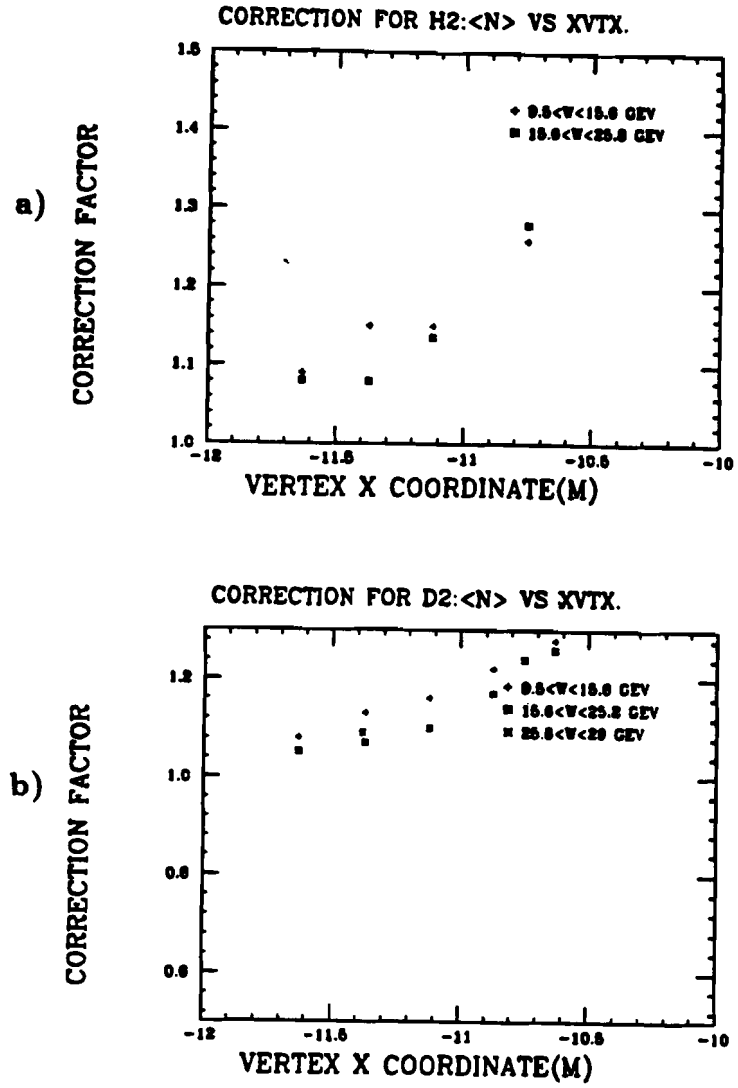

Figure 51. Monte Carlo correction factors vs. X_{vertex} for a)H_2 and b)D_2.

Even though the average corrected multiplicity has been checked for systematic x_{vertex} dependence, it is informative to compare the differential multiplicity distributions with Monte Carlo to check for systematics which may not show up in an average. For $4.5 < ln(W^2) < 7.0$, the multiplicity for interactions in the

upstream and downstream portions of the target has been plotted in comparison to the Monte Carlo in two different ways. In figure 52, the multiplicity excluding forward spectrometer and beam region streamer chamber tracks is given and supports the statement that data is slightly higher in charged hadron multiplicity than Monte Carlo for interactions in both sections of the target. This will be quantified in section 9.2. Note that the uncorrected differential multiplicity distribution from data has been compared to the equivalent distribution from Monte Carlo(namely the the software reconstructed multiplicity). Corrections to the data for a comparison to the input Monte Carlo are not done since the forward acceptance has been intentionally eliminated in order to study the streamer chamber alone and correcting the distribution would defeat this.

In figure 53, the multiplicity excluding only beam region streamer chamber tracks is given and shows that data is once again higher than Monte Carlo for interactions in both sections of the target. Note that the data is corrected and compared to the input Monte Carlo.

Finally, it should be noted that the comparisons of this chapter with Monte Carlo are merely searches for systematic errors and problems in methodology. Agreement with the Monte Carlo is not the goal, good correction factors for the data are.

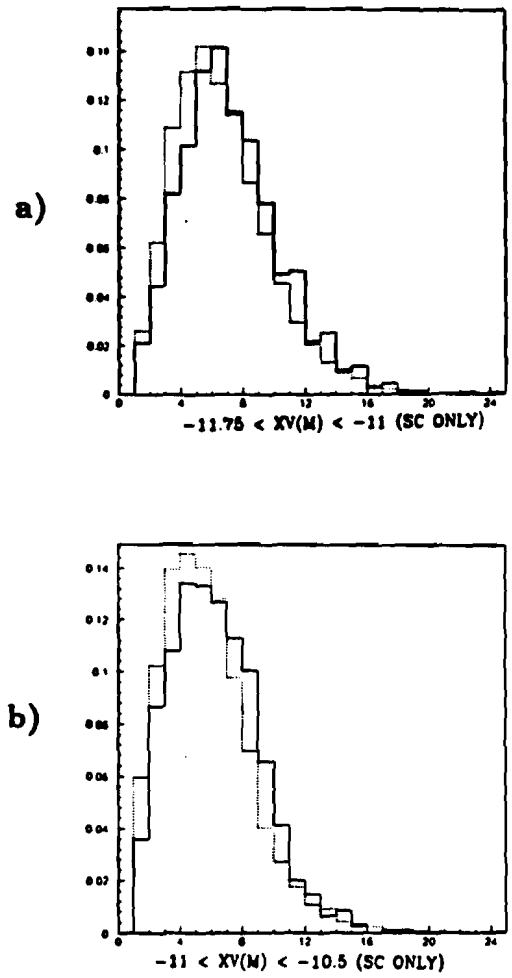

Figure 52. Multiplicity excluding the beam region for the a) upstream 3/5, b) downstream 2/5 of the target.

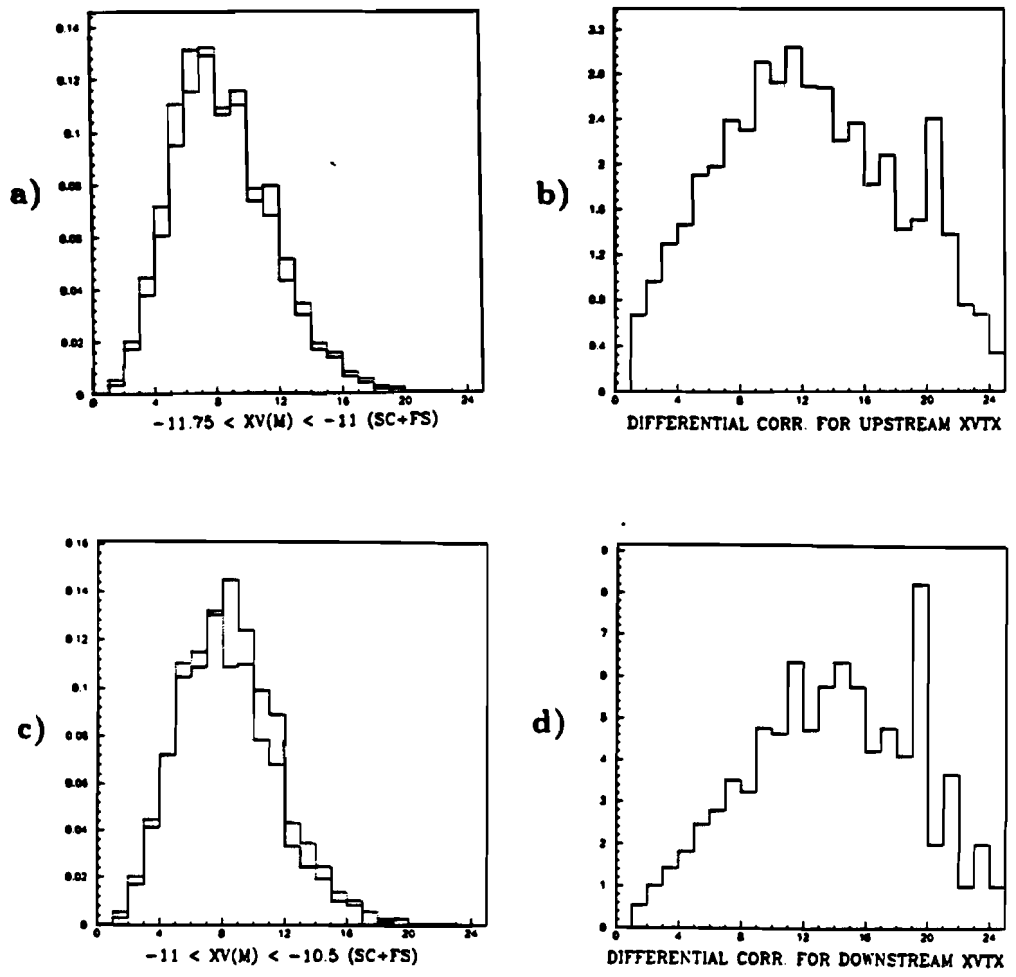

Figure 53. Multiplicity excluding the beam region streamer chamber tracks for the a)upstream 3/5 of the target with, b) the differential correction for a). The multiplicity for the downstream 2/5 of the target is c) with d) the differential correction for c).

Chapter 9 Results

§9.1 Multiplicity Distributions

A check on the statistical independence of the fragmentation in D_2 is the KNO scaling comparison of 4 W regions shown in figure 54. The curves are consistent with each other within the errors. KNO scaling is an important test since previous experiments disagree on its validity. As mentioned in chapter 2, UA5 interpreted its $P(n) < n >$ vs. $n/ < n >$ plot as a function of pseudo-rapidity as KNO scaling violation in $p\bar{p}$ (see section 2.2.7). At LEP[52], KNO scaling is not violated for e^+e^- at the Z^0 mass energy as a function of pseudo-rapidity. Statistics do not permit the further investigation of this issue here.

§9.2 Mean Multiplicity vs. Ln(W^2) and Ln(Q^2)

In this section, multiplicity as functions of Q^2 and W will be presented. One expects greater multiplicity as the available energy for producing hadrons(W) increases. At smaller Q^2, one expects more gluon induced events. Such events are higher in multiplicity than single quark DIS according to Monte Carlo predictions. Comparisons between H_2 and D_2 will be made as well as comparisons of the data to various Monte Carlo models of the hadronization process.

In figure 55 is shown the corrected average charged hadron multiplicity as a function of LnW^2 for H_2 and D_2.

In figure 56 is shown the correction factors used in figure 55 as a function of LnW^2.

The Tung and GHR Lund generated Monte Carlo predict a linear dependence of average multiplicity vs. ln(W^2) and the data confirms this. The data is 3 to 5% higher than the Morfin and Tung Monte Carlo at low W and consistent

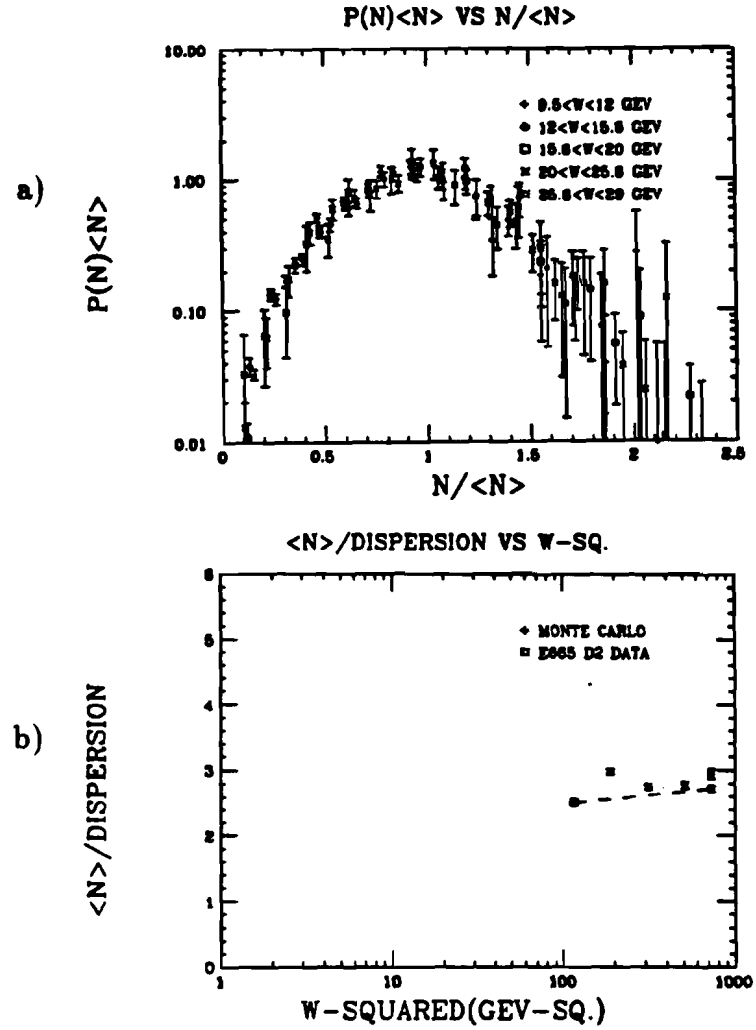

Figure 54. D_2 data a) $P(N) < N >$ vs $N/ < N >$, b) $< N >$/Dispersion.

at high W. It should be noted that Monte Carlo predicts an almost identical multiplicity for both targets as seen in the data. H_2 is 3 % higher at low W than the NA9[35,40] data for this target. This difference increases to 10 % at high W. Note that one can compare to the Monte Carlo used to generate corrections since

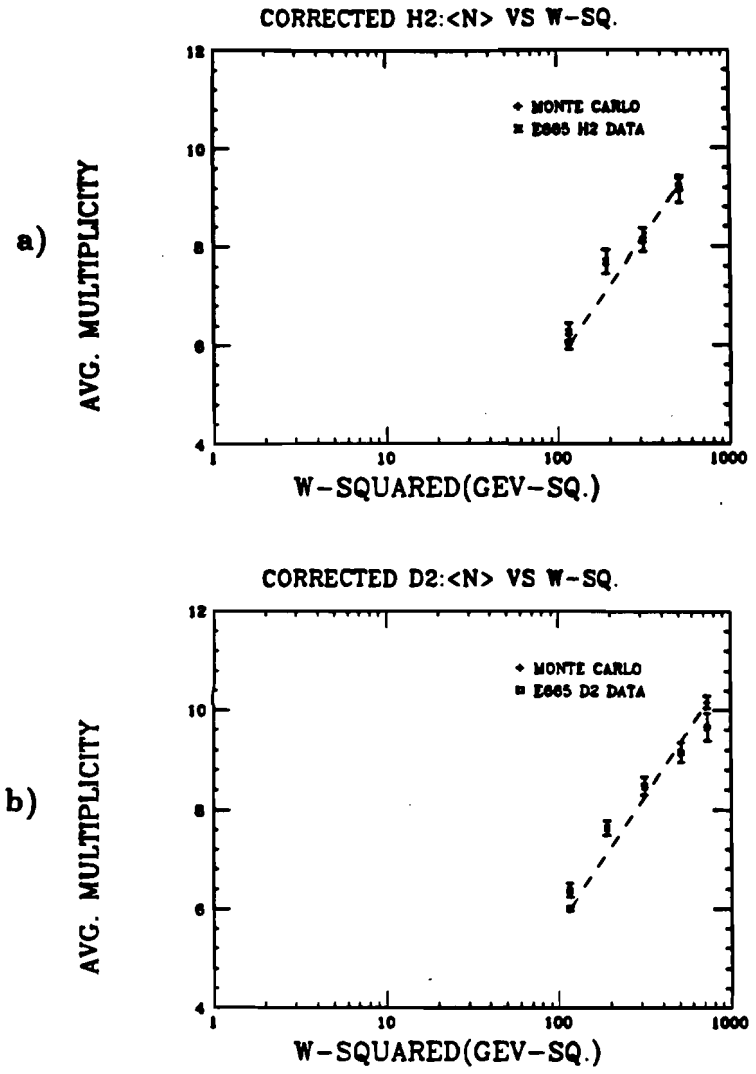

Figure 55. Corrected average charged hadron multiplicity as a function of LnW^2 for a)H_2 and b)D_2.

the corrections are thought to be independent of the number of input tracks to first order.

In figure 57, the H_2 average charged hadron multiplicity as a function of Q^2 is shown for $W < 20GeV$. The multiplicity value given for data is 5 % higher than

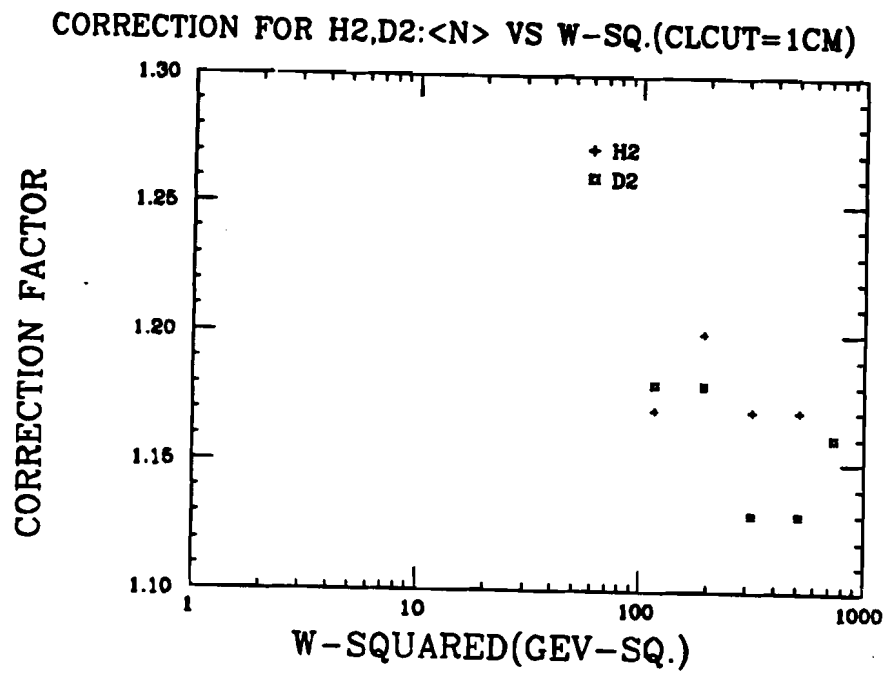

Figure 56. Correction factors as a function of LnW^2 for a)H_2 and b)D_2.

Monte Carlo in the $7 < Q^2 GeV^2$, $12 < W < 20GeV$ bins, but all other Q^2,W bins agree for $W < 20GeV$. The slopes are also in agreement.

For $20 < W < 29GeV$ (figure 58), the slopes and multiplicities are consistent within the errors.

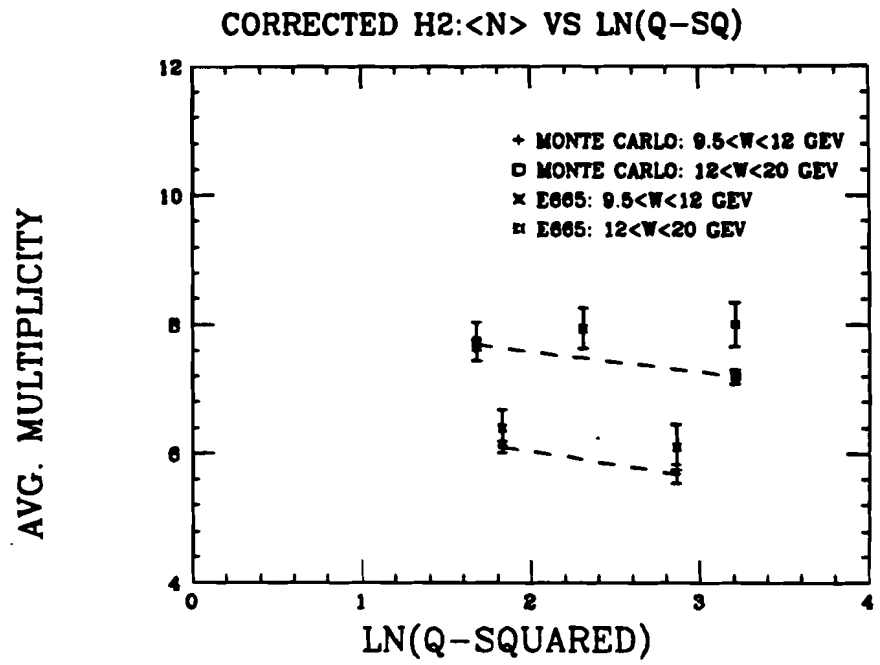

Figure 57. Corrected H_2 average charged hadron multiplicity as a function of $\mathrm{Ln}Q^2$ for $W < 20GeV$.

One may also compare the data with other models. The Q^2 and W^2 dependence of the H_2 multiplicity in the Lund shower model and in the Lund Ariadne shower model are shown in figure 59. In figure 60 is a comparison of the H_2' data to the mentioned models for $W > 20GeV$.

The Morfin and Tung model seems to best agree with the data at high W (and agrees well at lower W) since the shower models are .5 units low for $Q^2 < 7GeV^2$. Thus, string fragmentation with the Morfin and Tung QCD weights seems to produce Monte Carlo which agrees better with the data than these branching schemes with their input distributions. It should be noted that Morfin and Tung is a recent fit while the branching schemes were tuned using older data.

As well, the weights from Morfin and Tung can be separated into their contributions for single quark, quark-gluon and quark-quark jets. These are shown in figure 61 along with the average multiplicity one expects from each for $W > 20GeV$ in figure 62. If the statistics were better, one might be able to improve on the admixture or weights from these three processes assuming that the multiplicity from each is predicted correctly from string fragmentation.

In figure 63, the D_2 average charged hadron multiplicity as a function of Q^2 is shown for $W < 20GeV$.

The multiplicity values given for D_2 data are 5 % higher than Monte Carlo in the range $9.5 < W < 12GeV$, but the slopes are consistent. For $12 < W < 20GeV$, the lowest Q^2 multiplicity value given for D_2 data is 5 % higher than the Monte Carlo, but the slope of the data is flat while the slope of the Monte Carlo is negative resulting in larger disagreement(7 %) for $Q^2 > 7GeV^2$.

For $20 < W < 29GeV$ (figure 64), the two highest Q^2 multiplicities agree, but the Monte Carlo has a negative slope while data has a positive slope.

The Q^2 and W^2 dependence of the D_2 multiplicity in the Lund shower model and in the the Lund Ariadne shower model are shown in figure 65. In figure 66 is a comparison of the D_2 data to the mentioned models for $W > 20GeV$..

The Morfin and Tung multiplicity predictions are more consistent with D_2 multiplicity results from data than other models. One would be able to improve

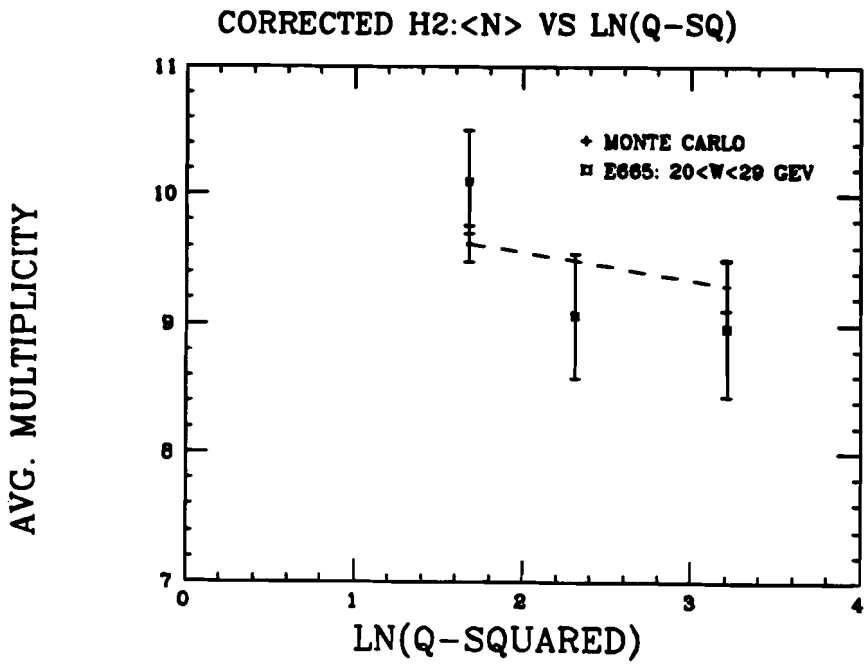

Figure 58. Corrected H_2 average charged hadron multiplicity as a function of $\mathrm{Ln}Q^2$ for $W > 20GeV$.

on the admixture of the three jet types(figure 67) with the information in the figure as with hydrogen were statistics better.

A comparison between forward and backward multiplicity was done for the D_2 target. In figure 68, corrected forward and backward multiplicity distribu-

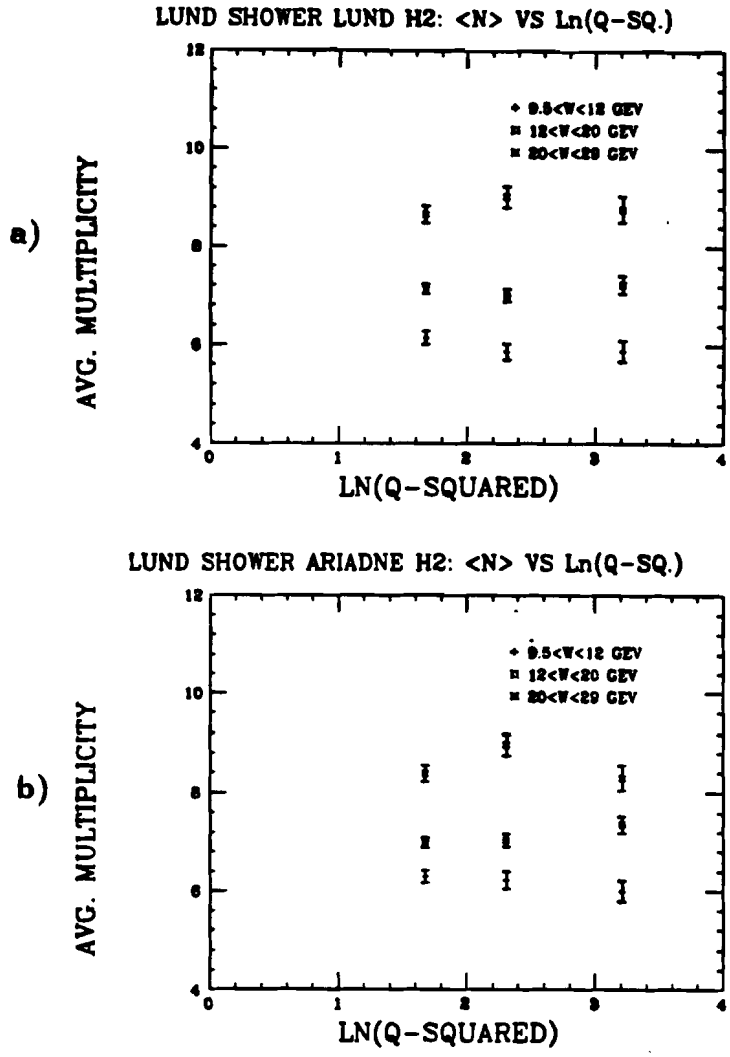

Figure 59. a)Lund shower and b)Lund Ariadne shower multiplicity predictions.

tions are shown. Data is higher than Monte Carlo by 15 to 20% and the forward data curve has negative concavity while Monte Carlo is linear. The backward data curve displays the opposite behavior with the multiplicity in agreement with Monte Carlo at low W and 10% lower at high W. The Monte Carlo multiplicity is once again linear as a function of W.

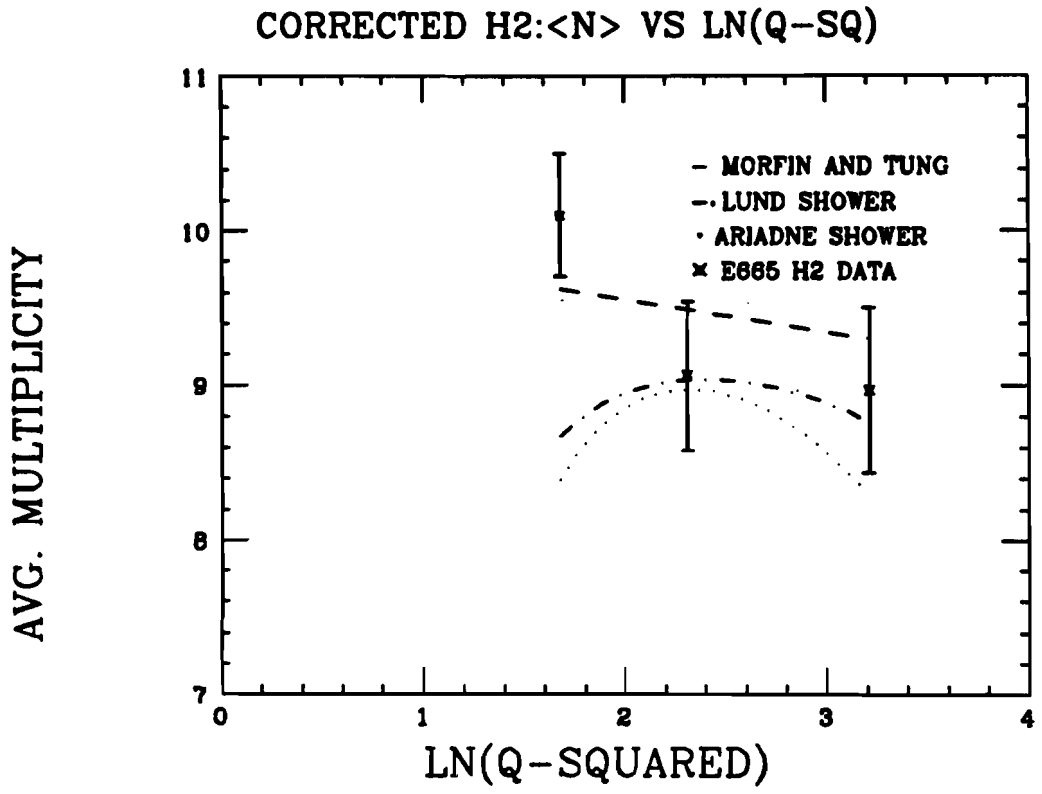

Figure 60. Corrected H_2 average charged hadron multiplicity as a function of $\mathrm{Ln}Q^2$ for $29 > W > 20GeV$ compared to some Monte Carlo models.

In figure 69, Monte Carlo correction factors are shown. It is clear that the forward multiplicity corrections are 1.5 times larger than the backward thus enhancing any systematic errors present. The size of the forward corrections is due to the degradation in x_F by re-interactions and decays. This degradation

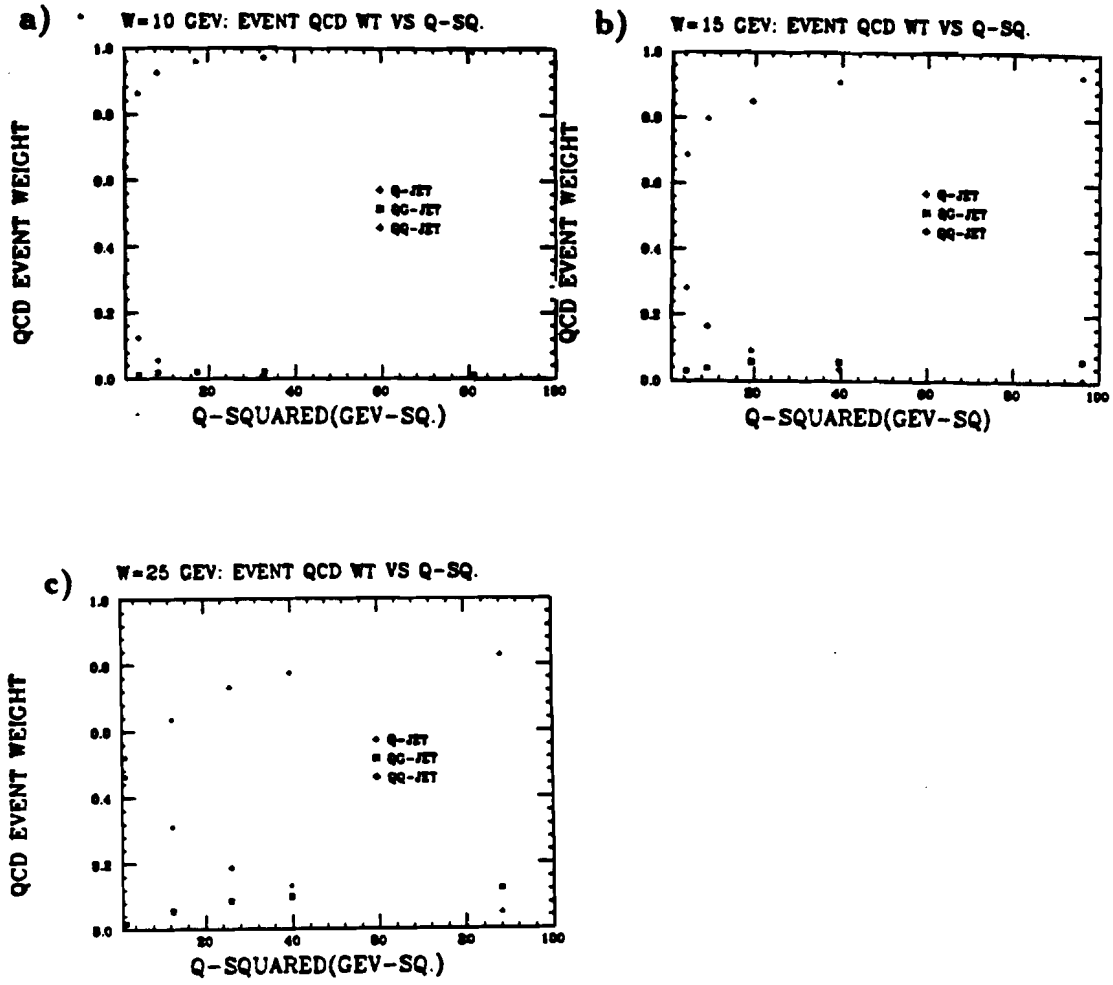

Figure 61. Contributions of q, qg and qq to DIS for a) $9.5 < W < 12GeV$, b)$12 < W < 20GeV$, $20 < W < 29GeV$.

results in positive x_F tracks being reconstructed as negative as illustrated in figure 70a. In this figure, x_F for secondary tracks fit to the primary by the vertex processor is shown. Comparison of the Monte Carlo generated primary track x_F

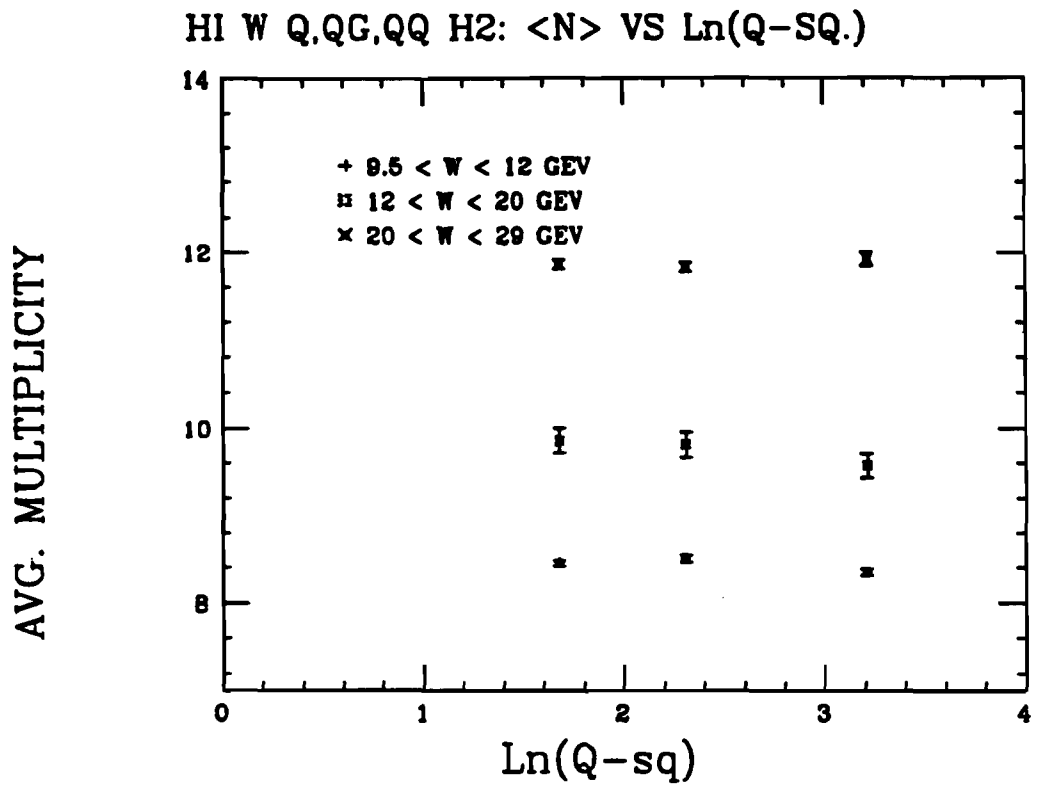

Figure 62. H_2 Multiplicity vs. Q^2 of q, qg and qq for $20 < W < 29GeV$.

with reconstructed (figure 70b) shows the extent of this effect. Reconstructed Monte Carlo and data(figure 71) are in reasonable agreement.

§9.3 Systematics

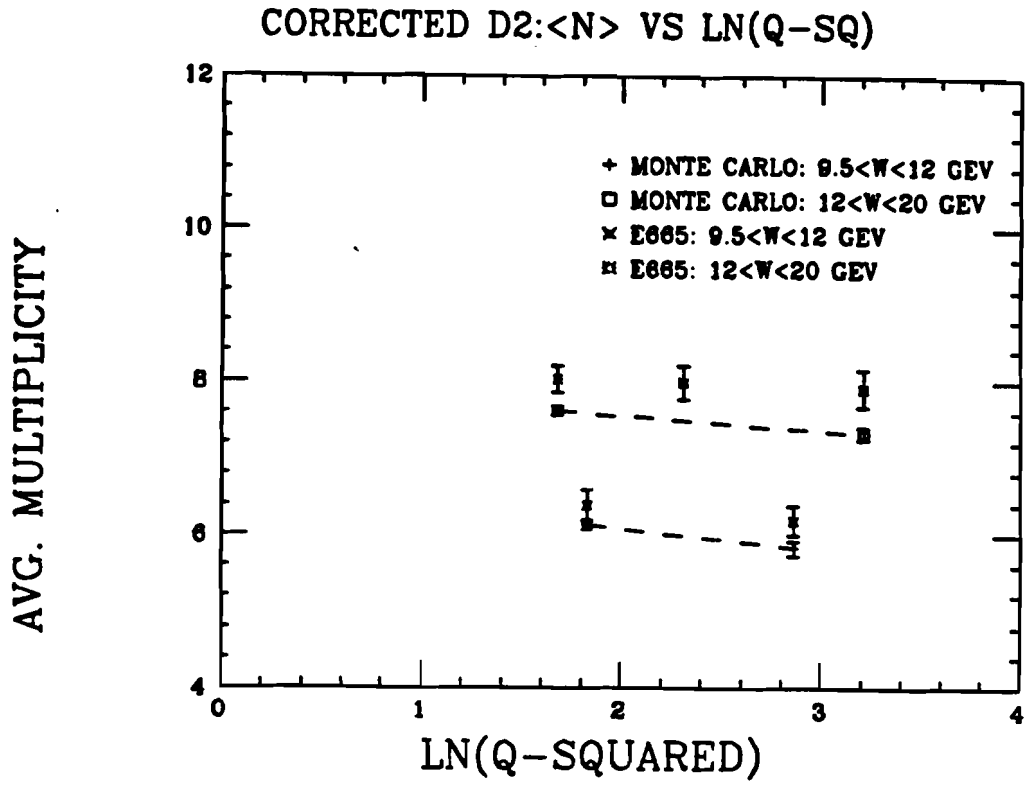

Figure 63. Corrected D_2 average charged hadron multiplicity as a function of $\mathrm{Ln}Q^2$ for $W < 20GeV$.

To estimate the systematic error due to acceptance, the multiplicity as a function of x_{vertex} was measured for fixed W. If valid corrections are applied, then the corrected multiplicity as a function of x_{vertex} should be constant for constant W. The extent to which this is true is given by the standard deviation of the mean multiplicity for different W and targets in table 10. The variation

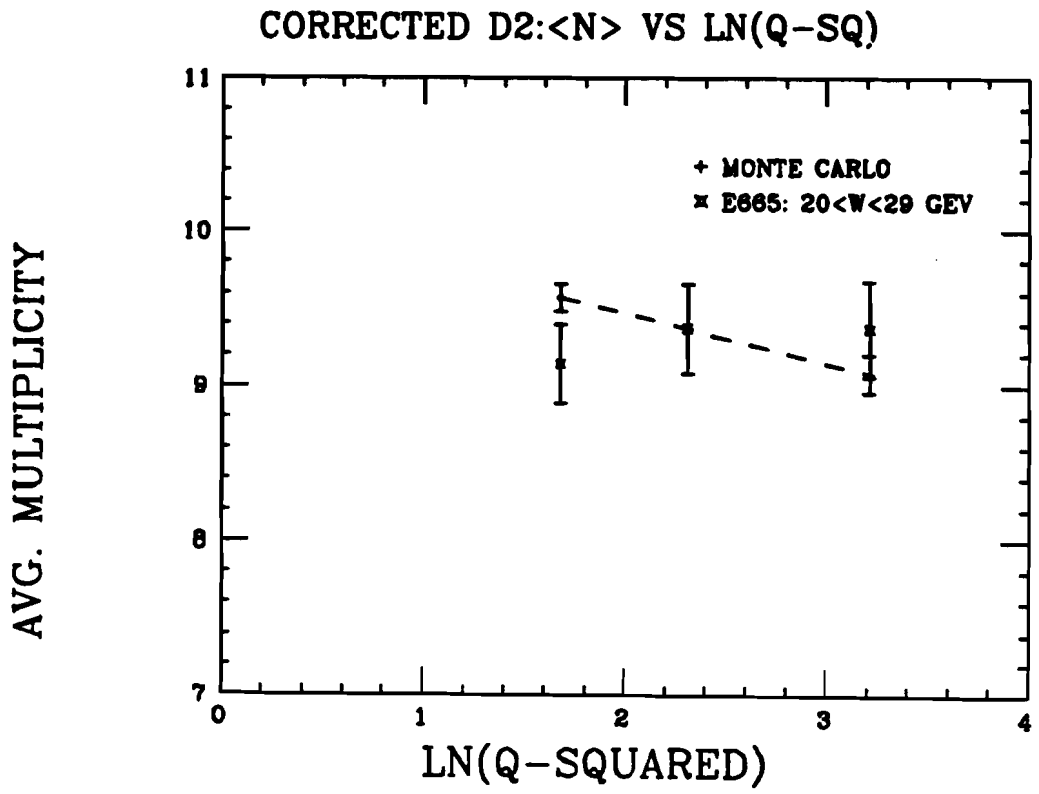

Figure 64. Corrected D_2 average charged hadron multiplicity as a function of $\mathrm{Ln}Q^2$ for $20 < W < 29GeV$.

is consistent with the statistical errors except for $W > 25GeV$. Here there is substantial x_{vertex} dependence perhaps providing an explanation for the weakness in rise for that point in figure 55.

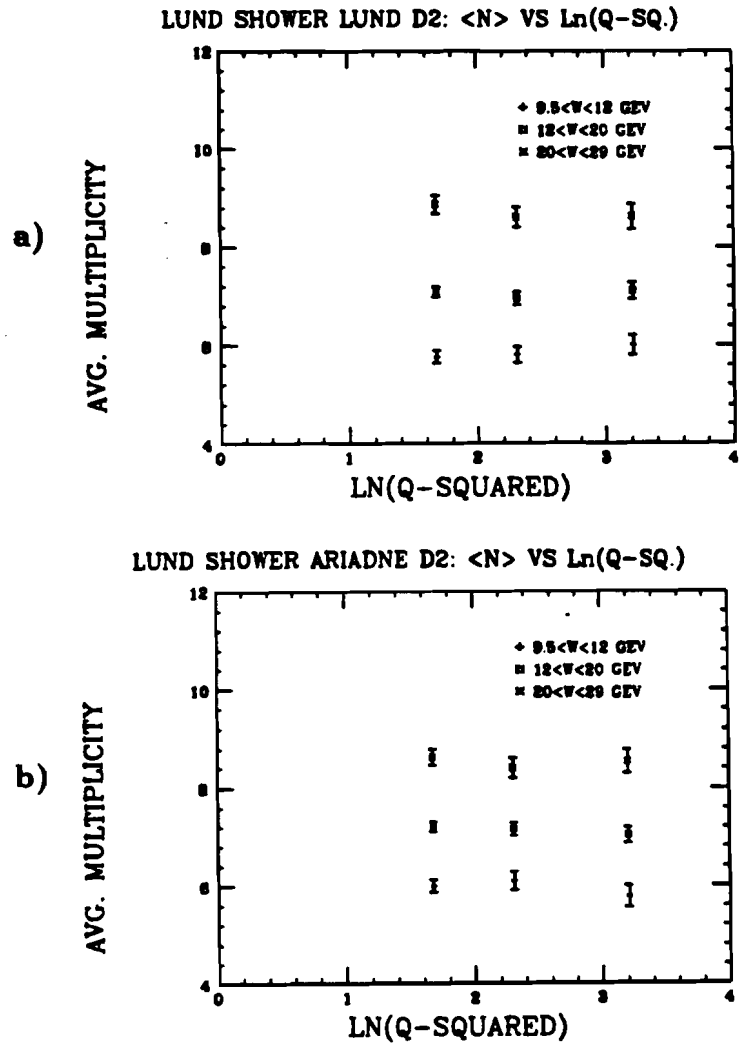

Figure 65. D_2 a)Lund shower and b)Lund Ariadne shower multiplicity predictions.

To address the concern that systematics based on the method of correcting the multiplicity may be present, the multiplicity was calculated in three different ways. The first way is the method which has been used thus far- correcting the mean with the ratio of input Monte Carlo over reconstructed Monte Carlo.

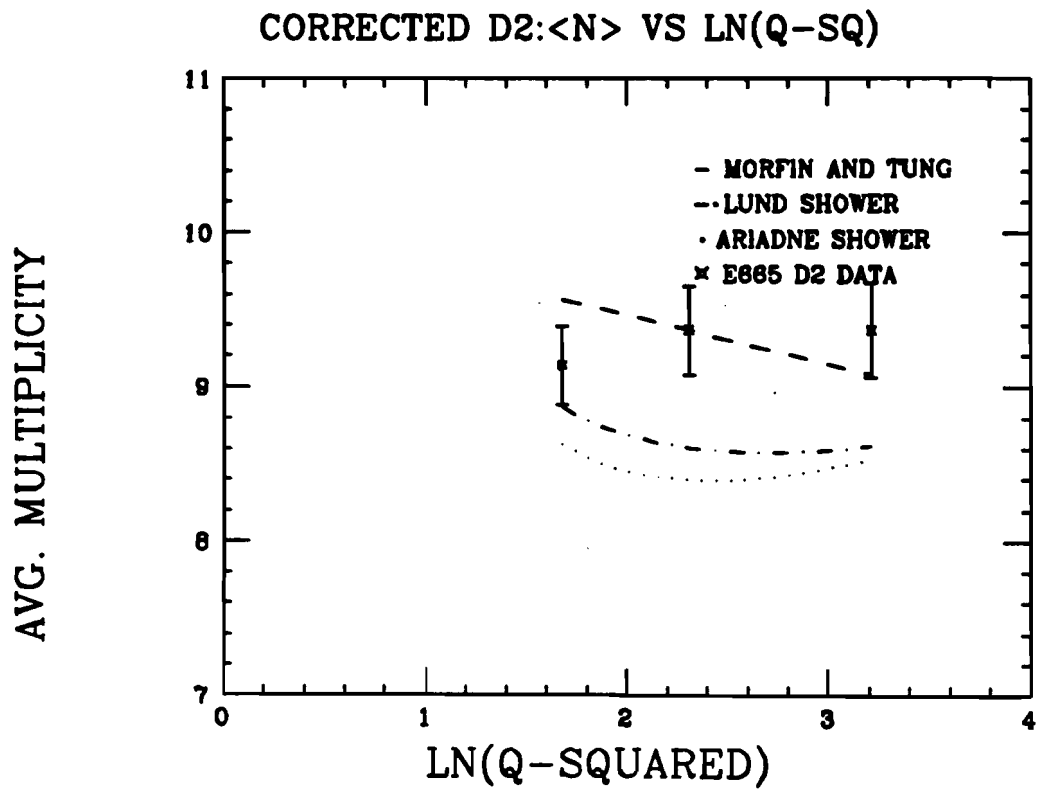

Figure 66. Corrected D_2 average charged hadron multiplicity as a function of $\mathrm{Ln}Q^2$ for $29 > W > 20GeV$ compared to some Monte Carlo models.

Tracks which come within a minimum distance of $1cm$ without being classified as belonging to the primary vertex by the vertex processor are added in with this method. A second measurement is obtained by increasing the "close" track

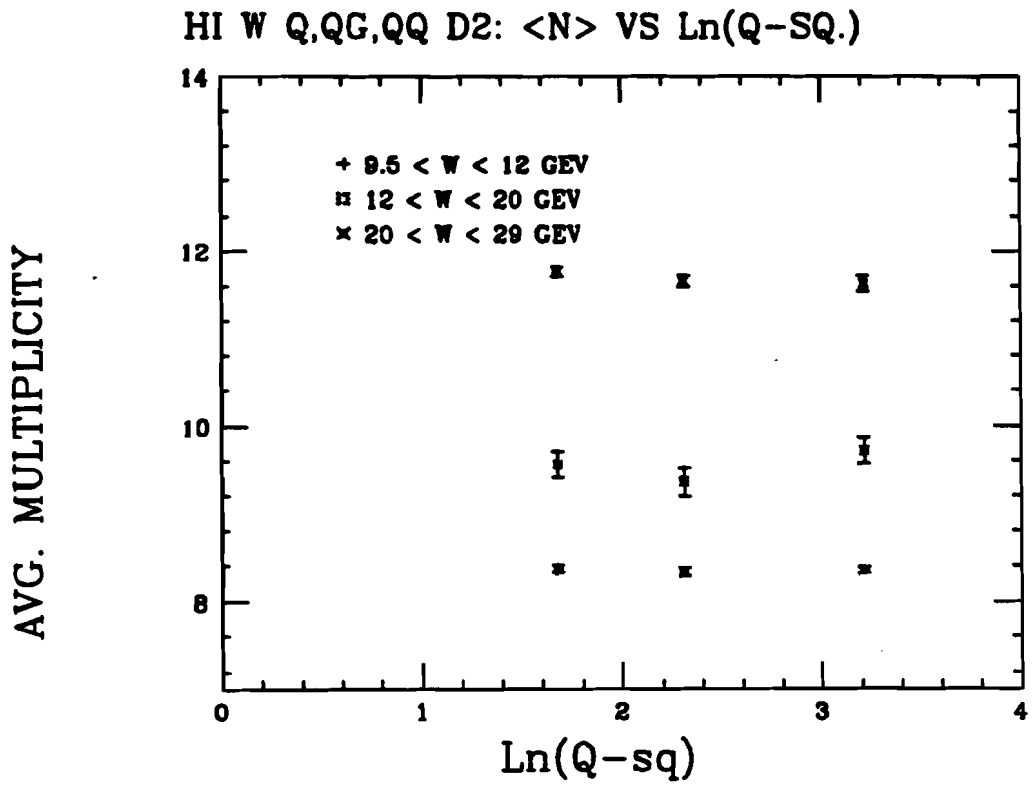

Figure 67. D_2 Multiplicity vs. Q^2 of q, qg and qq for $20 < W < 29GeV$.

cut to $5cm$. This cut makes the multiplicity more susceptible to hadrons created upstream of the target, decays and secondary interactions and forward spectrometer "ghost" tracks(see chapter 7) while diminishing losses due to poor alignment. A third method corrects the multiplicity by multiplying each bin of the differential multiplicity by the ratio of input Monte Carlo multiplcity over

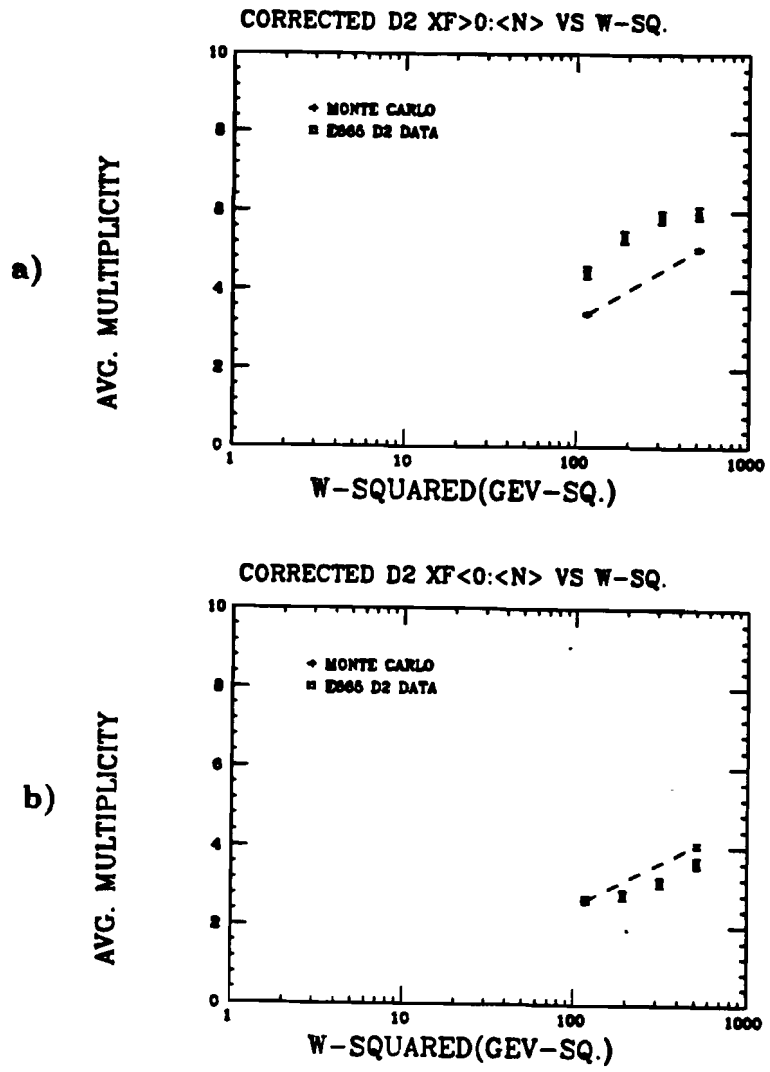

Figure 68. Corrected D_2 average charged hadron multiplicity as a function of LnW^2 for a)$x_F > 0$, b)$x_F < 0$.

reconstructed Monte Carlo. Note that H_2 will have contributions from only odd multiplicity events with this method due to charge conservation. A plot of Monte Carlo corrected multiplicity for H_2 and D_2 as a function of $Ln(w)$ is given in figure 72 using the three methods. The correction factors are given in figure 73. From figure 72, one can estimate the systematic error on the multiplicity

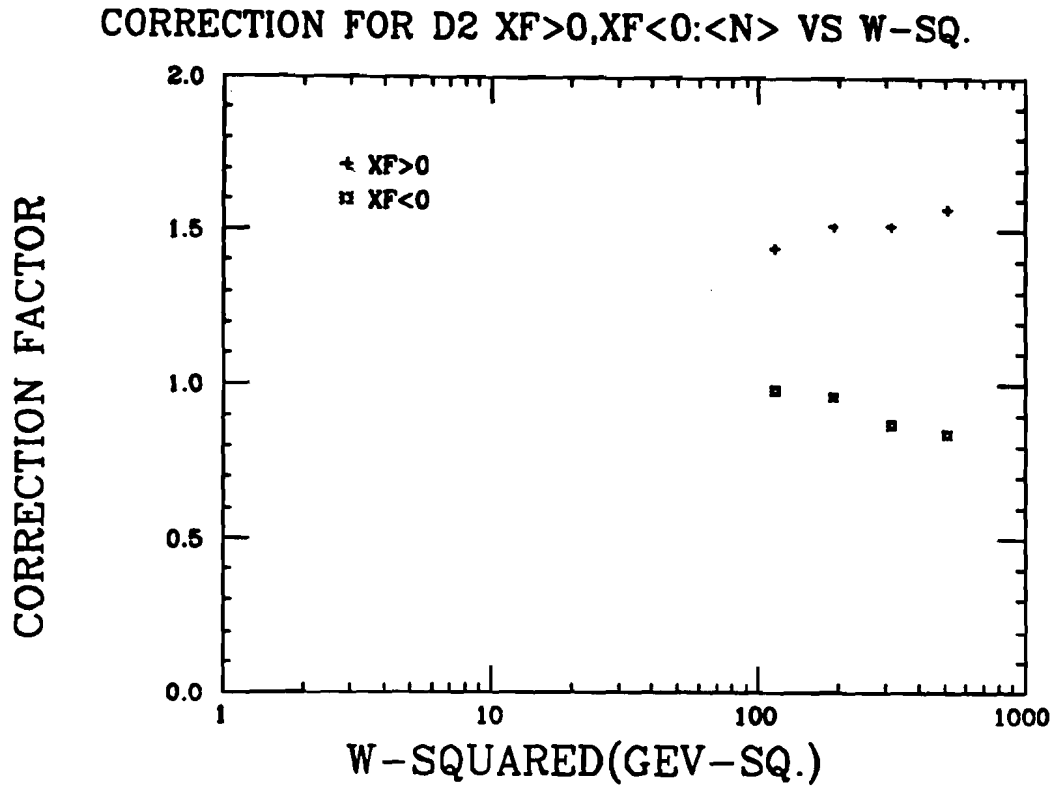

Figure 69. Multiplicity correction factors for D_2 as a function of $\mathrm{Ln}W^2$ for $x_F > 0$, $x_F < 0$.

due to method by subtracting largest and smallest multiplicity measurements from the average of the three. The results are in table 11. D_2 has much smaller systematic errors due to method than H_2.

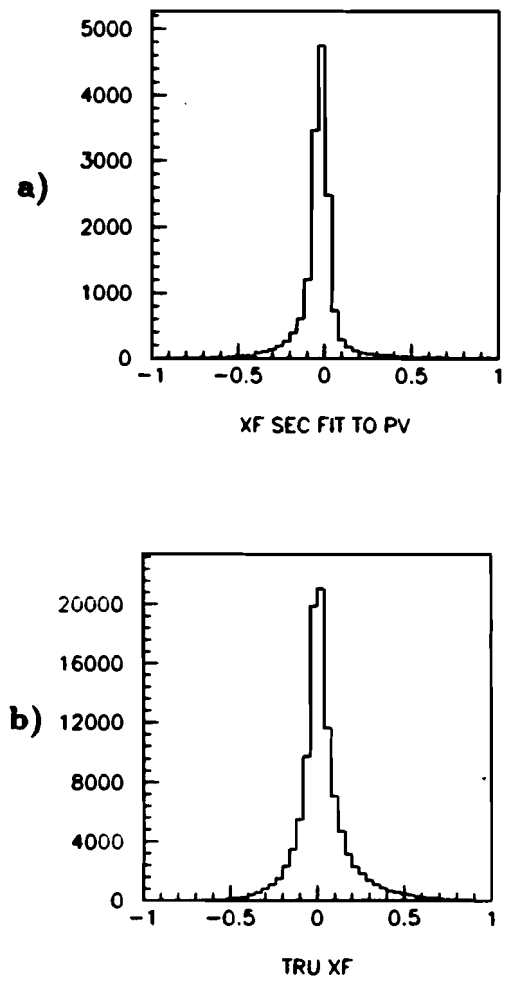

Figure 70. a)Reconstructed D_2 Monte Carlo x_F for secondaries contaminating the primary vertex, b) Generated Monte Carlo x_F.

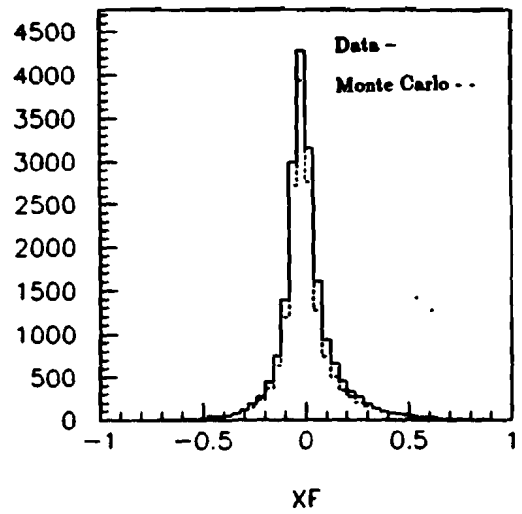

Figure 71. D_2 x_F.

Multiplicity x_{vertex} systematics

Target	$Ln(W^2)$	$< n >$	σ
H_2	4.5 to 5.5	6.84	.34
H_2	5.5 to 6.5	8.57	.39
D_2	4.5 to 5.5	6.99	.56
D_2	5.5 to 6.5	8.77	.31
D_2	6.5 to 7.0	9.54	.58

Table 10. Multiplicity x_{vertex} systematics. The standard deviation can be interpreted as a systematic error.

Multiplicity Method Systematics

Target	$Ln(W^2)$	$< n >$ with error
H_2	4.75	$6.14 + .12 - .17$
H_2	5.25	$7.35 + .34 - .37$
H_2	5.75	$8.05 + .08 - .05$
H_2	6.25	$9.32 + .39 - .23$
D_2	4.75	$6.36 + .08 - .09$
D_2	5.25	$7.55 + .08 - .09$
D_2	5.75	$8.42 + .04 - .06$
D_2	6.25	$9.16 + .09 - .07$
D_2	6.63	$9.66 + .01 - .03$

Table 11. Systematics associated with multiplicity method used.

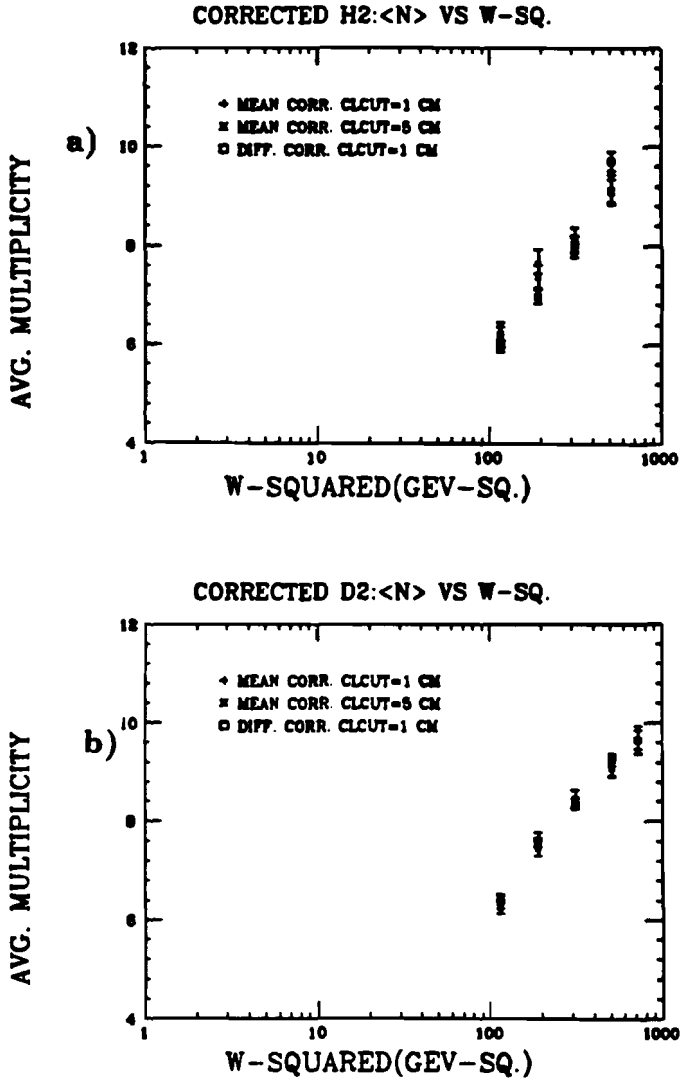

Figure 72. $< n >$ vs. $ln(W^2)$ using three different methods for a)H_2, b)D_2.

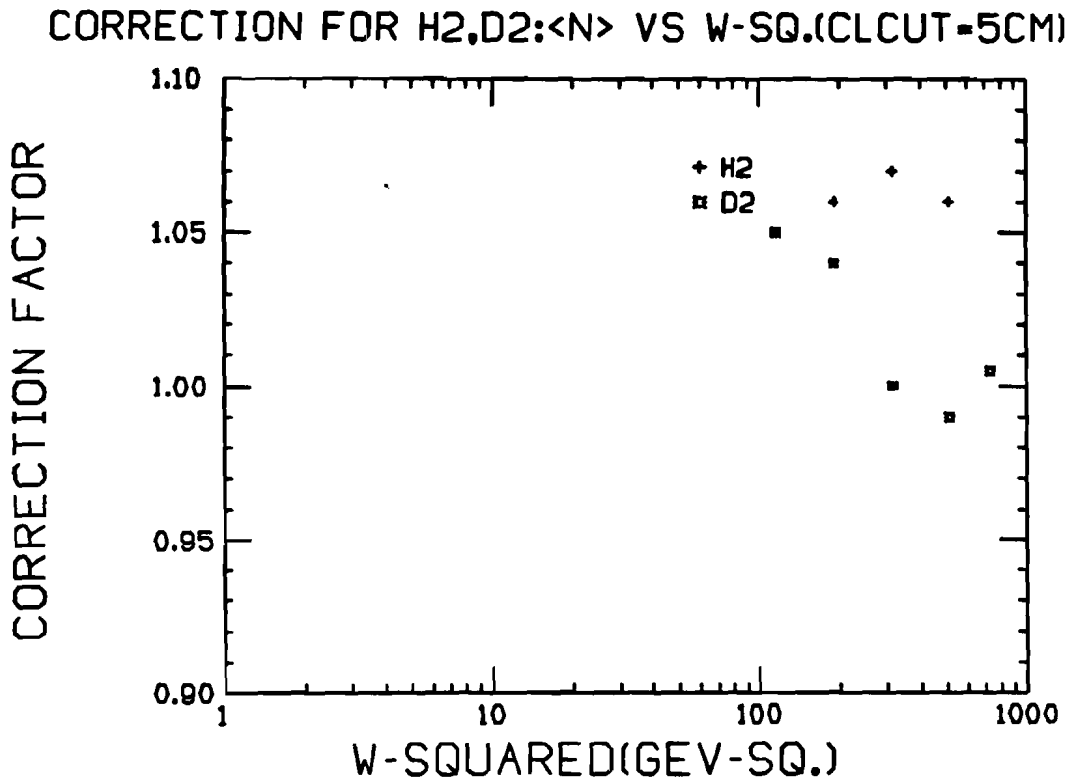

Figure 73. $< n >$ vs. $ln(W^2)$ correction factors for figure 72. a)H_2, b)D_2.

Chapter 10 Conclusions

In this study, charged hadron multiplicity was measured using a streamer chamber and forward tracking as a function of Q^2 and W in 490 GeV deep inelastic muon scattering from H_2 and D_2 targets. The charged track kinematics were obtained from reconstruction of the muon vertex and spectrometer fits, while the the number of primary hadron tracks associated with that vertex was ascertained by fits to the data and Monte Carlo modeling.

The data for both H_2 and D_2 is higher in multiplicity than that of NA9 H_2 for the same W and is generally consistent with Morfin and Tung structure functions in Lund Monte Carlo framework. The corrected data is higher than the Lund shower models with the largest discrepancies being at higher W. If one believes the multiplicity predictions of Lund, then one concludes that Morfin and Tung predict the correct admixture of QCD processes. Lund predicts multiplicities of roughly 11.5,9.5 and 8.25 for quark-quark, quark-gluon and single quark jet when $29 > W > 20GeV$. In this W range, the admixtures predicted by Morfin and Tung placed single quark jet DIS in the 50 to 80% range(increasing with Q^2), quark-quark at 45 to 10%(falling with Q^2) and quark-gluon jets at the few percent to 10 % level.

Data is consistent as well with the weak Q^2 dependence of Morfin and Tung. Kiselev and Petrov predicted a strong positive slope with $\ln(Q^2)$ if gluon bremsstrahlung dominated DIS as in their model.

H_2 and D_2 are consistent within the errors supporting the statement that the DIS events are predominantly sea quark scatters. This is expected since more than 90% of the data is below x_{Bj} of .2 which is the value at which previous experiments predict sea quark domination to occur.

References

1. H. L. Anderson et al., Phys. Rev. Lett. 38,1450(1977).

2. H. L. Anderson et al., Phys. Rev. Lett. 37,4(1976).

3. H. L. Anderson et al., Phys. Rev. Lett. 36,1422(1976).

4. H. L. Anderson et al., Phys. Rev. D20 No.11, 2645(1979).

5. O.C. Allkofer et al.,"A large magnetic spectrometer system for high energy muons",Nuc. Inst. Meth. 179,445(1981).

6. J. Drees and H. E. Montgomery,"Muon Scattering", Ann. Rev. Nucl. and Part. Sci. 33, 383(1983).

7. U. Timm et al, Nukleonika(Poland) V.26 No.11-12,1227(1981).

8. S. L. Wu, "e^+e^- physics at Petra- the first five years",Physics Reports 107, 2(1984).

9. G. Goldhaber, Proc. Leptonic. Session 18th Recontre de Moriond, Vol.2,137(1983).

10. R. P. Feynman, Rev. Mod. Phys. 20, 37(1948).

11. "Selected Papers in Quantum Electrodynamics",ed. J. Schwinger, Dover(1958).

12. H. M. Georgi, H. R. Quinn, and S. Weinberg, Phys. Rev. Lett. 33, 451(1974).

13. H. Georgi and S. L. Glashow, Phys. Rev. Lett. 32, 438(1974).

14. F. Halzen and A. Martin,"Quarks and Leptons", J.Wiley and Sons(1984).

15. C. G. Callen and D. J. Gross. Phys. Rev. Lett. 21 No. 5, 311(1968).

16. P. Renton,"Electroweak Interactions: An Introduction to the Physics of Quarks and Leptons",Cambridge University Press (1990).

17. G.Altarelli,"Partons in Quantum Chromodynamics.", Phys. Rep. 81C, 1(1982).

18. J.Morfin and W.Tung."Parton distributions from a global QCD analysis of deep inelastic scattering and lepton-pair production", Fermilab-Pub-90/74,IIT-PHY-90/11(1990).

19. M. Gluck , E. Hoffmann, E. Reya,"Scaling violations and the gluon distribution of the nucleon",Z.Phys.C13,119(1982).

20. R. D. Field and R. P. Feynman, Nucl. Phys. B136, 1(1978).

21. J. Schwinger, Phys. Rev. 82, 664(1951).

22. H. Bohr and H. B. Nielson, NBI-HE-78-3(1978).

23. A. Casher, H. Neuberger and S. Nussinov, Phys. Rev. D20, 179(1979).

24. B. Andersson, G. Gustafson and C. Peterson, Nucl. Phys. B135, 273(1978).

25. B. Andersson, G. Gustafson and C. Peterson, Z. Phys. C1, 105(1979).

26. B. Andersson, G. Gustafson and C. Peterson, Z.Phys. C3, 223(1980).

27. T. Sjostrand, Comp. Phys. Comm. 27, 243(1982).

28. T. Sjostrand, Comp. Phys. Comm. 39, 347(1986).

29. U. Pettersson,"Ariadne- A Monte Carlo for QCD cascades in the color dipole formulation",Lund Preprint LU TP 88-5(1988).

30. L. Lonnblad,"Ariadne 3- A Monte Carlo for QCD cascades in the color dipole formulation",Lund Preprint LU TP 89-10(1989).

31. A. V. Kiselev and V. A. Petrov, Sov. J. Nucl. Phys. 38 No.5, 792(1983).

32. A. V. Kiselev and V. A. Petrov, JETP Lett. V.43 No. 1, 4(1986).

33. A. H. Mueller, Phys. Rev. D2, 1963(1970).

34. Z. Koba, H.B. Nielson, P. Olesen,Nucl. Phys. B40 317(1972).

35. The European Muon Collaboration, J. J. Aubert et al., "Multiplicities of charged hadrons in 280 GeV/c muon- proton scattering", Nucl. Phys. B258,249(1985).

36. The UA5 Collaboration, G. J. Alner et al., Phys. Lett. 160B,

193(1985).

37. The Aachen-Birmingham-Bonn-CERN-Imperial College- MPI-Oxford, Collaboration, M. Aderholz et al., Nucl. Phys. B223, 269(1983).

38. C. C. Chang et al.,Phys. Rev. D27,47(1983).

39. T. Coghen et al.,Z. Phys. C, 187(1986).

40. The European Muon Collaboration, J. J. Aubert et al., "Hadron Multiplicity variation with Q^2 and scale breaking of the hadron distributions in deep inelastic muon-proton scattering", Phys. Lett. 165 No. 1-3, 222(1985).

41. The E665 Collaboration, M. R. Adams et al., " A spectrometer for muon scattering at the Tevatron", NIM 291a, 533(1990).

42. V. Eckert, Technical Report TR002,E665 Internal Report, Dec.1985.

43. R. Fernow,"Introduction to Experimental Particle Physics", Cambridge University Press, p.293(1986).

44. S. Wolbers, Technical Report SW114,E665 Internal Report, Jan.1990.

45. J. Hanlon, Technical Report,July 23 E665 Collaboration meeting, July 1990.

46. H. Melanson, Technical Report SW073,E665 Internal Report, Dec.1988.

47. H. Melanson,T. Osbourne, Technical Report SW013 ,E665 Internal Report ,Jan.1986.

48. A. Bhatti,W. Wittek,S. Wolbers, Technical Report SW071, E665 Internal Report, Mar.1989.

49. J. Hanlon, Technical Report VS019, E665 Internal Report, Feb.1988.

50. R. Brun et al.,"GEANT 3 Users Guide",CERN DD/EE/84-1;(1986).

51. H. Melanson, Technical Report ST0255, E665 Internal Report, Mar.1990.

52. LEP talk Singapore Conf. May,1990